A Wideband Low-power Gyrator-enhanced Electrical Balance Duplexer For IR-UWB Transceiver

Heqi Deng

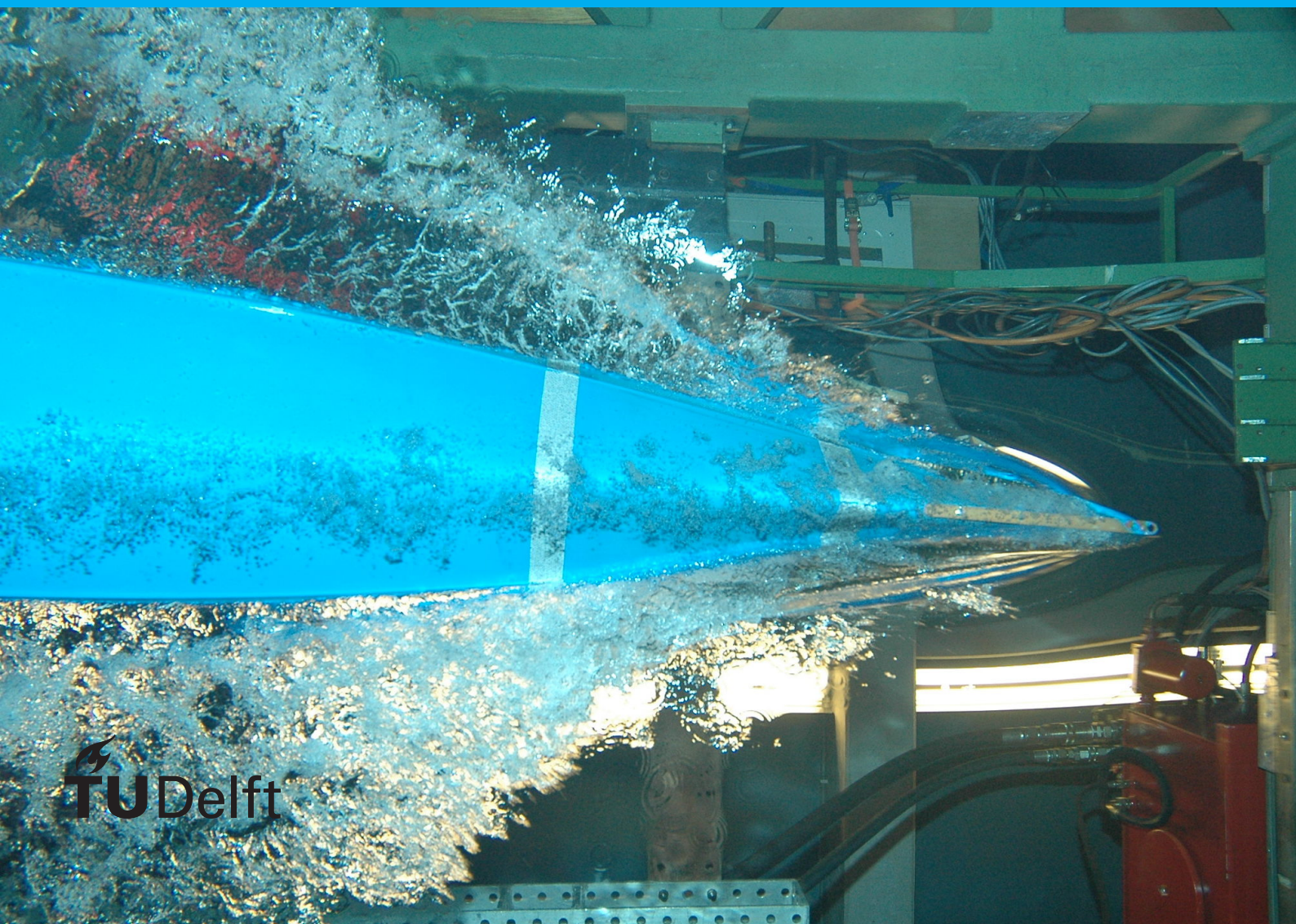

A Wideband Low-power Gyrator-enhanced Electrical Balance Duplexer For IR-UWB Transceiver

by

Heqi Deng

to obtain the degree of Master of Science
at the Delft University of Technology,
under the supervision of
Dr. Masoud Babaie (TU Delft)
and
Dr. Minyoung Song (imec & DGIST)
Dr. Anoop Bhat (imec)

Student number: 5489075
Project duration: September 1, 2022 – August 1, 2023
Thesis committee:
Dr. Masoud Babaie, TU Delft, supervisor
Dr. Minyoung Song, imec & DGIST, supervisor
Dr. Fabio Sebastiano, TU Delft

TU Delft imec

Acknowledgements

I was fortunate to research duplexers in UWB systems during my one-year internship at imec-nl. The study of EBD and full duplexing has been a hot topic in RFIC research in recent years. While at imec-nl, I completed my first full chip tape out with the help of my colleagues. I am grateful for their assistance.

Firstly, I would like to express my gratitude to my mentors, Minyoung Song and Anoop Bhat, for their exceptional guidance throughout my internship. Specifically, Minyoung provided me with this opportunity and offered extensive guidance ranging from project research direction to software configuration issues. Their professional knowledge, research attitude, and patient guidance have been invaluable to me. I am confident that Minyoung will become an outstanding professor in academia. Additionally, I would like to thank Jiang Liu for his invaluable help with the layout and Haoming Xin, Zule Xu, Meiyi Zhou, Huib Visser, and Yao-Hong Liu for their assistance.

In addition, I want to express my sincere gratitude to my supervisor at TuDelft, Masoud Babaie. His courses gave me a wealth of knowledge about RFIC circuit design. His ability to identify critical issues and offer enlightening insights during my master's project was instrumental. His valuable suggestions and constructive criticisms during my thesis writing greatly enhanced my work.

Furthermore, I am immensely thankful to my classmates at TuDelft. I am grateful for the companionship you provided during my Master's program. Your support was invaluable, and I learned a great deal from each and every one of you.

Finally, I want to express my deepest gratitude to my family. Your unwavering faith in me and constant support have been my pillars of strength. Whether it was through comforting conversations during challenging times or celebrating my victories, however small, your love and encouragement have been the driving force behind my endeavors. Thank you all for your endless support!

Heqi Deng
Eindhoven, August 2023

Preface

Wireless communication has become integral to our daily lives, enabling seamless connectivity and information exchange. As technology advances, there is a growing demand for wireless systems that can support higher data rates and simultaneously accommodate multiple users. Full-duplex communication, which allows for simultaneous transmission and reception on the same frequency band, has emerged as a promising solution to meet these evolving demands.

This master's thesis delves into designing and implementing a full-duplex impulse radio ultra-wideband (IR-UWB) transceiver to overcome the inherent challenges of simultaneous transmission and reception. The focus of this research lies in the development of a novel duplexer, a crucial component that enables the isolation of the transmit and receive paths, allowing for coexistence without self-interference.

This thesis sets the stage by introducing the motivation and significance of full-duplex communication systems. It provides an overview of the current state of IR-UWB technology and highlights the limitations and potential benefits of full-duplex technology. The introduction also outlines the research's objectives and scope, emphasizing the proposed duplexer's key role in achieving full-duplex operation. The thesis comprehensively reviews literature and research on full-duplex communication and IR-UWB technology, providing a foundation for understanding the technical challenges and opportunities of the proposed duplexer.

The subsequent chapters delve into the proposed duplexer and system-level design, including the architecture, components, and performance evaluation of the full-duplex IR-UWB transceiver. Special attention is given to the proposed duplexer, detailing its design principles, simulation results, and experimental validation. The performance metrics of the duplexer, such as isolation, insertion loss, and linearity, are thoroughly analyzed and discussed.

Furthermore, the thesis highlights the achievements and contributions of the research. The proposed duplexer demonstrates significant improvements in isolation and performance compared to existing solutions, paving the way for more efficient and reliable full-duplex communication systems. The findings of this research contribute to the growing body of knowledge in the field and provide valuable insights for future advancements.

In conclusion, this thesis presents a comprehensive study of the design and implementation of a full-duplex IR-UWB transceiver, focusing on the development and performance evaluation of a novel duplexer. The research outcomes contribute to advancing full-duplex RadCom, opening new possibilities for higher data rates, improved spectral efficiency, and improved target detection. The findings presented in this thesis lay the groundwork for future research and development in the field of full-duplex IR-UWB systems.

Contents

1

Introduction

Ultra-wideband (UWB) technology has recently been the subject of significant interest, given its high-speed data transmission and high-resolution capability. As defined by the Federal Communications Commission (FCC), a UWB device uses a signal with a fractional bandwidth (BW_{frac}) that exceeds 20%, or an absolute bandwidth (BW_{-10dB}) larger than 500 MHz (Fig. 1.1). The Defense Advanced Research Projects Agency (DARPA) further classifies a UWB signal as having a fractional bandwidth that exceeds 25% BW_{frac}. This fractional bandwidth is calculated as the ratio of the signal's -10 dB bandwidth to its center frequency in equation (1.1), with the center frequency defined as shown in equation (1.2).

$$BW_{frac} = \frac{BW_{-10dB}}{f_c} = \frac{2(f_H - f_L)}{f_H + f_L} \tag{1.1}$$

$$f_c = \frac{(f_H + f_L)}{2} \tag{1.2}$$

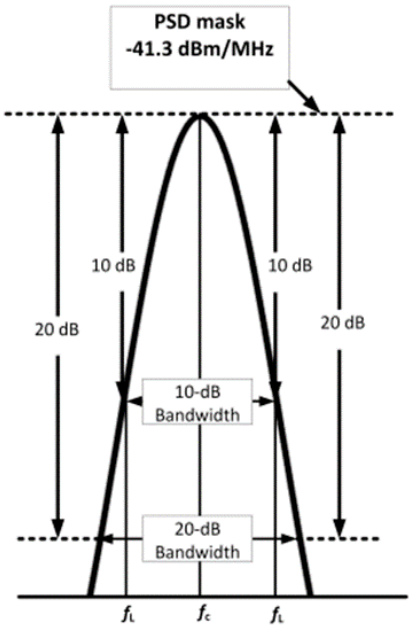

Figure 1.1: Definition of UWB signal [1].

UWB signals, as indicated in Fig. 1.1, set themselves apart from traditional narrow-band signals by offering a bandwidth exceeding 500 MHz, leading to a time-domain impulse with a pulse duration

of less than two nanoseconds. Even within the UWB context, a 500 MHz bandwidth is comparatively small, implying pulse durations that are typically sub-nanosecond. The frequency band available for UWB applications spans a broad range, from 3.1 GHz to 10.6 GHz.

Despite these advantages, the challenges of managing emission power and avoiding interference with nearby narrow-band signals due to the wide bandwidth and dispersed frequency bands cannot be ignored. In response, regulatory measures, such as power masks, have been established by the FCC and the Electronic Communications Committee (ECC) [2], as shown in Fig. 1.2.

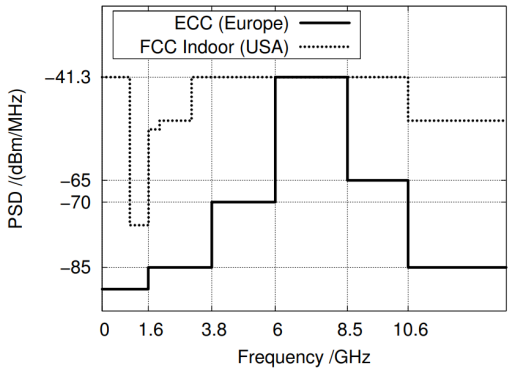

Figure 1.2: European UWB mask & FCC mask [2].

The two primary types of UWB communication systems are pulse-based and multicarrier-based. The latter, often implemented using orthogonal frequency-division multiplexing (OFDM), breaks down the entire UWB spectrum into numerous subbands, enabling it to circumvent transmissions in regions where other radio communication devices operate. However, these systems require complex signal processing techniques and sophisticated transceiver architectures [3].

Impulse Radio Ultra Wideband (IR-UWB) technology, a type of pulse-based UWB, uses exceedingly brief radio frequency pulses and provides considerable bandwidth, yielding several advantages. It grants substantial channel capacity, minimizes multipath effects, and facilitates high-precision timing [4]. Nonetheless, IR-UWB poses certain limitations, such as low transmission power to avoid interference and potential pulse distortion due to increased bandwidth [5].

This thesis centers on IR-UWB technology within the framework of a simultaneous radar and communication (RadCom) scheme. This RadCom or Joint Radar Communication (JRC) concept aspires to integrate radar and radio communication into a single device, enabling hardware components to be shared and thus promoting cost-effectiveness and system integration. The notable benefits of IR-UWB, such as its high channel capacity, resistance to multipath effects, and precision in timing, make it a prime choice for exploring and implementing the RadCom scheme. This chapter provides a summary of the technologies mentioned earlier. Subsection 1.1 explains UWB techniques, while Subsection 1.2 elaborates on the in-band full duplex (IBFD). Subsection 1.3 clarifies the research emphasis and scope of work of this thesis.

1.1. IR-UWB

Impulse Radio Ultra-Wideband (IR-UWB) is a recognized method of UWB signal transmission that uses ultra-short, low-duty-cycle baseband pulses. The design of these pulses, in terms of their shapes and durations, allows their frequency response to comply with the spectral mask defined by the Federal Communications Commission (FCC). Moreover, these pulses inherently operate within the radio frequency band, eliminating the need for a sinusoidal carrier to shift the signal [6].

IR-UWB technology, aiming at short-to-medium range transmissions focusing on power consumption reduction, has found applications in various sectors. These range from wireless sensor networks [7] and sensing/positioning systems to inter-chip communication, contactless wireless technology, and imaging systems, not to mention usage in biological or biomedical networks.

Optimized for energy-constrained, short-range wireless applications, IR-UWB radios are distinguished by their lower complexity and power consumption. These characteristics make them ideally

suited for personal area networks, low-power sensor networks, and wireless body area networks [8]. Furthermore, the high bandwidth capabilities of IR-UWB radios have fueled their use in high-precision location systems [9] and high data-rate dedicated communication links [10].

1.1.1. IR-UWB Applications

IR-UWB technology, integrated into the Internet of Things (IoT), has been recognized as a transformative force in healthcare applications. This technology is used to develop small, smart biomedical sensors that can be worn or implanted in the human body. These sensors form Wireless Body Area Networks (WBAN), which continuously monitor the physiological state of patients for both diagnosis and prevention purposes. The measurements taken by these sensors include vital signs such as Electrocardiogram (ECG), Electroencephalogram (EEG), temperature, and blood pressure. The IR-UWB technology is particularly noted for its secure transmission, low noise, and low energy consumption, making it an ideal choice for healthcare applications. The integration of IR-UWB technology in healthcare has led to the emergence of a new paradigm referred to as E-health. This involves the real-time monitoring of physiological signals for personalized healthcare. The real-time data provided by these sensors allows healthcare professionals to respond promptly to any changes in the patient's condition, thereby improving the quality of care. Furthermore, IR-UWB is recognized as a suitable technology for WBAN applications due to its ability to coexist with narrowband systems, low power consumption, and low-cost on-chip implementation. This makes it a cost-effective and efficient solution for healthcare monitoring systems [11].

1.1.2. IR-UWB General Specs

The communication rates of over 1 Gb/s were achieved by utilizing 3-D hybrid impulse modulation, which includes Pulse Shift Keying (PSK), Pulse Position Modulation (PPM), and Pulse Amplitude Modulation (PAM), even under conditions of 15 mm skin/fat [8]. According to [12], a data rate of 500 Mb/s was successfully reached with power consumptions of 27.7 mW for the receiver (RX) and 7 mW for the transmitter (TX), with a radio range of 1 to 5 m.

To ensure that the receiver can resolve the transmitted data, it should be designed to match the transmitter's maximum data rate of 1.66 Gbps in [8]. The transceiver works within the higher UWB band of 6.5 to 8 GHz, in compliance with the FCC power mask, and the total DC power of the transceiver should not exceed 50 mW. The targeted communication range is within the air's sub-meter level of 0.5 m. All the above specifications are summarized in Table 1.1.

Table 1.1: *Design specifications for communication applications*

Technology	**TSMC 28 nm**
Supply voltage (V)	**0.9**
Maximum Data Rate (Gbps)	**1.66**
DC Power Consumption (mW)	**25**
Frequency Range (GHz)	**6.5-8**
Communication Range (m)	**0.5**

1.1.3. IR-UWB Duplexing Methods

Ultra-Wideband (UWB) systems, similar to wireless communication, employ different duplexing types based on the interaction between the transmitter and receiver: Time Division Duplexing (TDD), Frequency Division Duplexing (FDD), Spatial Division Duplexing (SDD) and Full-Duplexing (FD), as shown in Fig. 1.3.

UWB devices use pulse transmission and reception to exchange data and determine location. TDD is the most commonly used duplexing method in this context, as stated in [9][13]. TDD involves a single-pole double-throw (SPDT) switch between TX and RX, which means the receiver is disabled during transmission and the transmitter disabled during reception, as shown in Fig. 1.3. This method effectively prevents receiver desensitization, which is typically caused by leakage of the transmitted signal. However, it also introduces a few notable drawbacks. These include reduced transmission

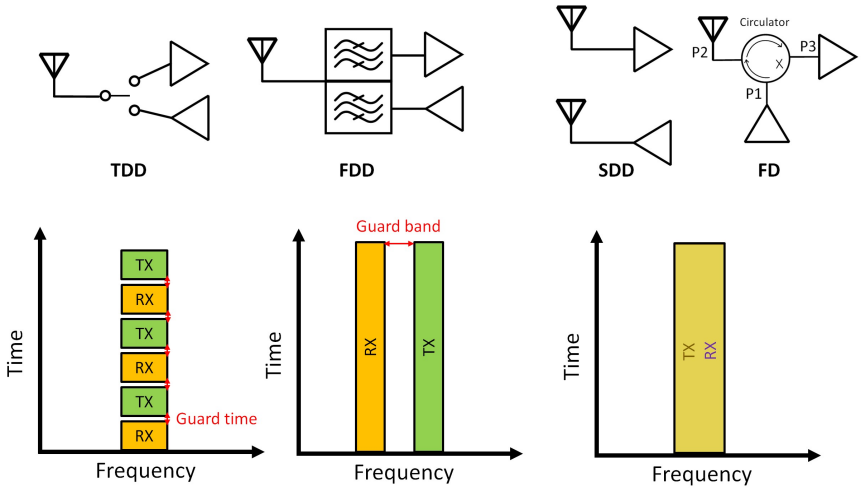

Figure 1.3: Duplxing methods in UWB system.

speed in wireless communication applications. TDD might reduce communication speeds due to the necessity of switching between transmitting and receiving modes. In TDD, the same frequency channel cannot transmit and receive at the exact same time. Instead, the system alternates between transmitting and receiving data. This switch introduces what's known as a 'guard time' – a brief pause to ensure that the transmission is fully completed before the system switches to receiving mode, and vice versa. This is to prevent overlap between the two modes, which could cause interference. The time taken to switch modes and the addition of the guard time reduces the effective data rate because the channel is not being utilized for a small portion of time. Additionally, the system needs to process the switching, which can also contribute to slower transmission speeds.

Moreover, it results in a "blind zone" in range measurement in radar applications. This blind zone is created because the receiver must periodically shut down, rendering it incapable of receiving echo signals at specific intervals. This periodic shutdown is necessary to avoid interference from the transmitted signal, but it inevitably leads to periods where signal reception is impossible, thereby creating gaps or "blind spots" in the overall range measurement capability.

FDD has been proposed as a potential solution to these issues, but its application may lead to a decrease in spectrum utilization. To prevent interference between these bands, there are unused frequency ranges, known as guard bands, between the transmit and receive bands. These guard bands, while necessary for preventing interference, are a portion of the spectrum that is not being used for data transmission, thereby reducing the overall spectrum efficiency. An alternative method is the utilization of two separate antennas—one for reception and the other for transmission—which could, however, lead to an increased system footprint [14][15].

For effective operation within a UWB system, SDD requires at least two antennas, as the antenna is the component that consumes the most space. Consequently, the application of SDD is often limited.

Compared to TDD, FDD, and SDD, full-duplex technology presents an appealing solution, as shown in Fig.1.3. It offers improved spectrum efficiency, mitigates the problem of blind zones in range measurement, and allows for the simultaneous use of a single antenna for both transmission and reception, effectively reducing the circuit footprint. In a typical full-duplexing system, there is a three-port circulator that allows signals to travel only between Port 1 (TX) and Port 2 (ANT), as well as between Port 2 (ANT) and Port 3 (RX). It's important to note that Tx and Rx are isolated from each other.

1.2. In-Band Full Duplex

The In-Band Full Duplex (IBFD) technology allows devices to transmit and receive signals at the same frequency, also known as Simultaneous Transmission and Reception (STAR) or Simultaneous Frequency Full Duplex (SFFD) [16]. However, Full Duplex (FD) should be used carefully as it may refer to systems like Frequency Division Duplex (FDD) that transmit and receive on different frequencies. In this thesis, FD specifically refers to IBFD [16, 17]. FD could represent a significant step forward for UWB and RadCom systems. By allowing for simultaneous data transmission and reception within the

same frequency band, FD maximizes the use of available bandwidth and harmonizes with the inherent advantages of UWB and RadCom systems.

Numerous systems, including cellular phones, Wi-Fi communications, and certain radar architectures, traditionally avoided FD implementation due to the severe self-interference (SI) produced when a transmitter and receiver are co-located [18]. SI can cause receiver desensitization within the desired receive band, overpowering conventional filters tasked with interference suppression [19][20]. Initial FD research primarily concentrated on Continuous Wave (CW) radar systems, using continuous transmission to enhance signal reception [21]. Subsequently, it was discovered that a wide array of other wireless systems could also derive considerable benefits from FD [22].

1.2.1. Self Interference

The idea of FD communication is not entirely new. For instance, early electronic phones used hybrid transformers to separate the earpiece from the microphone, thereby enabling FD communication over a two-wire loop to the central office [20]. Within the radar domain, practical ferrite material-based circulators have facilitated FD operation of transmitters and receivers.

However, introducing FD operation in commercial wireless applications like cellular communication and WiFi poses unique challenges. The primary hurdle with FD wireless is the substantial transmitter (TX) SI occurring at the receiver (RX), which can be 90-120 dB stronger than the intended signal depending mainly on the application. Such potent SI is particularly susceptible to wireless channel uncertainties, including frequency selectivity, time variation, and transceiver electronics imperfections, such as nonlinear distortion and phase noise.

These challenges escalate when considering integrated implementations intended for cost-sensitive and size-limited mobile devices. Preliminary studies verified the feasibility of SI cancellation and FD operation in commercial wireless applications utilizing laboratory equipment and off-the-shelf components. SI cancellation surpassing 100 dB has been demonstrated for military applications. However, these attempts' self-interference cancellation (SIC) techniques fundamentally conflict with small-size/integrated circuit (IC) implementation requirements.

Thanks to advancements in complementary metal oxide semiconductor (CMOS) technology, complex digital SIC can provide around 50 dB SIC and can be readily implemented. However, many current analog/RF SICs in FD demonstrations depend on eliminators using bulky off-the-shelf components, which are not compatible with compact and low-cost IC implementations. Integrating analog/RF SICs in ICs is vital for embedding FD wireless technology into mobile devices like smartphones and wearable devices [19].

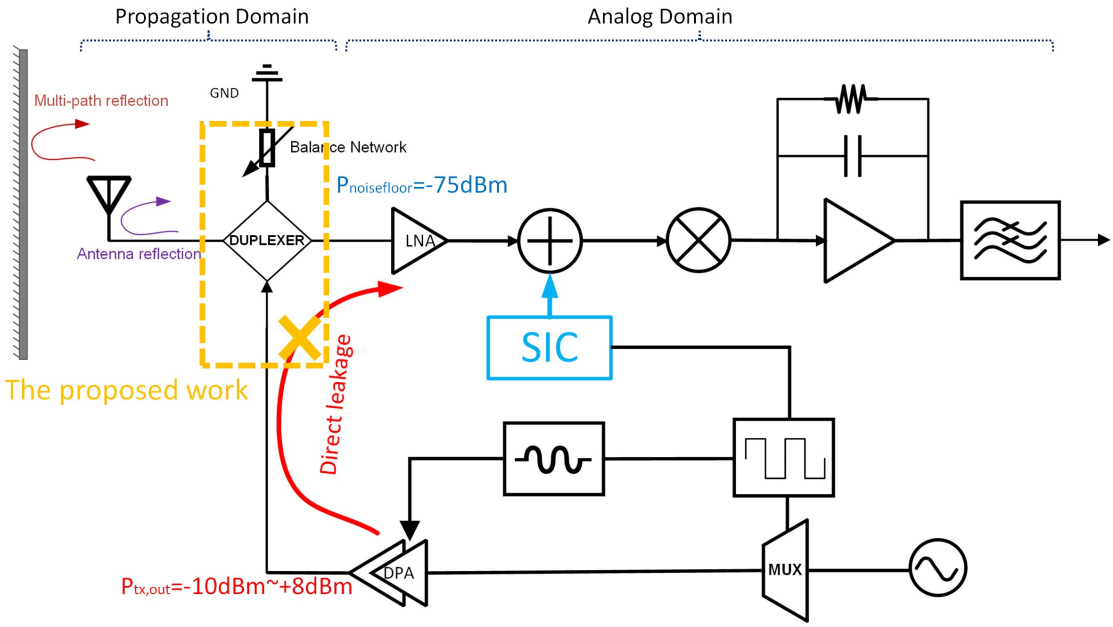

Figure 1.4: Self-interference and cancellation.

1.2.2. Self-Interference Cancellation

The authors of [23, 16] conducted studies on the impact of self-interference (SI) on various system components. They extensively classified self-interference cancellation (SIC) methods in multiple domains, such as the propagation, analog, and digital domains, as shown in Fig. 1.4.

Several transmit-to-receive coupling paths exist within the propagation domain. One such path is the direct path through the antenna interface device, which typically exhibits limited isolation when a shared antenna is used. The domain also illustrates the first received over-the-air path for multi-antenna setups. Systems utilizing a shared antenna enjoy a smaller antenna footprint but also need to counteract the antenna reflection path arising from imperfect matching of the antenna impedance to the interfacing device. Both direct leakage and antenna reflection signals usually pose the most significant interference, necessitating proper management of the multi-path reflection paths created by environmental objects. Contrary to the relatively static direct path coupling, antenna path and multi-path reflection signals are dynamic—affected by surroundings, thus necessitating suitable handling.

The analog domain includes RF and analog circuit hardware that connect antennas or antenna interfaces to the digital conversion stages. Fig. 1.4 shows the IR-UWB transceiver and highlights key components to indicate various cancellation locations. The first self-interference cancellation occurs between the antenna and the Low Noise Amplifier (LNA), preventing the LNA from being saturated by a strong self-interference signal. This takes place in the propagation domain, utilizing a duplexer, which is the main focus of this master's thesis. The second Self-Interference Cancellation (SIC) occurs between the LNA and the mixer in the analog domain. After these two stages of SIC, the signal enters the mixer, Transimpedance Amplifier (TIA), and Low Pass Filter (LPF) circuits. Although Digital Signal Processing (DSP) provides infinite flexibility for the digital domain SIC and has always been a hot research topic, this technology is not covered in this thesis.

1.2.3. Challenges of FD

Full-duplex systems enhance radar and communication by transmitting and receiving signals simultaneously. However, the adoption of FD systems introduces the challenge of self-interference, which can be mitigated through sophisticated signal processing techniques and meticulous hardware design. These challenges include:

- **Self-Interference (SI):** This is the most significant challenge in FD. When a device is transmitting and receiving simultaneously, the transmission can interfere with the reception, deleting the received signal's quality.
- **Hardware Complexity:** Implementing FD requires additional hardware components for self-interference cancellation, which can add to the complexity and cost of the devices. Moreover, it may result in increased power consumption.
- **Implementation in Mobile Devices:** Implementing FD in compact and cost-sensitive mobile devices presents additional challenges, as it requires integrated circuit designs and self-interference cancellation techniques that are compatible with these devices' size and power constraints.
- **Dynamic Environment:** The performance of FD system can be affected by the dynamism of the wireless channel, including frequency selectivity and time variation. Also, the signal's reflection on surrounding objects can create multipath interference, adding to the challenge of self-interference cancellation.
- **Non-Linear Distortions and Phase Noise:** These can be introduced by the imperfections of the transceiver, which can further complicate the task of self-interference cancellation.
- **Design of SIC Algorithms:** Designing self-interference cancellation algorithms that can provide sufficient cancellation, particularly in the digital domain, is a challenging task.

1.3. Scope of Work

1.3.1. Challenges of Duplexer

Therefore, in response to the aforementioned challenges, the following parameters are particularly important.

- **Isolation:** In order to suppress the co-channel leakage from TX to RX, the isolation between TX and RX needs to be as high as possible. Firstly, because the signal power from TX leakage to RX is too high, it may desensitize the receiver, thus degrading the overall performance of the receiving link. This can result in reduced receiver gain and issues of nonlinearity. Secondly, if the suppression of the leakage signal is insufficient, causing the power of the leakage signal to exceed the noise floor, this would decrease the signal-to-noise ratio of the transceiver.
- **Area:** Adding a duplexer between the receiver and transmitter will increase the complexity of the chip. Therefore, the designed duplexer circuit should be as simple as possible, and its area should also be as small as possible.
- **Power Consumption:** Not only the chip area, since the power consumption of the entire UWB chip is less than 50 mW, the power consumption of the duplexer should not be high, ideally not exceeding 5 mW.
- **Tunability:** The antenna impedance varies with the changes in the external environment. Therefore, the duplexer must maintain good performance despite changes in antenna impedance.
- **Insertion loss & Noise Figure:** The received signal will enter the duplexer before entering the LNA, so its noise figure (NF) will greatly affect the receiver's noise figure. Therefore, its NF should be as low as possible. Similarly, the transmitted signal must pass through the full duplex, which requires a low insertion loss.

1.3.2. Specifications

The self-interference in this thesis is shown in Fig. 1.4. After the transmitted signal passes through the duplexer, the self-interference signal is suppressed and then enters the LNA. The LNA will amplify the Self-Interference (SI), which is then further suppressed by the Self-Interference Cancellation (SIC) in the analog domain. The key specification is the level of isolation between TX and RX. The amount of suppression needed for SI is determined by factors such as transmitted power, the noise floor of the receiver, and the required SNR. To calculate the RX noise floor, take into account the channel bandwidth (BW) and the receiver's NF. The calculated noise floor is -75 dBm. The TX-RX isolation in the antenna interface needs to meet at least three requirements: 1. It should not desensitize the receiver. 2. It should not lower the SNR of the UWB chip to SNR_{min}. 3. It cannot exceed the maximum value of 0 dBm for the ADC input. The link budget of the entire receiving link is shown in Fig. 1.5. The maximum gain of the entire receiving link is 53 dB. The output power of the transmission link is between -10 dBm and 8 dBm. It's important to note that after ADC sampling, by utilizing the determinacy of the signal and multiple received pulse signals, a coding gain of 64 dB can be achieved. Coupled with the 6 dB gain obtained from ADC oversampling, a gain of 70 dB can be achieved in the digital domain. The SNR result is 36 dB, the needed SNR is 23 dB, leaving a margin of 13 dB. Overall, the required isolation in antenna interference and the needed self-interference cancellation in the analog domain are 28 dB, and 33 dB, respectively.

$$P_{NoiseFloor}(\text{dBm}) = -174(\text{dBm/Hz}) + 10\log(BW[\text{ Hz}]) + NF(\text{ dB}) \tag{1.3}$$

This thesis aims to develop a novel duplexer that achieves in-band full duplexing from 6.5 to 8 GHz. To prevent receiver desensitization, it is important to have isolation greater than 30 dB, insertion loss below 3 dB, noise figure below 4 dB, and power consumption below 4.5 mW. All of these specifications are compiled in Table 1.2 for reference.

In order to make it more practical, a complete UWB transceiver has been developed, which includes a duplexer for FD and Radcom capabilities. The transceiver also has a digital self-interference cancellation (DSIC) that provides active self-interference cancellation and increased isolation. The DSIC is a fully digital self-cancellation technique that was first introduced in Sander Hijmans' master's thesis and further refined in Jiang Liu's master's thesis. Both the transmitter and receiver use a validated circuit [8].

The structure of this thesis is as follows: In Chapter 2, various FD techniques are discussed, including their advantages and disadvantages. Chapter 3 introduces a new wideband, low-loss duplexer and explains its design principles. The design of the complete UWB transceiver is presented in Chapter 4. Lastly, Chapter 5 contains the concluding remarks and the future work.

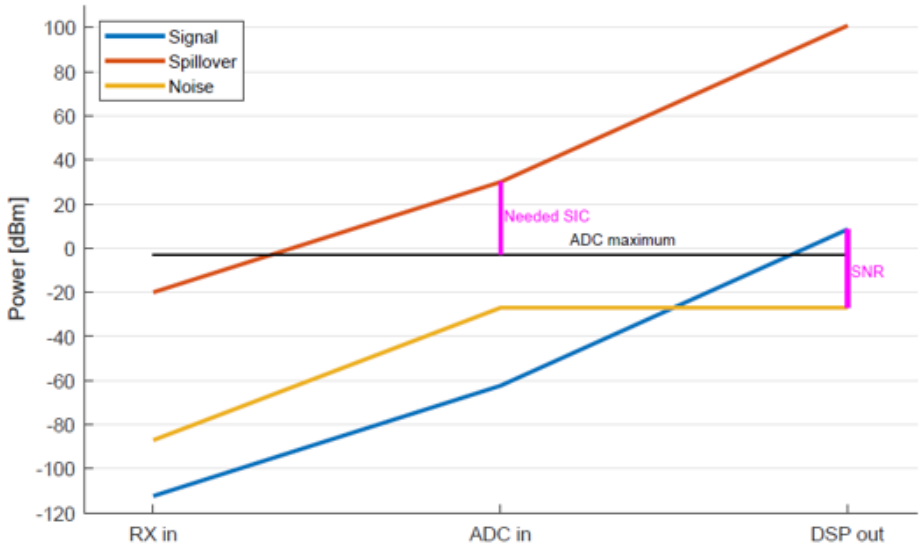

Figure 1.5: Link Budget.

Table 1.2: *Design specifications for duplexer*

Technology	**TSMC 28 nm**
Supply Voltage (V)	**0.9**
Isolation (dB)	**30**
DC Power Consumption (mW)	**4.5**
Operating frequency	**6.5-8**
Bandwidth (GHz)	**1**
Noise Figure (dB)	**4**
Insertion Loss (dB)	**3**

2

Existing Full Duplexing Technology

In the past, non-reciprocal circulators were created using ferrite materials [24]. Thanks to the Faraday effect, these materials display non-reciprocity when applying an external magnetic field. However, ferrite circulators are costly and cumbersome because the materials used are incompatible with integrated circuit fabrication processes. Therefore, a significant interest is in creating high-performance, non-magnetic integrated circulators.

This master's thesis focuses on duplexers in the propagation domain, with a particular emphasis on electrical balanced duplexers (EBD) and non-magnetic circulators. For duplexers in the propagation domain, they must meet specific criteria. They should be compact and devoid of losses, offering an incredibly high power handling capability without necessitating additional power consumption. Conventional FD demonstrations depend on large off-the-shelf antenna interfaces, like antenna pairs and ferrite circulators [24]. Regrettably, these are not suitable for mobile applications due to their form factor limitations and the requirement for condensed and integrated FD antenna interfaces. Compact duplexers have improved compatibility with MIMO and diversity applications. Additionally, single-antenna FD ensures wireless channel reciprocity, which can offer significant benefits [25]. Compact single-antenna duplexing has been demonstrated in full-duplex single-antenna radio systems (STAR) [19, 20, 26, 27, 28].

The electrical balanced diplexer (EBD) has also been suggested as a reciprocal shared antenna interface for FD. As a hybrid transformer, it can provide isolation between transmit (TX) and receive (RX) paths by balancing impedance, but it can result in a minimum 3 dB loss in both the TX-antenna and antenna-RX [29, 30]. This chapter will introduce three main full duplexing technologies in the propagation domain, along with their circuit principles.

2.1. Active Quasi-Circulator

In contrast to the recent popular trend of utilizing linear periodically time-varying (LPTV) circuits for non-reciprocal phase shifting, non-reciprocal circuits realized through active-biased transistors [31, 32, 33, 34] or gyrator circuits [35] are comparatively simpler, as they do not require complex and precise clock signals.

Transistors that are biased with a DC current or voltage inherently exhibit non-reciprocity due to their unilateral gain, as shown in Fig. 2.1 and Fig. 2.2. For example, an active-biased transistor with a forward gain $|S21| > 1$ can be an isolator with non-reciprocal signal transmission $|S21| > |S12|$. Initially, active transistors were employed to realize magnetless non-reciprocal components.

The core of a typical active quasi-circulator is illustrated in Fig. 2.1. It comprises a common-gate transistor (M1) and a common-source transistor (M2). The system works by transmitting signals from Port 1 (TX) through two separate paths before reaching Port 3 (RX). The first path, which is in-phase, goes through transistor M1, and the second, which is out-of-phase, passes through transistor M2. As the signals converge at port 3 (RX), there is a chance that they may cancel each other out, resulting in isolation. However, the amplitude and phase variations caused by the signal passing through the in-phase and out-of-phase paths depend on the frequency characteristics of the two different transistor circuits. Therefore, the circuit in Fig. 2.1 can only achieve limited isolation within a certain bandwidth.

Additionally, since M1, M2, and the current source all inject noise into Port 3, the circuit's noise performance is also poor.

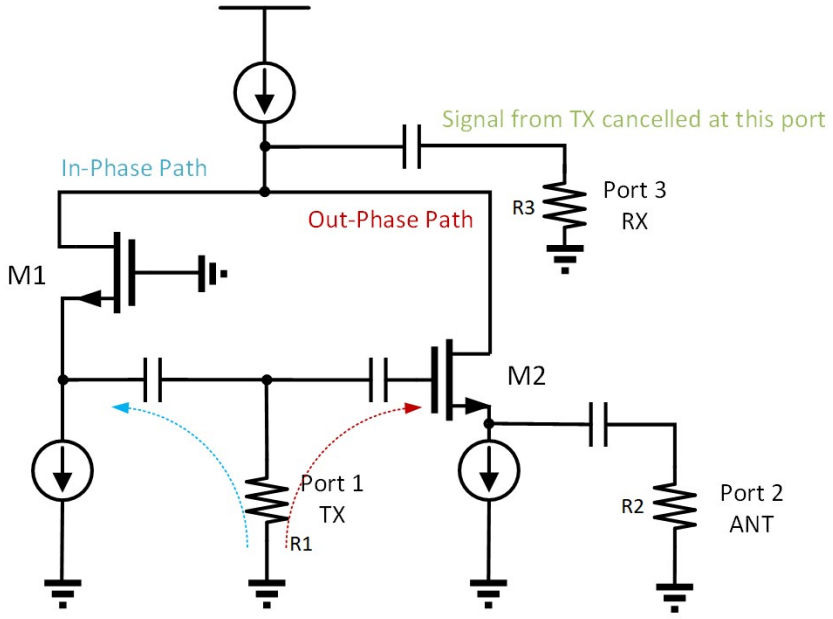

Figure 2.1: Typical active quasi-circulator based on active-biased transistors.

The diagram shown in Fig. 2.2 provides an example of an active quasi-circulator design using CMOS isolators [34]. This design includes two main components: two CMOS isolators and a Wilkinson power divider. The CMOS isolators control the signal's direction, while the Wilkinson power divider maintains primary isolation between ports 2 and 3. Compared to the active quasi-circulator, as shown in Fig. 2.1, this design can achieve higher P1dB, enabling the quasi-circulator to handle higher power levels. However, it's important to note that mismatches between the Wilkinson divider and the isolators can negatively impact the return losses of port 2 and port 3 and the insertion losses.

Active quasi-circulators tend to be sensitive to the DC bias. Moreover, the transistor's noise and nonlinearity can deteriorate the circulator's performance, especially under high power conditions. Their power-handling capabilities are insufficient. Therefore, they are not often used in traditional wireless communication and radar applications where the front end of the transceiver requires exceptional power handling for transmission and low noise for reception. However, these active methods are compatible with integrated circuit fabrication and have found applications in low-power communications [36] and biomedical systems [37]. Nevertheless, they are ultimately limited by the noise and nonlinearity introduced by the active devices.

2.2. EBD Technologies

In order to integrate a duplexer into a system, a couple of strategies can be adopted. Either nonreciprocity must be attained through alternative means, or the duplexer's reciprocity needs to be preserved using a four-port network, as depicted in Fig. 2.3. Consequently, electrical balanced duplexers with four ports are introduced. The antenna, RX, and TX ports are necessary, while the balance network (BAL) port "balances" the signal from TX to RX.

Electrical balanced duplexers (EBDs) can offset self-interference in FD systems, where transmission (TX) and reception (RX) occur simultaneously on the same frequency and time frame [38]. Alongside this passive cancellation at the EBD level, active cancellation methods can be used within the RF front ends. This dual-mode cancellation can be implemented simultaneously for both frequency-division duplexing (FDD) and FD systems, offering an enhanced capability for TX–RX leakage cancellation. This approach improves the overall effectiveness of the systems by minimizing self-interference and maintaining the integrity of the received signal [39].

As shown in Fig. 2.3, when the transmitting signal travel from the power amplifier (PA) to ANT

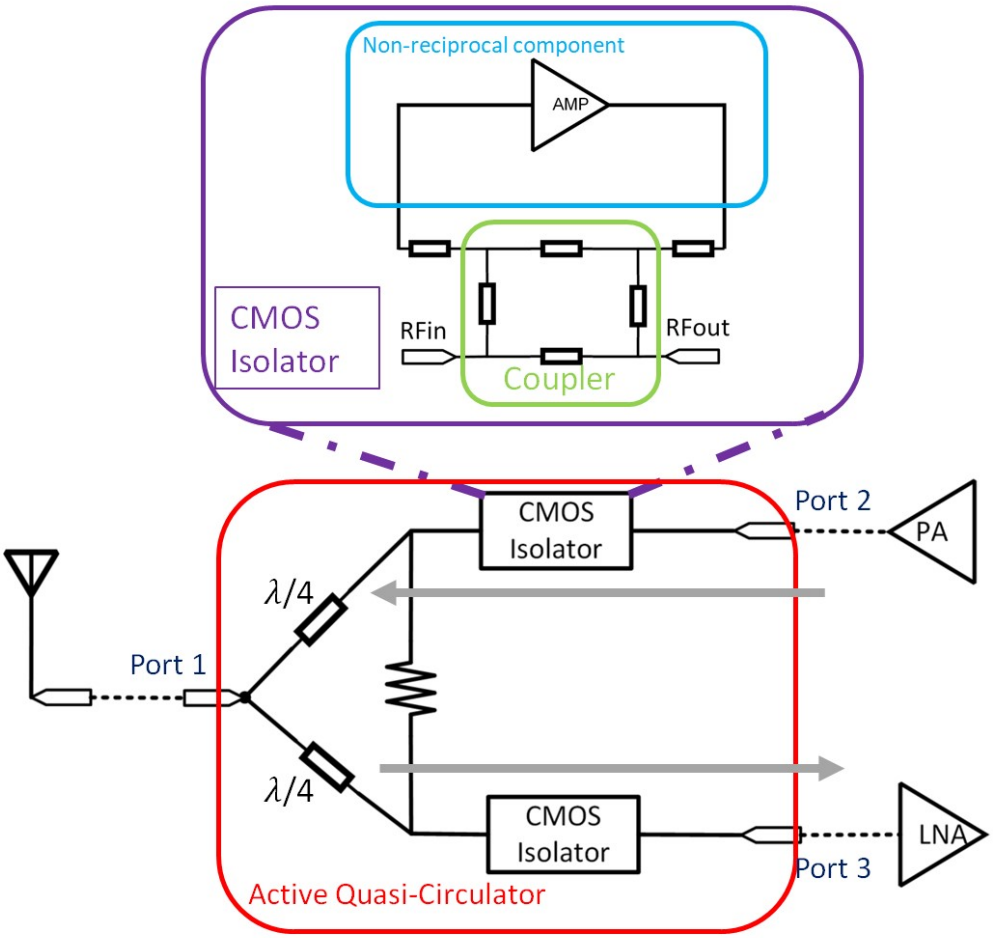

Figure 2.2: The diagram of the active quasi-circulator by using CMOS isolators.

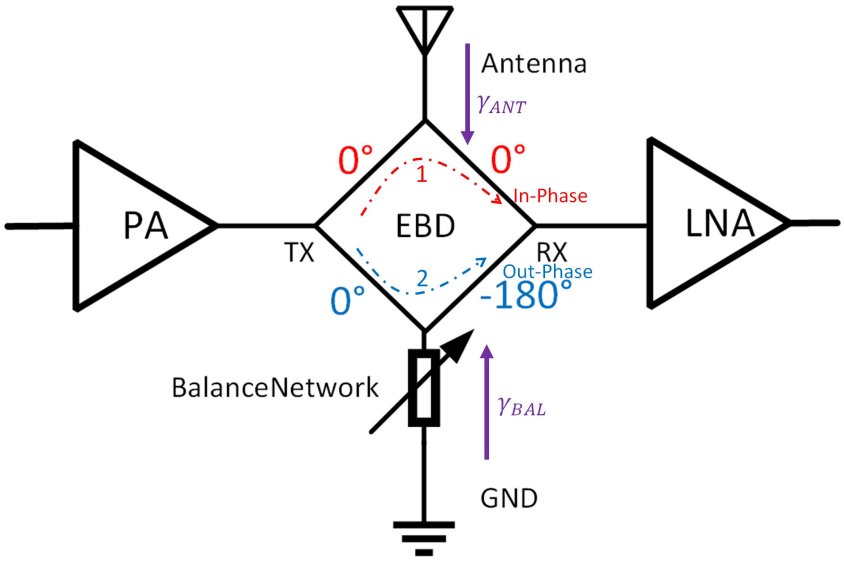

Figure 2.3: EBD Circuit.

(Path 1), the transmitted signal leaks to the RX port. Simultaneously, the transmitting signal reaches the RX port through TX-BAL-RX (Path 2). Unlike the signal reaching the RX through path 1, the signal reaching the RX through path 2 is out-phase, with a phase difference of $180°$. This results in electrical balance, where the power flowing through Path 1 is canceled out by an equal amount of power in Path 2, completely isolating the TX and RX ports. To achieve this, the reflection coefficient at the BAL port (γ_{BAL}) must be correlated to the reflection coefficient at the ANT port (γ_{ANT}). This means that the impedance at the BAL port (Z_{BAL}) must respond to changes in the antenna impedance (Z_{ANT}). To match RX, TX, BAL, and ANT ports simultaneously, **bi-conjugancy** must be achieved.

2.2.1. Bi-conjugacy Concept

In contrast to the definition of conjugacy in circuit design, bi-conjugacy does not refer to the complex conjugate of a complex number. Instead, in EBD circuits, two ports, such as TX and RX, are considered bi-conjugate if they are electrically isolated from each other within the circuit and exhibit equal but opposite signal transfers to the other ports. This behavior is accomplished by utilizing balanced voltages or currents to position the two ports forming a bi-conjugate pair in an electrical null zone, effectively canceling out any signals generated by the other two ports [40]. Obtaining bi-conjugacy can be achieved using a hybrid transformer, as described in [41].

2.2.2. Hybrid Transfomrer

In [41, 42], the hybrid transformer circuit used in EBD circuits is analyzed in detail. Its simplified model is shown in Fig. 2.4. R_A, R_B, R_C, and R_D are the impedances of the ports, while N1 and N2 represent the number of turns for the primary and secondary coils, respectively. The power transmitted by the TX is split between the antenna and the balance port in a ratio r, which corresponds to the tapping ratio of the primary windings. To achieve circuit matching, bi-conjugacy must be satisfied between TX and RX and between ANT and BAL as expressed in equation (2.1).

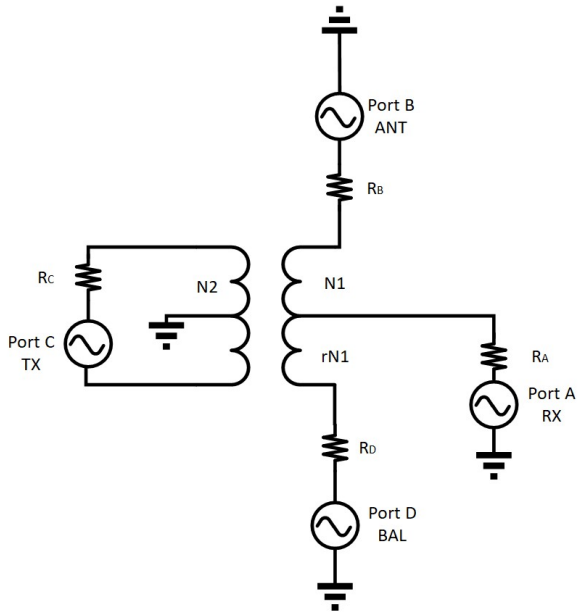

Figure 2.4: Hybrid transformer.

$$
\begin{aligned}
R_D &= rR_B \\
R_A &= \frac{r}{1+r}R_B \\
R_C &= \frac{1}{1+r}\left(\frac{N_2}{N_1}\right)^2 R_B
\end{aligned}
\tag{2.1}
$$

2.2.3. Insertion Loss and Isolation

As mentioned earlier, as shown in Fig. 2.3 and Fig. 2.4, the power at the TX port divides into two paths, and the 'r' power ratio represents the proportion of power transferred from TX to ANT port (P_{TX-ANT}) compared to the power transferred from TX to BAL port (P_{TX-BAL}). The 'r' can be easily modified by adjusting the turn ratio in hybrid transformers.

$$\begin{aligned} \mathrm{TXIL}(r) &= 10\log\left(\frac{1+r}{r}\right), \\ \mathrm{RXIL}(r) &= \mathrm{NF}(r) = 10\log(1+r). \end{aligned} \tag{2.2}$$

It can be demonstrated that the insertion losses on the TX path (TXIL) and the RX path (RXIL), or the noise figure (NF), follow a specific relation. Fig. 2.5 demonstrates the relation between the insertion loss and the ratio 'r'. As 'r' changes, a tradeoff between TXIL and NF exists, as shown in Fig. 2.5. When 'r' equals 1, TXIL and RXIL (or NF) hold 3 dB values, highlighting a balanced state [30]. This 3 dB loss is the intrinsic loss of the EBD circuit.

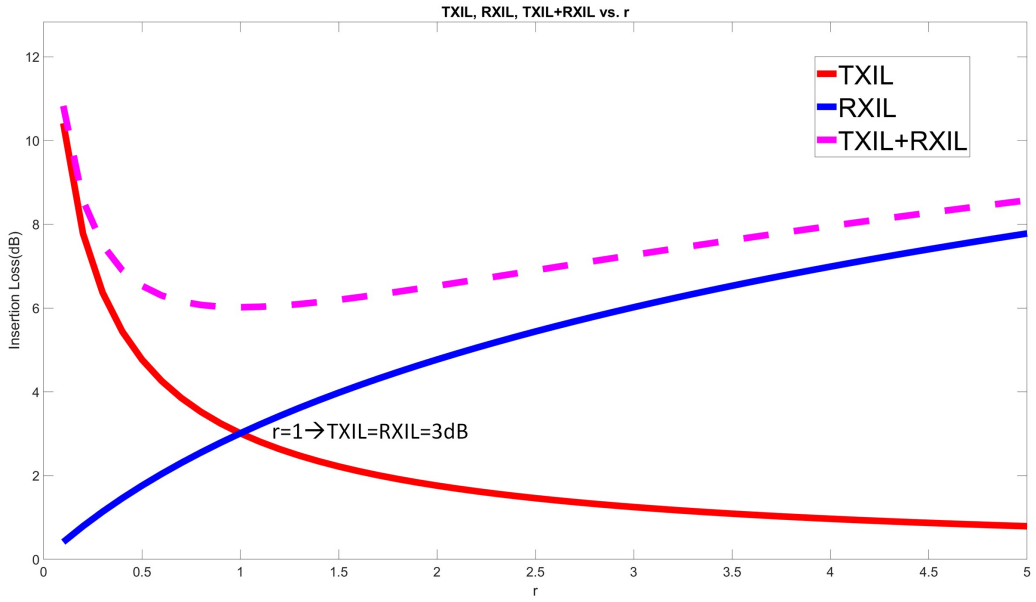

Figure 2.5: TXIL and NF of a lossless EBD as a function of r.

In practical use, the extent of TX-RX isolation bandwidth depends on the matched reflection coefficients (or impedance) between the BAL and ANT ports [42]. The transceiver's isolation is determined by the reflection coefficients of the antenna and the balance network, as shown in equation (2.3). In an ideal case, infinite isolation is achieved over an infinite operating frequency range if the antenna and BAL impedances are equal to $50\,\Omega$. However, the antenna impedance depends on the frequency and the surrounding environments. One method to increase bandwidth is to design the BAL so that its impedance closely follows the impedance of the antenna as the frequency changes. This requires careful engineering and may involve incorporating adjustable elements. However, this approach inevitably increases the complexity of the circuit.

$$\mathrm{TX-RX_{ISO.}}(r,\omega) = 20\log\left|\gamma_{\mathrm{ANT}}(\omega) - \gamma_{BAL}(\omega)\right| - 20\log\left(\frac{1+r}{\sqrt{r}}\right) \tag{2.3}$$

2.2.4. EBD implementations

In [43], a notably complex balance network was designed, as illustrated in Fig. 2.6. This design is compatible with all LTE bands within the frequency range of 0.7 to 1 GHz. The design of the advanced balance network aims to ensure stable and efficient performance across multiple LTE bands, accounting for variable conditions. There are ten fixed inductors and nineteen adjustable capacitors. While this

BAL achieves a relatively large adjustable range and precision, it requires a significant chip area to accommodate.

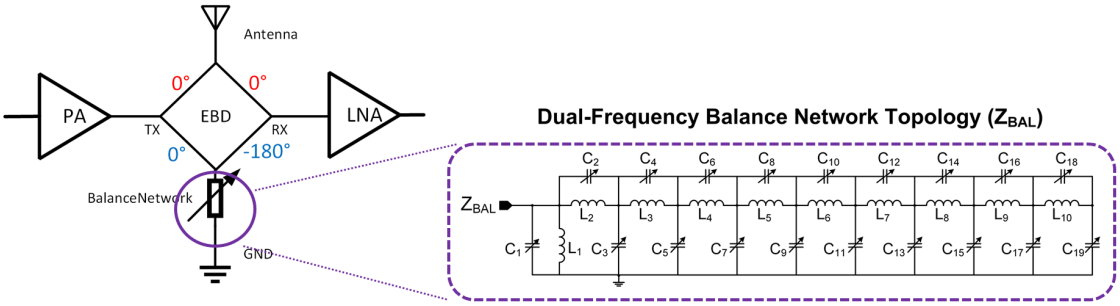

Figure 2.6: The balance network circuit.

[44] proposed a new EBD circuit called the Phase Gradient Supported Electrical Balance Duplexer (PBD). The PBD collects signal energy that would otherwise be lost to the ground and improves EBD's 3 dB intrinsic loss. As shown in Fig. 2.7, by controlling the phase of the phase shifter, the signal can be directed from the antenna to the RX or from the TX to the antenna. The balance network can also compensate for impedance mismatches at the antenna port. However, since the components comprising the PBD are reciprocal, the PBD itself is also reciprocal. In ideal conditions, energy can flow entirely from the TX to the ANT or from the ANT to the RX, but these two scenarios cannot be simultaneously achieved. Therefore, the PBD is an improvement on the EBD for FDD applications, as it has no fundamental insertion loss limit but uses a similar mechanism for isolation.

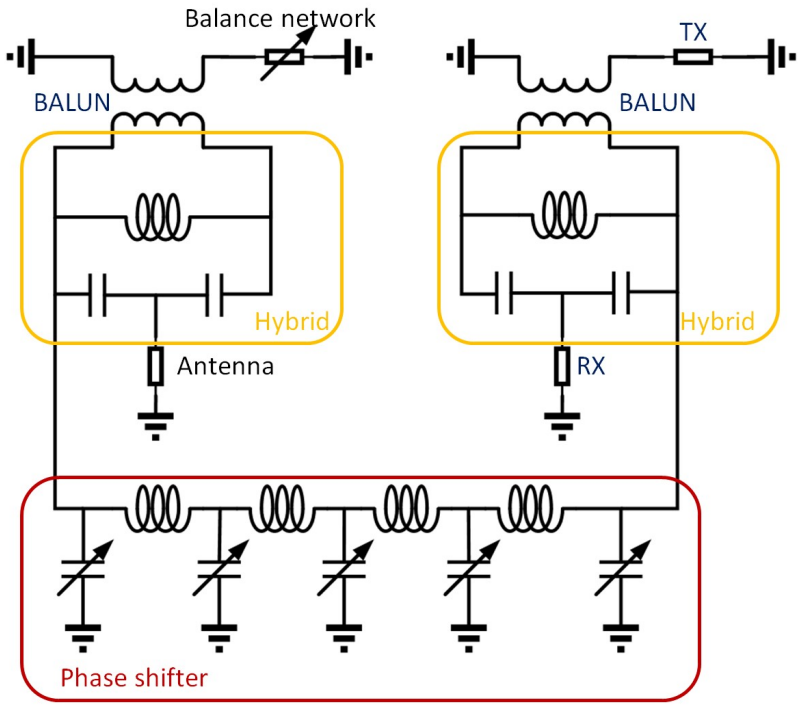

Figure 2.7: The schematic of PBD.

In conclusion, EBDs come with certain advantages. They demonstrate high linearity without requiring direct current (DC) power consumption. Moreover, they offer adaptive isolation courtesy of reconfigurable balance networks. This feature allows the EBD to be more flexible and adaptable to varying operational conditions, enhancing its overall performance and efficiency [19]. However, in practical applications, these transmission losses can escalate by an additional 0.5 to 2 dB due to non-ideal factors

such as metal resistivity and substrate loss. Taking into account the inherent 3 dB loss of the EBD, the combined losses at the receiver and transmitter can reach up to 8 dB, which limits the application of EBD.

2.3. Non-magnetic Circulator

In order to overcome the 3 dB loss limitation, it is necessary to break the principle of reciprocity. Traditional non-reciprocal shared-antenna full-duplexers use non-reciprocal ferrite-based circulators which rely on magnetic materials. However, these materials are incompatible with CMOS technology, making the duplexer bulky and expensive.

There is a great need for shared-antenna FD systems that do not require reciprocity and are compatible with CMOS technology. These systems should have low loss and be able to support high transmission power. Integrating the antenna interface on the same platform as the transceiver offers a unified design and optimized radio system. This approach presents an opportunity to review and question some long-standing design principles for RF systems [19].

Lorentz reciprocity is a fundamental characteristic of electronic structures that are linear, time-invariant, passive, and based on traditional materials with symmetric permittivity and permeability tensors. Traditionally, nonreciprocity has been achieved using the magneto-optic Faraday effect in ferrite materials. However, as previously mentioned, ferrite materials are incompatible with CMOS processes. Also, active circulators are limited in their linearity and noise performance, making them unsuitable for radio applications with stringent linearity and noise requirements.

Recently, a novel approach to non-magnetic nonreciprocity was introduced based on passive transistor switching for spatiotemporal conductance modulation, compatible with CMOS. There is ongoing research into high-performance passive non-magnetic circulators based on linear, periodically time-varying (LPTV) switches in CMOS across RF to millimeter-wave frequencies. [26, 28] achieved +90°/-90° non-reciprocal phase shifting by implementing these non-reciprocal circuits through the characteristics of n-path filters. Through an ingenious switching circuit, spatiotemporal conductance modulation [27] was realized, allowing the circulator to operate at higher frequencies and lower power consumption. Additionally, there are more simple and direct methods to achieve non-reciprocal phase shifting, such as using a gyrator [35] or varactor [45]. [35] realizes the non-reciprocity of forward and reverse signals by controlling the tap direction of the transformer.

2.3.1. N-path filter based

N-path filters have emerged as a potential answer for creating adjustable, high-quality factor filters at RF band, capitalizing on the capabilities of nanoscale CMOS IC technology [28, 46, 47, 48]. These belong to a category of LPTV networks that cyclically channel signals using passive transistor switches through an array of capacitors. This process results in a second-order band-pass filter profile, achieved by converting the low-pass filtering effect of the capacitor to a center frequency defined by the clock frequency. It has been observed that inducing a relative phase shift between the non-overlapping clocks that govern the input and output switch sets of a two-port N-path filter introduces a non-reciprocal phase shift. The signals moving in forward and reverse directions encounter this shift due to the disparate sequencing of the phase-shifted switches they come across. Despite this, the magnitude response remains reciprocal, and the filter retains its low-loss tunability, similar to conventional N-path filters shown in Fig. 2.8.

The switches and capacitor loads (CLs) in Fig. 2.8 can be modeled as parametric modulators and low-pass filters, as shown in Fig. 2.9. The low-pass filter consists of the source impedance, load impedance, and CLs. The signal transmission process can also be understood by considering each group of commutating switches as an in-phase and quadrature reciprocal modulator, which carries out frequency up-conversion and down-conversion [46]. Fig. 2.9 represents signal propagation through the staggered commutated network in both forward and reverse directions. Assuming a cosine input signal at a frequency near the commutation frequency, each switch group can be modeled as an in-phase and quadrature reciprocal modulator that multiplies the input signal with the cosine and sine variants of the pump signal.

The second set of pump signals is assumed to lead the first set by $+90^{\circ}$. The usage of unstaggered commutated networks to create reciprocal comb filters is based on the principle of frequency translation from low-pass filtering to RF using commutating switches. This low-pass filtering significantly dimin-

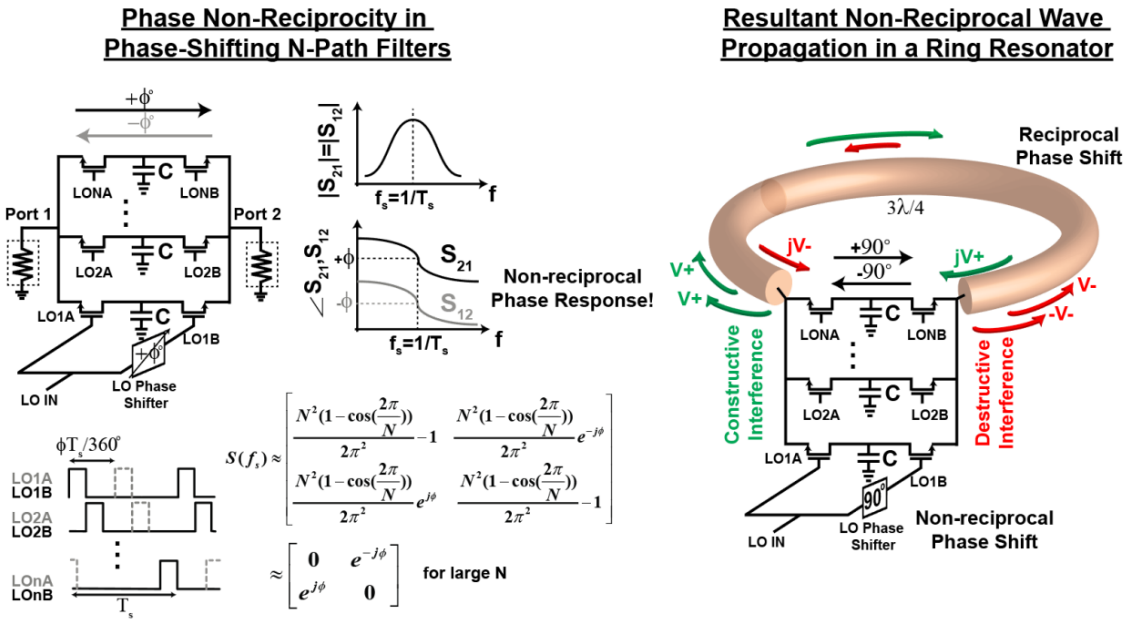

Figure 2.8: Magnetic-free non-reciprocity based on the non-reciprocal phase response of a two-port phase-shifting N-path filter [28].

ishes the up-converted signal after the first modulation. As a result, there is a non-reciprocal phase response for signal transmission in the forward and reverse directions. It is worth noting that while the up-converted frequency components are filtered out, the desired signal does not experience any power loss as the commutated media are purely capacitive. A commutator with at least four paths can be interpreted as a reciprocal in-phase and quadrature frequency converter. The low-pass filters minimize the up-converted components after the first commutation. Consequently, phase non-reciprocity is observed for signals moving in the forward and reverse directions through a staggered commutated network.

Now the non-reciprocal phase shifter is obtained by N-path filter technology. Next, the non-reciprocal phase shifter is embedded into three-quarters of a wavelength loop, as shown in Fig. 2.10. The combined non-reciprocal phase shift of the N-path filter and the reciprocal phase shift of the transmission line allow for one-way wave propagation ($-270° - 90° = -360°$). This is because the boundary condition for wave propagation in the opposite direction cannot be met ($-270° + 90° = -180°$). Furthermore, a three-port circulator can be created if ports are placed at any point along the loop with a quarter wavelength distance between them. This leads to the defined S-parameters at the center operating frequency, as shown in equation (2.4).

$$S_{\text{circ}}\ (f_s) = \begin{bmatrix} 0 & 0 & -1 \\ -j & 0 & 0 \\ 0 & -j & 0 \end{bmatrix} \tag{2.4}$$

[28] has developed a prototype circulator in a 65-nm CMOS process designed to operate between 610-850 MHz. The design incorporates an N-path filter, utilizing eight paths. Each quarter-wavelength transmission line is substituted with an integrated Capacitor-Inductor-Capacitor (CLC) section, with off-chip inductors deployed to enhance the quality factor. Experimental results revealed a transmission loss of 1.7 dB between TX-Antenna and Antenna-RX. However, broadband isolation exceeding 15 dB between TX and RX was achieved (up to 50 dB in narrowband isolation when using an antenna tuner). The in-band IIP3 for Antenna-Rx and TX-Antenna measured at +8.7 dBm and +27.5 dBm, respectively.

To enhance the Q-factor of the quarter-wavelength transmission line, the circuit design employed off-chip inductors, which, however, enlarged the overall circuit footprint. The prototype has difficulty handling situations where the antenna port is not optimally matched. If the impedance of the antenna port deviates from the ideal $50\,\Omega$, it upsets the circuit balance, which results in reduced isolation and increased insertion loss. In response to this issue, subsequent iterations of the circuit [48, 49] design

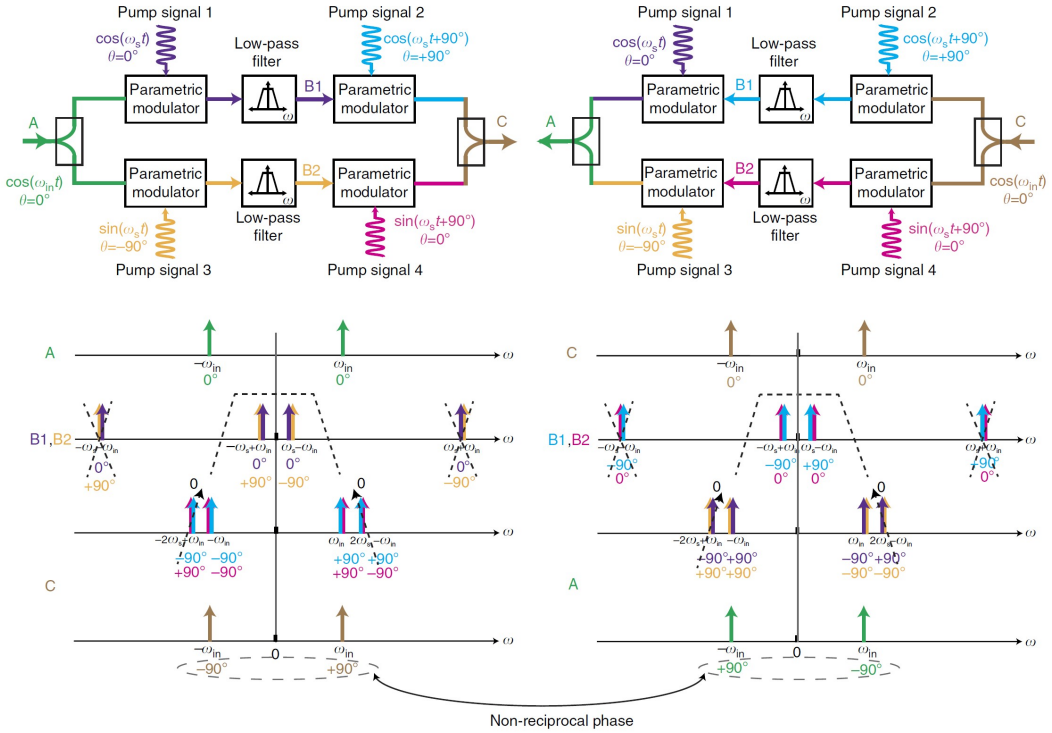

Figure 2.9: The principle of implementing non-reciprocity by N-path filters [46].

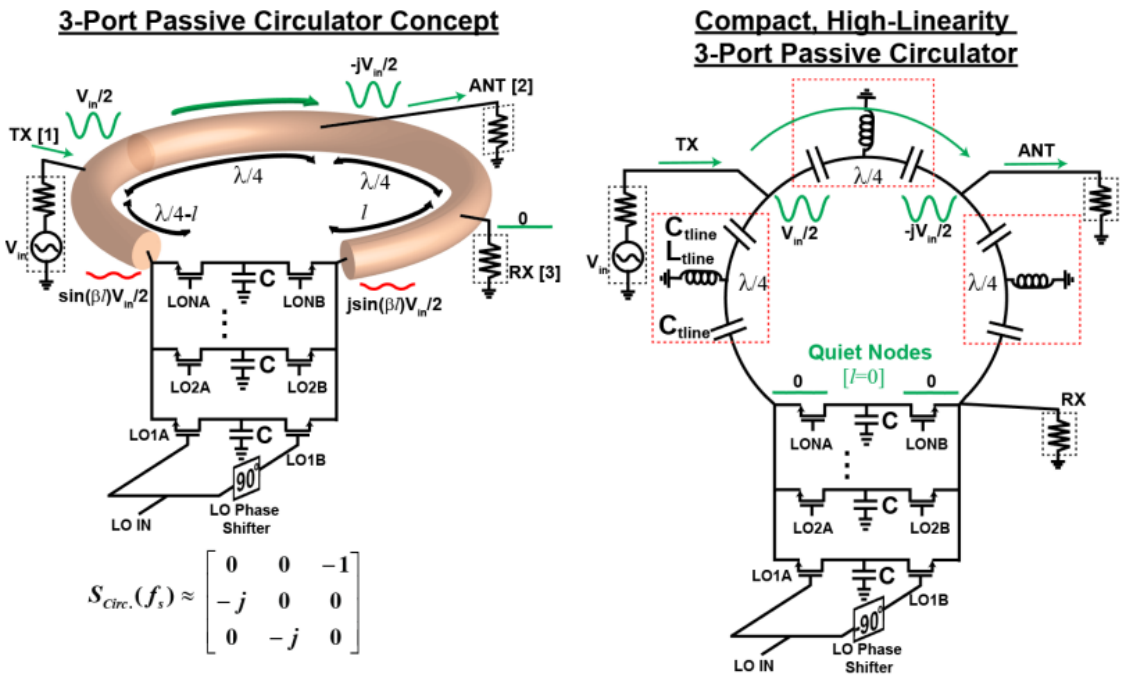

Figure 2.10: The magnetic-free N path-filter-based non-reciprocal circulator [28].

incorporated a balance network at one end of the N-path filter, as shown in Fig. 2.11. This addition addressed the negative impact on circuit performance caused by switch resistance (R_{sw}) and parasitic capacitance. However, it was found that the balance network was ineffective in restoring performance for antenna port conditions that were not $50\,\Omega$. In particular, isolation and insertion loss were not improved. It is worth noting that the circuit leverages the inherent down-conversion property of the N-path filter, extracting the down-converted baseband signal directly from the load capacitor. This approach eliminates the need for a mixer circuit, thereby simplifying the overall design.

Due to the N-path filter's high Q-value characteristic, the circuit effectively suppresses out-of-band interference signals. However, this also limits its ability to support wide operating bandwidths, making it unsuitable for wideband UWB circuits. The circuit's primary drawback lies in its power consumption, necessitating a periodic local oscillator signal to drive 8 or 16 switches. For example, the non-magnetic circulator based on the N-path filter in [50] operates in the range of 0.55 to 0.9 GHz, but its power consumption is as high as 24 mW. Moreover, according to equation $Power = CV^2f$, the power consumption will increase as the frequency rises. In addition, the intrinsic loss of the N-path filter is related to the number of its branches, as shown in Table 2.1. To achieve lower loss, a larger value of N is preferable. However, this also means more CLs and parasitic capacitance, increasing the circuit power consumption. Therefore, N is typically chosen to be 4 or 8. Another point of concern, not elaborated in the referenced articles [48, 49], is the impact of local oscillator signal phase noise on receiver noise. Securing a clean local oscillator signal, especially at high operating frequencies, represents a significant challenge.

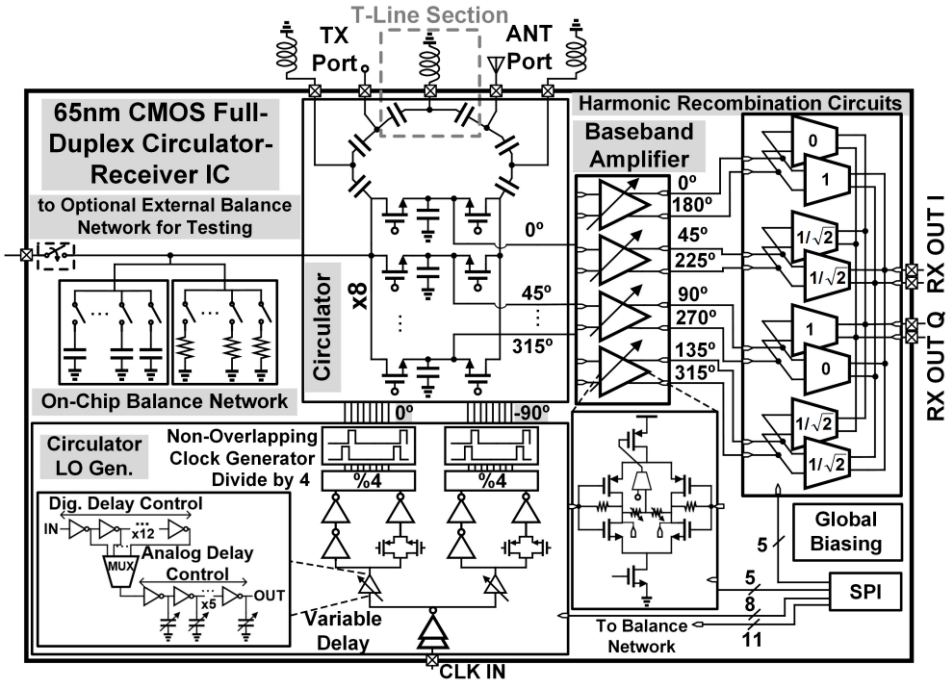

Figure 2.11: The highly linear integrated magnetic-free N-path-filter-based full-duplex circulator-receiver [48].

Table 2.1: Loss Parameters of N-Path Filter

N	$\frac{1}{N}$	$Loss = \mathrm{sinc}^2\left(\frac{1}{N}\right)$
4	0.25	1.83 dB
8	0.125	0.45 dB
16	0.0625	0.11 dB

2.3.2. Spatiotemporal Conductance Modulation

Inspired by the N-path filter-based low-RF CMOS circulator, [51, 52] have proposed a nearly 28-GHz, fully integrated passive circulator, using a 45-nm SOI CMOS, as shown in Fig. 2.12. This innovative design is based on an expanded concept of spatiotemporal conductivity modulation. Similar to the N-path, filter-based staggered commutation, this concept achieves phase nonreciprocity. However, it utilizes a modulation frequency that is significantly lower than the operational frequency—only a third in this case—which enables the possibility of mm-wave operation and dramatically improves bandwidth. Additionally, the lowered local oscillator frequency correspondingly reduces circuit power consumption and complexity of the clock signal. A differential implementation also minimizes the LO leakage, enhancing power handling.

Building on this foundation, [53] have developed a non-magnetic CMOS 60 GHz circulator based on spatio-temporal conductivity modulation (STCM) across a loss/dispersion-engineered bandpass filter. Leveraging a fully passive architecture based on LC all-pass filters, [54] has enhanced the bandwidth of the circulator while achieving low power consumption. The circuit operates at a central frequency of 6.5 GHz, possessing a fractional bandwidth of 28%, and it features a 2.2 dB insertion loss, 2.4 dB noise figure, and 18 dB isolation, all while consuming only 2.5 mW of core power. These results are credited to the fully passive architecture based on LC all-pass filters, which permit a 1.6-fold increase in fractional bandwidth and the lowest power consumption, all within a core area of merely $0.45\,mm^2$.

The idea of spatiotemporal conductivity modulation is illustrated in Fig. 2.13. This concept involves two sets of differential mixer-quad switches situated on both sides of a differential transmission-line delay. The switches are triggered at a modulation frequency called ω_m. The transmission line delay is a crucial factor that is equivalent to a quarter of the modulation period ($T_m/4$).

The switches on the left and right sides are controlled by square-wave clocks with a 50% duty cycle, but the clocks on the right side are delayed by $T_m/4$ compared to the ones on the left side. As a result, waves traveling from left to right will go through the transmission-line delay without any changes in polarity during the first half of the clock period. In the second half of the clock period, they will undergo two polarity changes that negate each other, as depicted in Fig. 2.13(a).

On the other hand, when waves move from right to left, they experience the transmission-line delay and a single sign flip during each half of the clock period, as shown in Fig. 2.13(b). This indicates that transmission in both directions is completely lossless. Additionally, there is a non-reciprocal phase difference of 180°, which is shown to be infinitely broadband in Fig. 2.13(c).

Similar to the N-path filter-based non-magnetic circulator circuit, spatiotemporal conductivity modulation also falls into the category of linear periodically time-varying (LPTV) circuits. These types of circuits require accurate local oscillator signals to control the switches in the circuit, increasing their complexity. The core CLC circuit demands a substantial chip area. Moreover, during the spatiotemporal conductivity modulation process, to enhance return loss and reduce insertion loss, the circuit needs to employ a differential structure rather than a single-ended one [55]. As a result, a balun circuit must be added to single-ended ports, such as antenna ports, to convert single-ended to differential. This addition increases the overall insertion loss of the circuit and the chip area. Further, when there is a mismatch at the antenna end, the insertion loss and isolation of the circulator are significantly impacted.

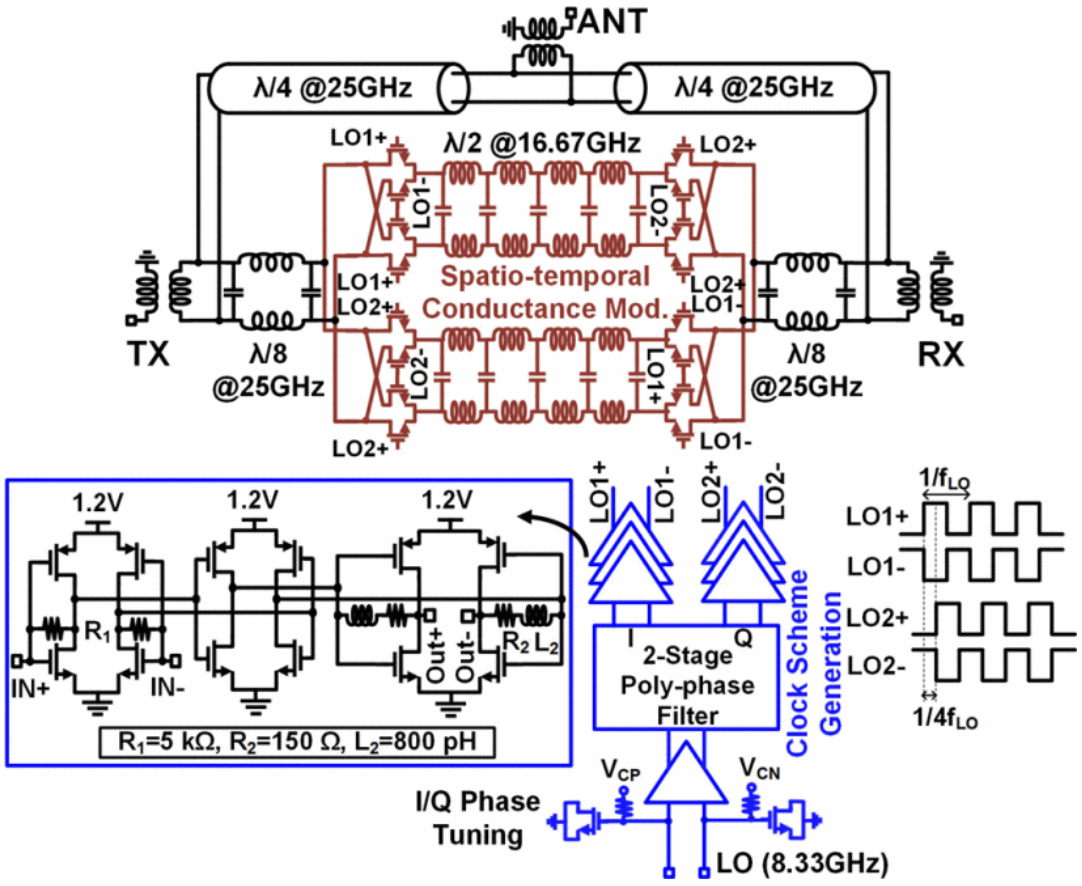

Figure 2.12: The 28GHz magnetic-free non-reciprocal passive 45nm sol CMOS circulator[51].

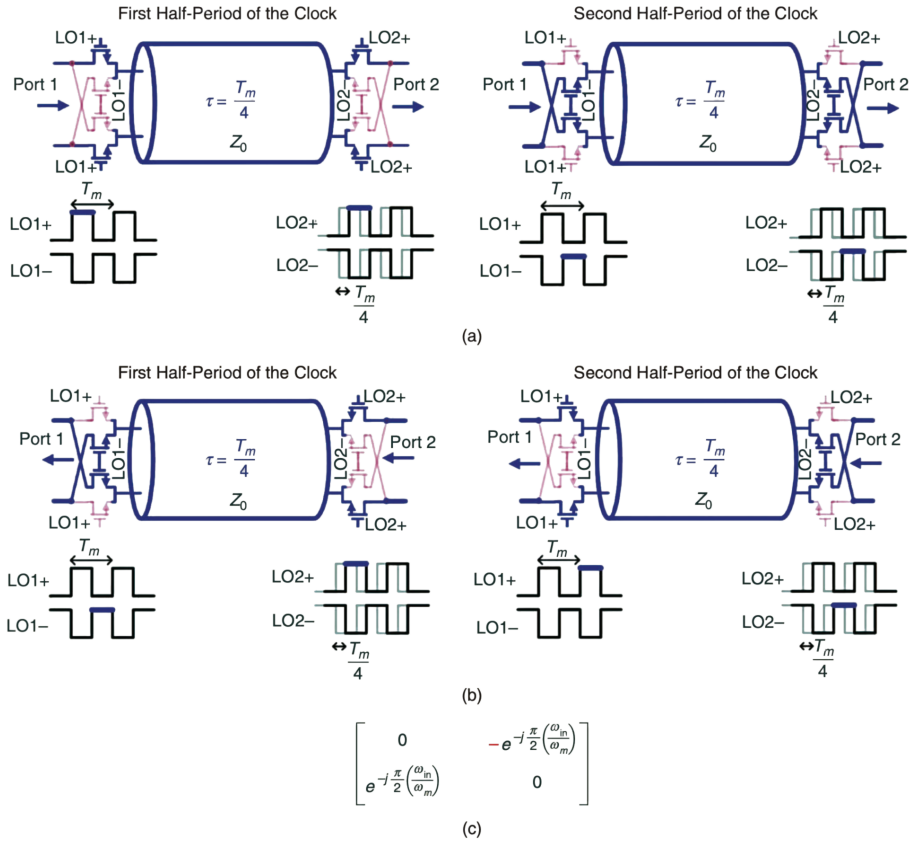

Figure 2.13: The non-reciprocal phase shifting in spatiotemporal (a) Propagation in the forward direction, (b) Propagation in the reverse direction, and (c) The S-parameters [19].

3

The Propoese Full Duplexer

The project details outlined in section 1.3.2 indicate that the Power Amplifier (PA) has a maximum output power of 8 dBm. This significantly differs from regular wireless communication, where transmission power is close to 1 W. As a result, less stringent performance is required under high-signal conditions. In this project, the duplexer is integrated into the UWB transceiver, and the total power consumption of the entire UWB transceiver is less than 50 mW. The duplexer cannot consume too much power, and it is expected that the power consumption of the duplexer is about one-tenth of the total transceiver power consumption, around 5 mW.

As a passive device, the Electrical Balance Duplexer (EBD) provides an appealing option given its low power consumption and superior large-signal performance. However, the EBD's inherent 3 dB loss combined with an approximate 1 dB loss from the transformer, results in a deterioration of around 4 dB in both the transmission link and noise figure within the 6-9 GHz working frequency range.

A non-magnetic approach based on Spatiotemporal Conductance Modulation has the potential to achieve low power consumption and satisfactory small and large signal performance at higher frequencies. But this technology is performed in a differential circuit to improve its performance [36], and both the receiver and antenna ends of the UWB chip only process single-ended signals, with the PA output being the only differential signal. Consequently, implementing this approach would necessitate two extra baluns at both the receiver and antenna to transition single-ended signals into differential ones. This not only augments the chip area but also induces additional insertion loss. Moreover, similar to the non-magnetic circulator based on the N-path filter, this type of circuit is also sensitive to changes in the antenna VSWR. Furthermore, generating a precise, low-phase noise local oscillator signal presents its own set of challenges.

3.1. The Principle of Gyrator-Enhanced Electrical Balanced Duplexer

As mentioned before, the optimal circuit structure would involve the design of a low-power non-reciprocal device built on the EBD platform, which would then be employed to create a non-magnetic circulator. This approach would balance low power consumption and minimal chip area usage while achieving a low insertion loss and excellent isolation at wideband frequency. This section will provide a detailed overview of the evolution process from traditional EBD circuits to ideal Gyrator-Enhanced Electrical Balanced Duplexer (GE-EBD) circuits.

3.1.1. The Lossless EBD

The signal flow in a typical EBD is depicted in Fig. 3.1. Only a portion of the signal is transmitted through the antenna, while the rest is lost through the balance network. If it were possible to collect the signal lost through the balance network to the ground, the intrinsic loss of the EBD could be eliminated.

The most intuitive method for improvement is to remove the BAL and merge the signal transmitted from the TX to the ANT, as shown in Fig. 3.2(a). Once the signal is transmitted and goes through the hybrid transformer, it is separated into two paths: in-phase and out-of-phase. After going through a transmission line with a length of 180°, the out-of-phase signal is transformed into the in-phase. In this way, the signal can be merged using a power combiner and output to the antenna. However, the signal

received by the antenna is now split into two paths by the power splitter. Both signals are in phase, but one of the in-phase signals becomes Out phase after passing through the $180°$ transmission line. Thus, these two signals will cancel out at the LNA input, and RX will not receive any signal. Similarly, if the $180°$ transmission line is changed to a $0°$ transmission line, the antenna will not obtain the output signal from the PA, even though RX can normally receive the signal from the antenna, as shown in Fig. 3.2(b). In conclusion, since the signal is transmitted in a loop, assuming that the devices in the figure are ideal, the insertion loss will be 0 dB. However, this circuit can only achieve FDD functionality, meaning that it can either transmit or receive signals depending on the phase characteristics of the transmission line in Fig. 3.2 [44].

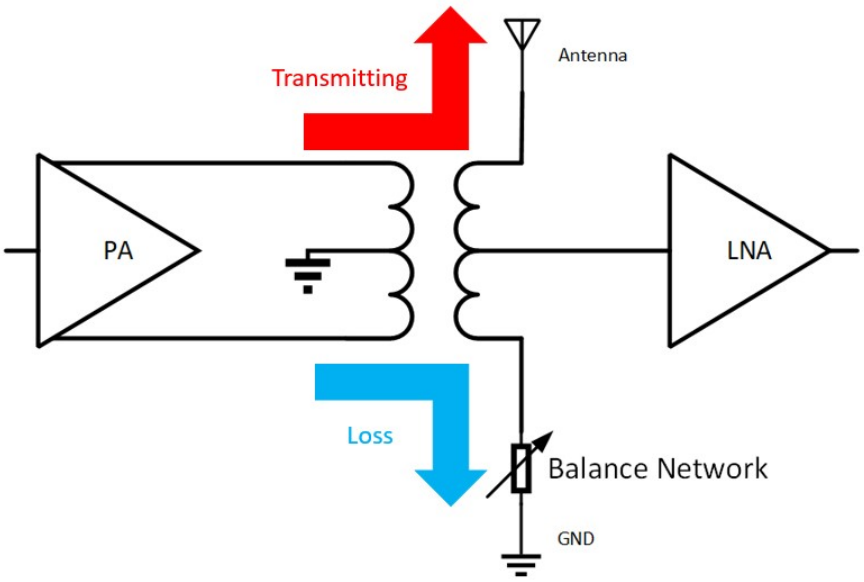

Figure 3.1: The signal power flow in a typical EBD.

3.1.2. The Block Diagram of GE-EBD

Based on the two modes of the circuit above and incorporating the non-reciprocal phase shifter in the non-magnetic circulator, it seems possible to achieve Full Duplexing (FD) by simply substituting the transmission line or phase shifter in Fig. 3.2 with a non-reciprocal phase shifter. This resolves the issue of full duplexing. However, there is another problem: how to compensate when there is an impedance mismatch at the antenna port. This cannot be achieved using a power splitter (in fact, if only the non-reciprocal phase shifter is used to replace the fixed phase shifter and the power splitter is retained, this structure is very similar to the non-magnetic circulator). However, if a hybrid coupler is used to replace the power splitter, and the additional port of the hybrid coupler is connected to BAL, it may be possible to compensate for the impedance mismatch at the antenna port. Hence, by making these changes, a new circuit is created. Then, we need to focus on:

- Designing a low-power $+90°/-90°$ gyrator to replace the fixed phase shifter.
- The hybrid coupler can compensate for mismatch at the antenna port and provide a fixed phase shifting. This allows the original non-reciprocal phase shift of $0°/180°$ to be revised to a non-reciprocal phase shift of $+90°/-90°$. In addition, the hybrid coupler can be implemented with a transformer in RF IC design. And compared to implementing phase shifters with transmission lines, it occupies a smaller area and has a wider operating bandwidth.

The block diagram of the proposed circuit, gyrator-enhanced electrical balance duplexer (GE-EBD), is shown in Fig. 3.3. A hybrid transformer connected to the antenna fulfills the function of the original EBD circuit. The hybrid transformer within the diagram accomplishes the task of creating electrical balance and converting the differential signal from the TX into a single-ended signal. Meanwhile, a

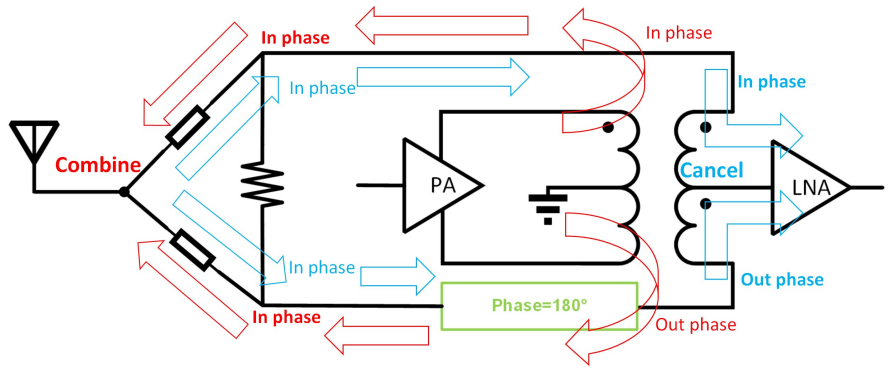

(a) Signal flow in TX mode.

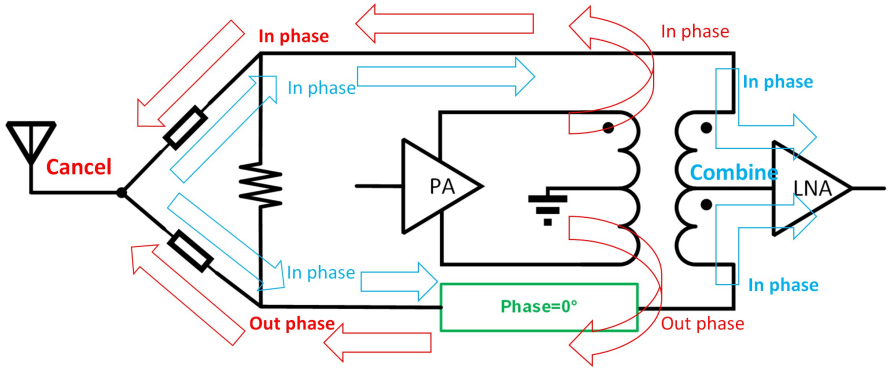

(b) Signal flow in RX mode.

Figure 3.2: The signal flow diagram in a lossless duplexer. (a) The transmitting signal is split into two equal power signals, with a phase difference of 180° after passing through the hybrid transformer. One signal directly enters the antenna port, while the other requires phase adjustment via a 180° transmission line or phase shifter before entering the antenna port. The two signals are superimposed at the antenna port. (b) During the process of receiving signals, the antenna receives a signal and splits it into equal halves using a power splitter. These halves are then fed into the hybrid transformer, and at the RX, they are in phase, resulting in a combination at the RX port.

hybrid coupler takes over the function of the initial power splitter. The balance network connected to the hybrid coupler compensates for the antenna's impedance mismatch. This hybrid transformer can be realized using a transformer with a high coupling coefficient, thereby fulfilling the function of a traditional EBD circuit. The non-reciprocal phase shifter enables full duplexing and determines the power consumption and noise of the duplexer. As shown in Fig. 3.4, the signal flow diagram explains how GE-EBD achieves lossless full duplexing. Detailed analysis of this can be conducted using S-parameters.

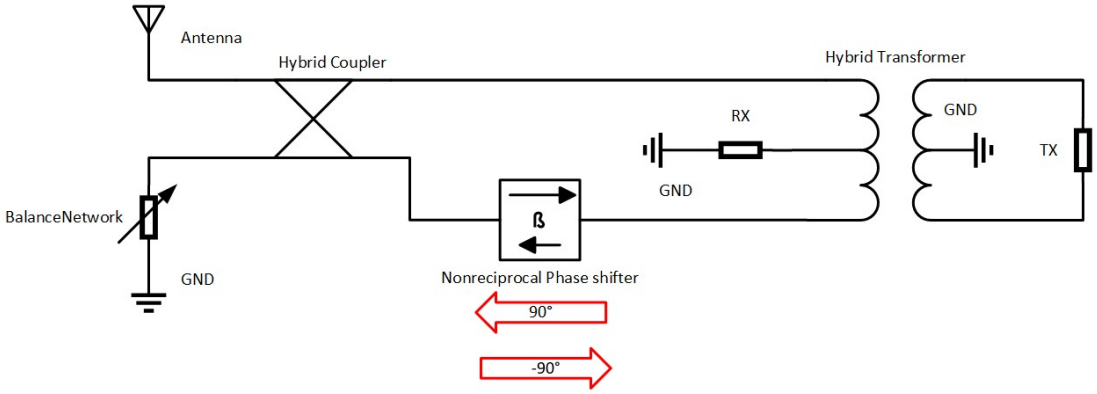

Figure 3.3: The block diagram of the proposed duplexer.

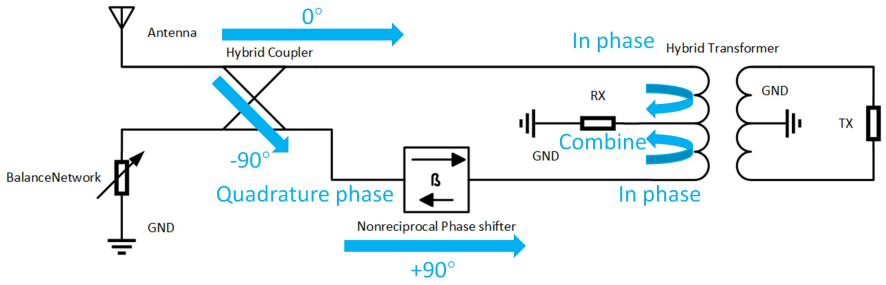

(a) Receiving.

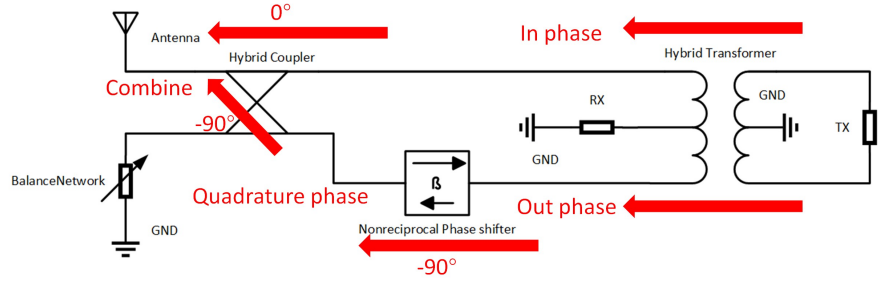

(b) Transmitting.

Figure 3.4: The signal power flow in the proposed duplexer. During reception, the signal is superimposed at the RX. Conversely, during transmission, the signal is superimposed at the antenna port.

3.2. Model and Analysis

In order to analyze the isolation and insertion loss of the proposed duplexer, the simplest method is to conduct a small-signal analysis using S-parameters. To simplify calculations, the model in Fig. 3.3 is simplified, as shown in Fig. 3.5. Here, $[SB]$ represents the hybrid coupler, $[SA]$ signifies the hybrid transformer, and $[SP]$ represents the non-reciprocal phase shifter. $[aB]$ represents the incident wave of the hybrid coupler, and $[bB]$ represents the reflected wave of the hybrid coupler. $[aA]$ represents

the incident wave of the hybrid transformer, and $[bA]$ represents the reflected wave of the hybrid transformer, as shown in Fig. 3.5. To simplify calculations, it is assumed that the magnitude of the return loss is zero at each port of the hybrid coupler, non-reciprocal phase shifter, and hybrid transformer. Using the definition of S-parameters, the equation is as follows:

$$\begin{aligned}[bB] &= [SB][aB], \\ [bA] &= [SA][aA].\end{aligned} \tag{3.1}$$

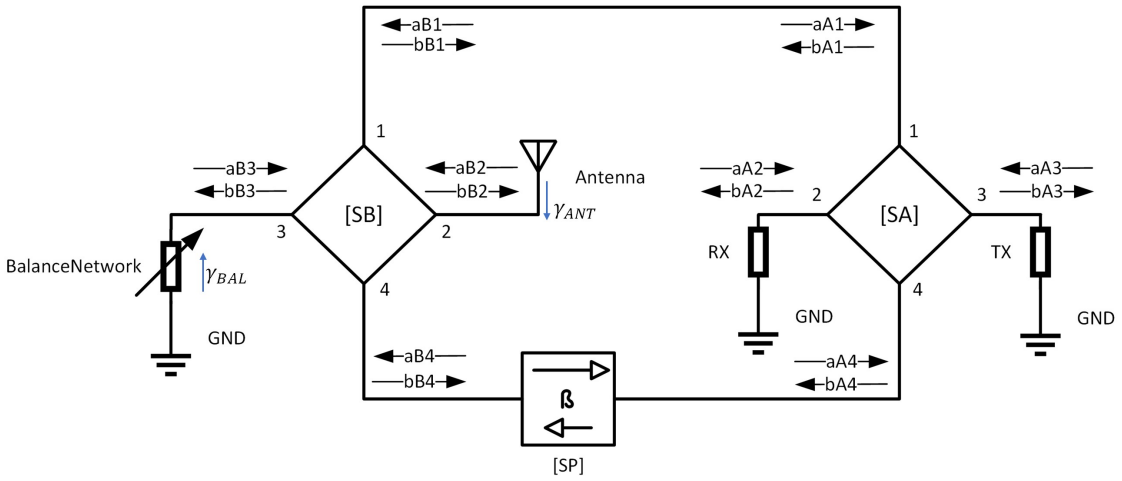

Figure 3.5: The S-parameter analysis of the proposed duplexer.

For the ideal hybrid transformer and non-reciprocal phase shifter, their S-parameters are equation (3.2) and equation (3.3), respectively:

$$[SA] = \begin{pmatrix} 0 & \frac{1}{\sqrt{2}} & \frac{1}{\sqrt{2}} & 0 \\ \frac{1}{\sqrt{2}} & 0 & 0 & \frac{1}{\sqrt{2}} \\ \frac{1}{\sqrt{2}} & 0 & 0 & -\frac{1}{\sqrt{2}} \\ 0 & \frac{1}{\sqrt{2}} & -\frac{1}{\sqrt{2}} & 0 \end{pmatrix} \tag{3.2}$$

$$[SP] = \begin{pmatrix} 0 & -j \\ j & 0 \end{pmatrix} \tag{3.3}$$

Only the S-parameters of the hybrid coupler, represented as $[SB]$, remain unknown. Based on specific requirements, different types of hybrid couplers can be chosen.

3.2.1. $90°$ Hybrid Coupler based

By examining the block diagram of a hybrid coupler, it can be inferred that utilizing various types of hybrid couplers will yield unique outcomes. Initially, the most basic type, the most basic type - $90°$ hybrid coupler - is implemented. The corresponding S-parameter matrix for the $90°$ hybrid coupler can be found in equation (3.4).

$$[SB] = \begin{pmatrix} 0 & -j\frac{1}{\sqrt{2}} & -\frac{1}{\sqrt{2}} & 0 \\ -j\frac{1}{\sqrt{2}} & 0 & 0 & -\frac{1}{\sqrt{2}} \\ -\frac{1}{\sqrt{2}} & 0 & 0 & -j\frac{1}{\sqrt{2}} \\ 0 & -\frac{1}{\sqrt{2}} & -j\frac{1}{\sqrt{2}} & 0 \end{pmatrix} \tag{3.4}$$

In terms of the isolation from the TX to RX, the signal a_{A3} output from the transmitter (TX) and the signal b_{A2} input to the receiver (RX) are considered. The ratio of these signals corresponds to the TRANSMISSION or LEAKAGE from TX to RX, which is the inverse of the isolation.

$$TRANSMISSION_{TX-RX} = \frac{b_{\mathrm{A2}}}{a_{\mathrm{A3}}} \tag{3.5}$$

$$TRANSMISSION_{TX-RX} = \frac{1}{ISOLATION_{TX-RX}} \tag{3.6}$$

The following equations can be obtained from Fig. 3.5. To simplify the calculations, assume that the RX end is perfectly matched, resulting in a reflection signal of 0 at the RX.

$$b_{\mathrm{A1}} = a_{\mathrm{B1}} \tag{3.7}$$

$$b_{\mathrm{B1}} = a_{\mathrm{A1}} \tag{3.8}$$

$$a_{\mathrm{B3}} = \gamma_{\mathrm{bal}} \cdot b_{\mathrm{B3}} \tag{3.9}$$

$$a_{\mathrm{B2}} = \gamma_{\mathrm{ant}} \cdot b_{\mathrm{B2}} \tag{3.10}$$

$$a_{\mathrm{B4}} = \mathrm{SP}_{12} \cdot b_{\mathrm{A4}} \tag{3.11}$$

$$a_{\mathrm{A4}} = \mathrm{SP}_{21} \cdot b_{\mathrm{B4}} \tag{3.12}$$

$$a_{\mathrm{A2}} = 0 \tag{3.13}$$

Upon integrating equation (3.1), (3.7)-(3.13) into equation (3.5), the $TRANSMISSION_{TX-RX}$ can be established as follows:

$$TRANSMISSION_{TX-RX} = \frac{\left((-\mathrm{SB}_{42}^2\gamma_{\mathrm{ant}} - \mathrm{SB}_{43}^2\gamma_{\mathrm{bal}})\right)\mathrm{SP}_{21} - \mathrm{SB}_{21}\mathrm{SB}_{42}\gamma_{\mathrm{ant}} - \mathrm{SB}_{31}\mathrm{SB}_{43}\gamma_{\mathrm{bal}}}{2}\mathrm{SP}_{12} + \frac{(\mathrm{SB}_{21}\mathrm{SB}_{42}\gamma_{\mathrm{ant}} + \mathrm{SB}_{31}\mathrm{SB}_{43}\gamma_{\mathrm{bal}})\mathrm{SP}_{21}}{2} + \frac{\mathrm{SB}_{21}^2\gamma_{\mathrm{ant}}}{2} + \frac{\mathrm{SB}_{31}^2\gamma_{\mathrm{bal}}}{2} \tag{3.14}$$

Thus, by substituting the known S-parameters of the hybrid transformer, hybrid coupler, and non-reciprocal phase shifter into equation (3.14), the ideal $TRANSMISSION_{TX-RX}$ can be calculated as follows:

$$TRANSMISSION_{TX-RX} = -\gamma_{\mathrm{ant}} \tag{3.15}$$

Equation (3.15) shows that under ideal conditions, $TRANSMISSION_{TX-RX}$ or isolation depends solely on the reflection coefficient of the antenna port. If the antenna port is matched to $50\,\Omega$, the $TRANSMISSION_{TX-RX}$ is zero, meaning no signal is transmitted from the transmission port to the receiving port. However, any mismatch at the antenna port would deteriorate the isolation, which the balance network cannot compensate for.

Next, we calculate the insertion loss at the RX, which is the ratio of the signal b_{A2} output to the RX port and the signal a_{B2} input from the antenna port:

$$RXIL = \frac{\mathrm{b}_{A2}}{\mathrm{a}_{B2}} \tag{3.16}$$

To simplify the calculation, assuming that the TX port is matched:

$$\mathrm{a}_{A3} = 0 \tag{3.17}$$

Similar to the calculation of $TRANSMISSION_{TX-RX}$, substituting equation (3.7),(3.8),(3.9),(3.11),(3.12),(3.13) and (3.17) into equation (3.16), $RXIL$ can be derived:

$$RXIL = \frac{\sqrt{2}(SB_{42}SP_{21} + SB_{21})}{2} \tag{3.18}$$

After substituting the S-parameters, the result for $RXIL$ is:

$$RXIL = -j \Rightarrow \text{loss} = 0\,dB \tag{3.19}$$

Based on equation (3.19), assuming ideal conditions where there is no loss from each hybrid coupler, hybrid transformer, and non-reciprocal phase shifter, and no mismatches at each port, the signal from the antenna to the receiver only has a phase difference of $-90°$. Using similar steps, the insertion loss from the TX port to the antenna port can be calculated:

$$TXIL = \frac{\sqrt{2}(-SB_{42}SP_{12} + SB_{21})}{2} \tag{3.20}$$

$$TXIL = -j \Rightarrow \text{loss} = 0\,dB \tag{3.21}$$

3.2.2. Phase and Amplitude Mismatch of Non-reciprocal Phase Shifter

The above result is based on the assumption that the non-reciprocal phase shifter has no phase mismatch and there are no losses during forward and reverse transmissions. Next, we will analyze the case where the non-reciprocal phase shifter is not ideal.

Firstly, assuming that the non-reciprocal phase shifter suffers from some phase mismatch, its S-parameters $[SP]$ can be described as follows:

$$[SP] = \begin{pmatrix} 0 & -j \\ je^{j\phi} & 0 \end{pmatrix} \tag{3.22}$$

Following the steps outlined above, the relation between phase mismatch and transmission can be calculated:

$$TRANSMISSION_{TX-RX} = -\gamma_{\text{ant}} \frac{e^{j\phi} + 1}{2} \tag{3.23}$$

According to equation (3.23), it can be observed that when there is a phase mismatch, the $TRANSMISSION_{TX-RX}$ is not only dependent on the reflection coefficient at the antenna port but also on the value of the phase mismatch. It is known that the absolute value of the product of two complex numbers will not exceed the product of their absolute values. Therefore, it contributes to increased isolation from TX to RX. By extracting the second term $\frac{e^{j\phi}+1}{2}$ in the equation (3.23), excluding the antenna reflection coefficient, and plotting it, the results are shown in Fig. 3.6 (a). When there is no phase mismatch ($\phi = 0°$), the extra isolation provided by the phase mismatch is 0 dB. At $\pm 90°$, the extra isolation is 3 dB. Similar conclusions can be drawn when phase mismatch occurs at S_{12}. In short, phase mismatch does not degrade isolation. It improves isolation from transmitter to receiver, but what is the cost? The following analysis will discuss the impact of phase mismatch on insertion loss.

Using the same approach, the $RXIL$ can be obtained, as shown in equation (3.24) and Fig. 3.6 (b). When the phase mismatch is $0°$, $RXIL$ (Receiver Insertion Loss) is 0 dB. However, as the phase mismatch increases, $RXIL$ gradually deteriorates. $TXIL$ remains the same as given by equation (3.21) in this condition. This is because only S_{21} changes while S_{12} remains the same. According to the signal flow diagram in Fig. 3.4b, the transmitted signal is unaffected. Similar conclusions can be obtained if the phase mismatch occurs at S_{12}. $TXIL$ deteriorates while $RXIL$ remains unchanged.

$$RXIL = -\frac{j}{2}(e^{j\phi} + 1) \tag{3.24}$$

Next, the effect of amplitude mismatch in the non-reciprocal phase shifter on the performance of the duplexer needs to be analyzed. Similar to the previous analysis approach, start with a simple assumption:

$$[SP] = \begin{pmatrix} 0 & -j \\ AMj & 0 \end{pmatrix} \tag{3.25}$$

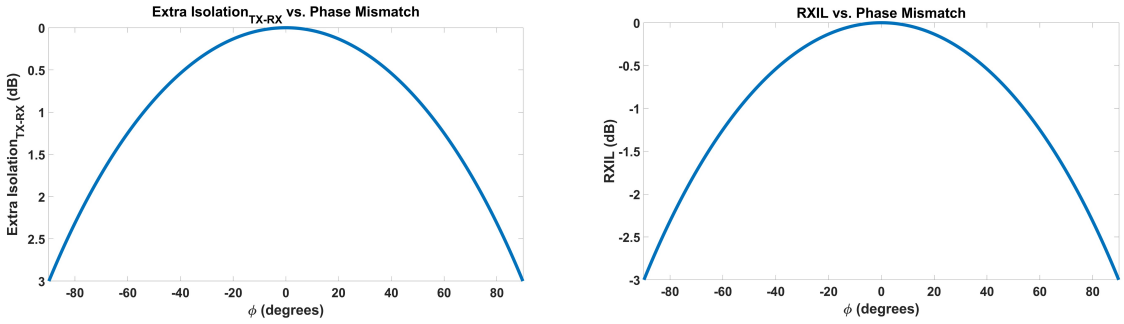

(a) (b)

Figure 3.6: The influence of phase mismatch. (a) The additional $Isolation_{TX-RX}$ is caused by phase mismatch. (b) The relation between $RXIL$ and phase mismatch.

The amplitude of S_{21} decreases by a factor of AM. The transmission (or isolation) and $RXIL$ can be calculated accordingly, as shown in equation (3.26) (3.27) and Fig. 3.7. The additional isolation caused by the amplitude mismatch of the non-reciprocal phase shifter is depicted in Fig. 3.7 (a), while its $RXIL$ is shown in Fig. 3.7 (b). The behavior of $TXIL$ is similar to that of phase mismatch, where $TXIL$ deteriorates only when amplitude mismatch occurs in S_{12}.

$$TRANSMISSION_{TX-RX} = -\gamma_{\text{ant}} \frac{AM+1}{2} \tag{3.26}$$

$$RXIL = -j\frac{AM+1}{2} \tag{3.27}$$

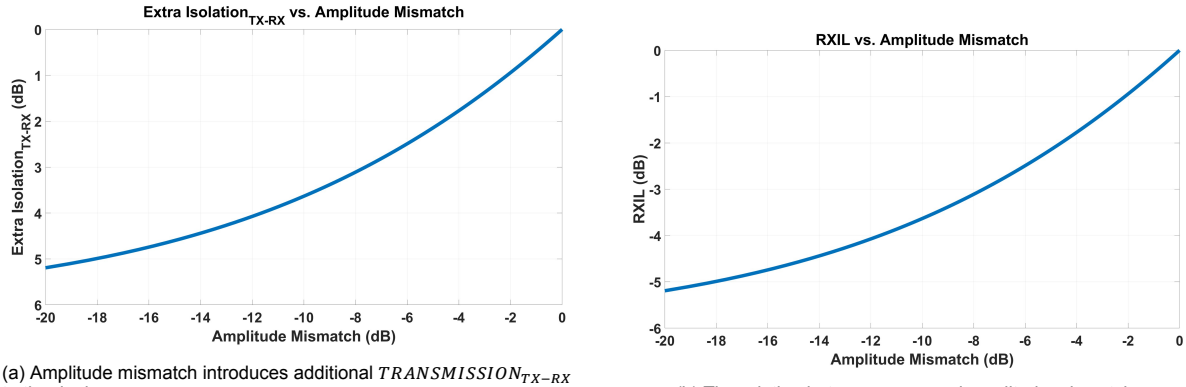

(a) Amplitude mismatch introduces additional $TRANSMISSION_{TX-RX}$ to the duplexer.

(b) The relation between $RXIL$ and amplitude mismatch.

Figure 3.7: Effects of amplitude mismatch on the duplexer

In summary, the non-reciprocal phase shifter's variations in phase and amplitude are reflected in the $Isolation_{TX-RX}$ and insertion loss. While they improve the duplexer's performance by introducing extra $Isolation_{TX-RX}$, they also worsen the insertion loss. Due to the unidirectional nature of the non-reciprocal phase shifter, changes in S_{21} only affect $Isolation_{TX-RX}$ and $RXIL$, while changes in S_{12} only affect $Isolation_{TX-RX}$ and $TXIL$.The situation is more intricate than expected because the return loss of practical devices is not zero, leading to a non-unidirectional signal flow diagram as depicted in Fig. 3.4. As a result, changes in S_{21} affect $TXIL$ and changes in S_{12} affect $RXIL$. It is necessary to introduce adjustable components at appropriate locations in the duplexer to compensate for the mismatch.

3.2.3. Phase and Amplitude unbalance of Hybrid Coupler

The amplitude and phase unbalance of the hybrid coupler can also cause changes in the performance of the duplexer. If amplitude and phase unbalance exist in the hybrid coupler, they can be represented by $AUe^{j\theta}$, where AU stands for amplitude and θ stands for phase. The expression $AUe^{j\theta}$ is inserted into the equation: (3.14)(3.18)(3.20):

$$TRANSMISSION_{TX-RX} = -\gamma_{\text{ant}}(\frac{AUe^{j\theta}+1}{2})^2 \tag{3.28}$$

$$RXIL = -j\frac{AUe^{j\theta}+1}{2} \tag{3.29}$$

$$TXIL = -j\frac{AUe^{j\theta}+1}{2} \tag{3.30}$$

According to equation (3.28)(3.29)(3.30), the unbalance of amplitude and phase will bring additional isolation $(\frac{AUe^{j\theta}+1}{2})^2$ to $Isolation_{TX-RX}$. However, this comes with the added cost of increased losses in both the $RXIL$ and $TXIL$, by a factor of $\frac{AUe^{j\theta}+1}{2}$, as shown in Fig. 3.8. This is consistent with the signal flow chart in Fig. 3.4. The hybrid coupler combines the In-phase and Quadrature signals, and the unbalance of amplitude and phase brings about losses during power combination. To minimize the impact of phase or amplitude imbalance, it is important to keep the loss below 1 dB. Therefore, the corresponding phase imbalance should be less than $45°$, and the amplitude imbalance should be less than 2 dB, as shown in Fig. 3.8.

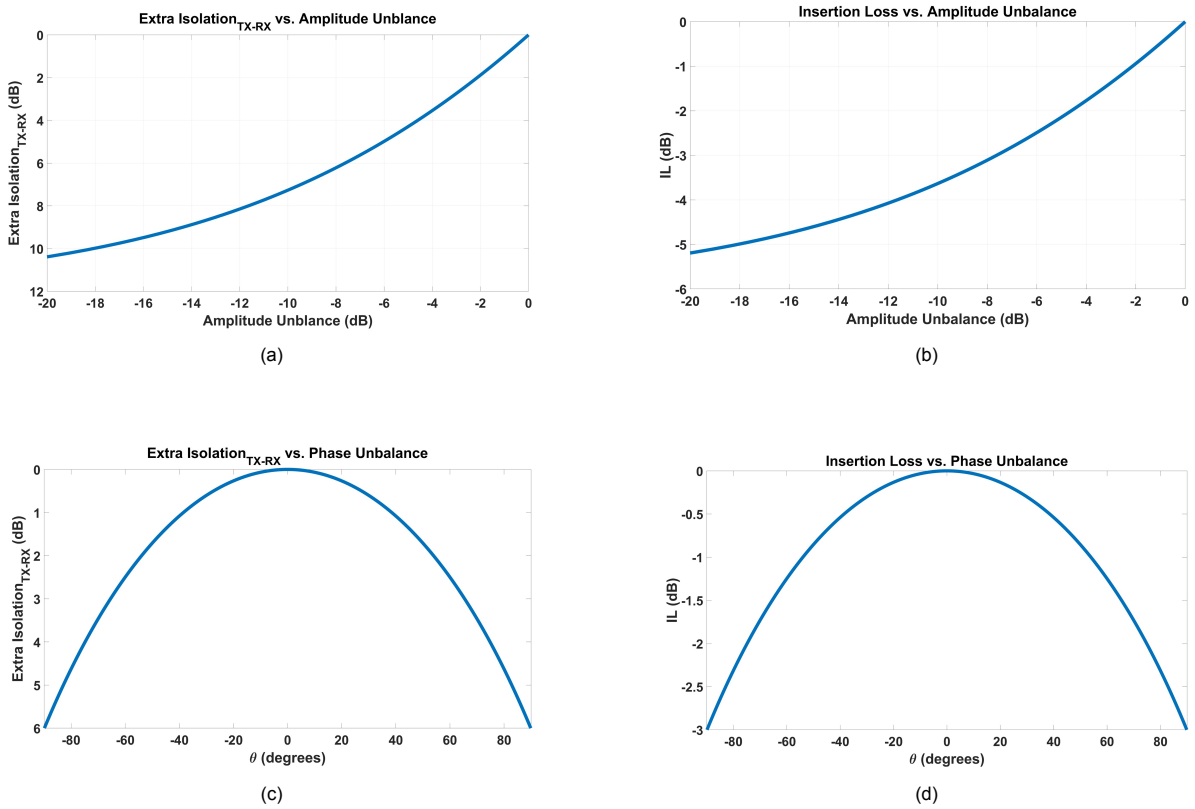

Figure 3.8: When amplitude and phase unbalance exist in the In-phase and Quadrature paths of the hybrid coupler, changes occur in $Isolation_{TX-RX}$ and insertion loss. (a) Additional $Isolation_{TX-RX}$ and amplitude unbalance. (b) Insertion Loss and amplitude unbalance. (c) Additional $Isolation_{TX-RX}$ and phase unbalance. (d) Insertion Loss and phase unbalance.

3.2.4. $45°$ Hybrid Coupler based

Section 3.2.1 shows that theoretically, a lossless GE-EBD can be achieved theoretically if a hybrid coupler is implemented as a $90°$ hybrid coupler. However, the balance network cannot compensate for the mismatch at the antenna port. This is because all the energy split from the TX is recycled back to the antenna port. Without accounting for return loss in those ports, there will be no energy transfer to the balance network. As a result, leveraging the correlated signal to rectify the mismatched signal at the antenna port becomes unfeasible. Therefore, a different type of hybrid coupler is needed to

distribute a small part of the energy to the balance network, ensuring that this portion of the signal is correlated with the signal transmitted to the antenna port. This way, this part of the signal can be used to compensate for the mismatched signal at the antenna port. Equation (3.31) shows that in the GE-EBD with the $45°$ Hybrid Coupler, the incident wave b_{B3} is injected into BAL. In contrast, in the GE-EBD with the $90°$ Hybrid Coupler, the incident wave b_{B3} is not injected into BAL, which confirms the prior analysis. A $45°$ hybrid coupler is used to replace the $90°$ hybrid coupler. The S-parameters of a $45°$ hybrid coupler are shown in equation (3.32). It is worth noting that only the hybrid coupler is changed in GE-EBD. To maintain the functionality of full duplexing, the phase shifting of the non-reciprocal phase shifter remains unchanged, still $+90°/-90°$.

$$b_{B3} = \frac{(\sqrt{2} + (2-\sqrt{2})j) \times b_{B4}}{(1 + (1+\sqrt{2})j) \times \gamma_{\text{ant}} + (\sqrt{2} - 1 + j) \times \gamma_{\text{bal}}} \tag{3.31}$$

$$[SB] = \begin{pmatrix} 0 & 0.5 - 0.5j & -\frac{1}{\sqrt{2}}j & 0 \\ 0.5 - 0.5j & 0 & 0 & -\frac{1}{\sqrt{2}}j \\ -\frac{1}{\sqrt{2}}j & 0 & 0 & 0.5 + 0.5j \\ 0 & -\frac{1}{\sqrt{2}}j & 0.5 + 0.5j & 0 \end{pmatrix} \tag{3.32}$$

By substituting equation (3.32) into equation (3.14),(3.18),(3.20), $TRANSMISSION_{TX-RX}$, $TXIL$, and $RXIL$ can be easily obtained:

$$TRANSMISSION_{TX-RX} = \frac{(\sqrt{2}+1)(1-j)}{4}\gamma_{\text{ant}} + \frac{(\sqrt{2}-1)(1+j)}{4}\gamma_{\text{bal}} \tag{3.33}$$

$$RXIL = \frac{2+\sqrt{2}}{4} - \frac{\sqrt{2}}{4}j \Rightarrow \text{Loss} = 0.68\,dB \tag{3.34}$$

$$TXIL = \frac{2+\sqrt{2}}{4} - \frac{\sqrt{2}}{4}j \Rightarrow \text{Loss} = 0.68\,dB \tag{3.35}$$

From equation (3.33), it can be seen that the $TRANSMISSION_{TX-RX}$ not only depends on the reflection coefficient γ_{ant} at the antenna but also on the reflection coefficient γ_{bal} at the balance network. By adjusting γ_{bal}, it is possible to compensate for the mismatch at the antenna. However, the cost is an increase in insertion loss by 0.68 dB. This is because a small portion of the energy is distributed to the balance network by the $45°$ hybrid coupler to compensate for the mismatch at the antenna port. The next step is to determine the range for compensating for the mismatch in the antenna port.

Firstly, because the reflection coefficients of the antenna γ_{ant} and the balance network γ_{bal} are complex numbers, suppose their values are respectively:

$$\gamma_{\text{ant}} = a + bj \tag{3.36}$$

$$\gamma_{\text{bal}} = X + Yj \tag{3.37}$$

Substitute equations (3.36) and (3.37) into equation (3.33). Set $TRANSMISSION_{TX-RX}$ to zero to obtain the relation between the reflection coefficients of the antenna port and balance network under ideal $TRANSMISSION_{TX-RX}$ conditions.

$$\begin{aligned} X &= (\sqrt{2}+1)^2 \cdot b \\ Y &= -(\sqrt{2}+1)^2 \cdot a \end{aligned} \tag{3.38}$$

The absolute values of the reflection coefficient should be between 0 and 1:

$$X^2 + Y^2 \leq 1 \Rightarrow a^2 + b^2 \leq \frac{1}{(\sqrt{2}+1)^4} \tag{3.39}$$

Finally, The balance network's compensation range for antenna-port mismatches has been determined. The balance network can effectively provide compensation when VSWR is less than 1.5, achieving an $TRANSMISSION_{TX-RX}$ level of zero when VSWR is below 1.4142 and reaching an $TRANSMISSION_{TX-RX}$ level of -30 dB ($ISOLATION = 30\,dB$) when VSWR is between 1.4142 and 1.5.

$$|\gamma_{\text{ant}}| \leq \frac{1}{(\sqrt{2}+1)^2} \Rightarrow VSWR \leq 1.4142 \tag{3.40}$$

3.2.5. $60°$ Hybrid Coupler based

Similarly, by replacing the $45°$ hybrid coupler with a $60°$ hybrid coupler, the compensation range of the Balance Network can be expanded. However, the trade-off is a higher insertion loss. The S-parameters of a $60°$ hybrid coupler are as equation (3.41).

$$[SB] = \begin{pmatrix} 0 & \frac{1}{\sqrt{2}}\left(0.5 - j\frac{\sqrt{3}}{2}\right) & -j\frac{1}{\sqrt{2}} & 0 \\ \frac{1}{\sqrt{2}}\left(0.5 - j\frac{\sqrt{3}}{2}\right) & 0 & 0 & -j\frac{1}{\sqrt{2}} \\ -j\frac{1}{\sqrt{2}} & 0 & 0 & \frac{1}{\sqrt{2}}\left(0.5 + j\frac{\sqrt{3}}{2}\right) \\ 0 & -j\frac{1}{\sqrt{2}} & \frac{1}{\sqrt{2}}\left(0.5 + j\frac{\sqrt{3}}{2}\right) & 0 \end{pmatrix} \tag{3.41}$$

By substituting equation (3.41) into equation (3.14),(3.18),(3.20), $TRANSMISSION_{TX-RX}$, $TXIL$, and $RXIL$ can be easily obtained:

$$TRANSMISSION_{TX-RX} = \left(\frac{3}{8} - \frac{3\sqrt{3}}{8}j\right)\gamma_{\text{ant}} + \left(\frac{1}{8} + \frac{\sqrt{3}}{8}j\right)\gamma_{\text{bal}} \tag{3.42}$$

$$RXIL = TXIL = 1.25dB \tag{3.43}$$

3.2.6. The optimal Transmission

Replacing the $45°$ hybrid coupler with a $60°$ hybrid coupler increases insertion loss from 0.68 dB to 1.25 dB. The balance network's compensatable range also expands. If the VSWR of the antenna is less than 2, the balance network's reflection coefficient can be adjusted to reduce $TRANSMISSION_{TX-RX}$ amplitude to zero, preventing signal energy transfer from TX to RX. Table 3.1 displays the outcomes of utilizing three types of hybrid couplers. The $90°$ hybrid coupler performs the best, but it can't utilize the balance network to compensate for the mismatch at the antenna port. The $60°$ hybrid coupler can provide compensation when the VSWR of the antenna is less than 2, but it inherently has an insertion loss of 1.25 dB.

Table 3.1: Comparison of GE-EBD Performance with Different Hybrid Couplers

	$TRANSMISSION_{TX-RX}$	RXIL (dB)	TXIL (dB)	Compensable Range ($VSWR$)
$45°$ Hybrid Coupler-Based	$= \frac{(\sqrt{2}+1)(1-j)}{4}\gamma_{\text{ant}} + \frac{(\sqrt{2}-1)(1+j)}{4}\gamma_{\text{bal}}$	0.68	0.68	≤ 1.41
$60°$ Hybrid Coupler-Based	$= \left(\frac{3}{8} - \frac{3\sqrt{3}}{8}j\right)\gamma_{\text{ant}} + \left(\frac{1}{8} + \frac{\sqrt{3}}{8}j\right)\gamma_{\text{bal}}$	1.25	1.25	≤ 2
$90°$ Hybrid Coupler-Based	$= -\gamma_{\text{ant}}$	0	0	=1
Note: $Isolation_{TX-RX} = \frac{1}{Transmission_{TX-RX}}$				

Fig. 3.9 illustrates the significant advantages of a GE-EBD that can use BAL to compensate for antenna impedance mismatch. A $90°$ hybrid coupler-based GE-EBD achieves ideal $TRANSMISSION_{TX-RX}$ (or $Isolation_{TX-RX}$) between TX and RX only when $VSWR = 1$. As the antenna's VSWR worsens, $Isolation_{TX-RX}$ deteriorates accordingly, eventually reaching 3 dB. When using a GE-EBD with a $45°$ hybrid coupler or a $60°$ hybrid coupler, it is possible to achieve excellent $Isolation_{TX-RX}$ over a wider

range. This is because these couplers can use BAL to compensate for any antenna impedance mismatch. If the $VSWR$ is less than 1.41, the $45°$ hybrid coupler-based GE-EBD can achieve perfect $Isolation_{TX-RX}$, while the $60°$ hybrid coupler-based GE-EBD can do so when the $VSWR$ is less than 2. Even if the VSWR deteriorates to 1.5, the GE-EBD using a $45°$ hybrid coupler can still provide 30 dB of $Isolation_{TX-RX}$. However, if the VSWR worsens to 2.2, only the GE-EBD using a $60°$ hybrid coupler can achieve 30 dB of $Isolation_{TX-RX}$. In such cases, the performance of the GE-EBD utilizing a $45°$ hybrid coupler declines, and the GE-EBD using a $90°$ hybrid coupler can only offer 15 dB or 8 dB of $Isolation_{TX-RX}$.

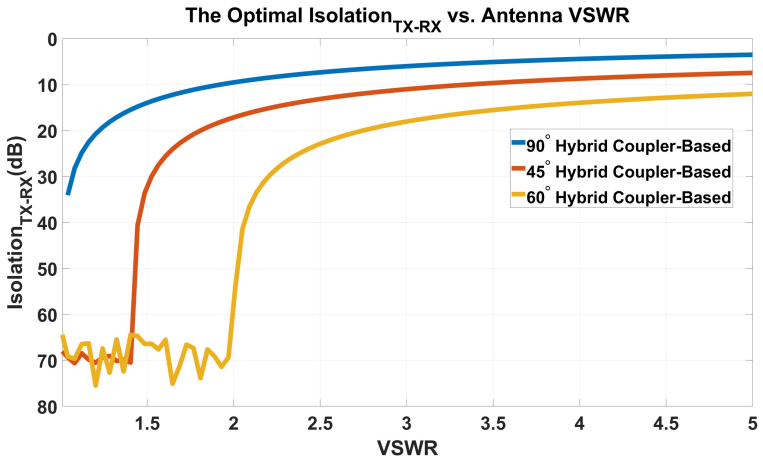

Figure 3.9: The optimal Isolation that the GE-EBD based on different hybrid couplers can achieve as the antenna VSWR changes

3.3. Hybrid-coupler Design

According to the introduction in Section 3.2, three different performances of GE-EBD were achieved by using three types of hybrid couplers with different phases. While the $45°$ and $60°$ hybrid coupler-based GE-EBD provide a larger compensable range, they induce losses of 0.68 dB and 1.25 dB, respectively. In this thesis, the $90°$ hybrid is implemented for the following reasons:

1. In UWB transceiver applications, either on-chip or off-chip antenna impedance matching networks are employed to keep the antenna port impedance close to $50\,\Omega$. Once this duplexer is integrated into the UWB transceiver, this matching network can be used to ensure the VSWR at the antenna end is close to 1.

2. Compared to the compensable range, ensuring the lowest possible insertion loss is critical in this application. Hence, the $90°$ hybrid coupler-based GE-EBD is selected in this thesis, as it offers better performance,

[56] presented a guide for designing a CMOS-compatible, lumped-element equivalent of a coupled-line quadrature hybrid. Compared to other hybrid architectures that use RC-based circuits, this specific circuit demonstrates a lower insertion loss and is less susceptible to component variations. The circuit illustrated in Fig. 3.10 is a lumped-element circuit that has been normalized to a characteristic impedance, represented by Z_0, and an angular frequency of ω_0 at the operating frequency. The values of this circuit are also shown in Fig. 3.10. By using equation (3.44)(3.45), all inductance and capacitance values can be scaled at any desired impedance and frequency. The initial values of the inductance and capacitance are shown in Table 3.2 when the central frequency (f_0) is $7.5\,GHz$ and the characteristic impedance Z_0 is $50\,\Omega$. Due to the parasitic capacitance introduced by the transformer, as well as the parasitic capacitance from other circuits within the duplexer, the capacitance values obtained after optimization simulations are less than the calculated values, as shown in Table 3.2. The $90°$ Hybrid coupler layout is illustrated in Fig. 3.11, featuring tunable capacitors $CG_1 \sim CG_2$ parallel to the ground, while the values of CM_1 and CM_2 remain fixed.

$$L = L_{\text{norm}} \frac{Z_0}{\omega_0} \tag{3.44}$$

$$C = \frac{C_{\text{norm}}}{Z_0 \omega_0} \tag{3.45}$$

Table 3.2: The inductance and capacitance values for the $90°$ hybrid coupler.

Parameter	calculated Value	Design Value
L	1.5 nH	
CG_1	176 fF	50 fF - 170 fF (Tunable)
CG_2	176 fF	45 fF - 130 fF (Tunable)
CM_1	424 fF	293 fF
CM_2	424 fF	120 fF

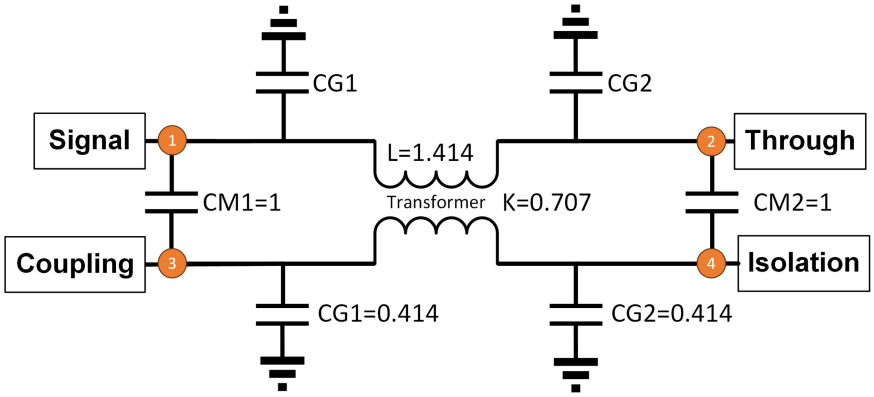

Figure 3.10: Inductively coupled alternative derived from coupled-line directional couplers.

The simulation results of the transformer are shown in Fig. 3.12. The inductance is close to 1.5 nH, and the magnetic coupling factor is about 0.72, which is fairly consistent with the calculated value. The simulation results are displayed in Fig. 3.13, indicating that the insertion loss of the through port and coupling port is the same at approximately 3.5 dB around 8 GHz. The isolation between the signal port and isolation port exceeds 30 dB, while the phase difference between the through port and coupling port is around $90°$, less than $1°$. As can be seen from Fig. 3.8, the additional insertion loss brought by phase unbalance of less than 1 degree is very small and can be neglected. At the desired frequency, there is an amplitude unbalance ranging from -1.2 dB to 1 dB, which could result in a maximum loss of 0.5 dB. When integrating the hybrid coupler with other circuits in the duplexer, parasitic capacitance can cause the center frequency to shift towards lower frequencies. As a result, it is necessary to use tunable capacitors $CG_1 \sim CG_4$ after the entire duplexer design is completed in order to maintain the center frequency within the desired frequency range. For those seeking to design a $45°$ or $60°$ hybrid coupler, a comprehensive design methodology is readily available through [57].

The simulation shown in Fig. 3.13 is a combination of the EM simulation of the transformer and the post-simulation results of the RC extraction of surrounding components. However, if we examine this layout, as shown in Fig. 3.11, we notice that the wires from C_{M1} to C_{G3} and from C_{M2} to C_{G4} exceed a length of $200\,\mu m$. This increases the parasitic capacitance and resistive losses and introduces a significant inductance. Therefore, the parasitic inductance introduced by these wires should also be considered to obtain accurate simulation results. As illustrated in Fig. 3.14, an EM simulation is performed on this part of the circuit, and then the results are integrated into the rest of the circuit for post-simulation. The final simulation results are shown in Fig. 3.15. After considering the EM simulation of the long wires, it can be observed that the phase and amplitude unbalance have deteriorated

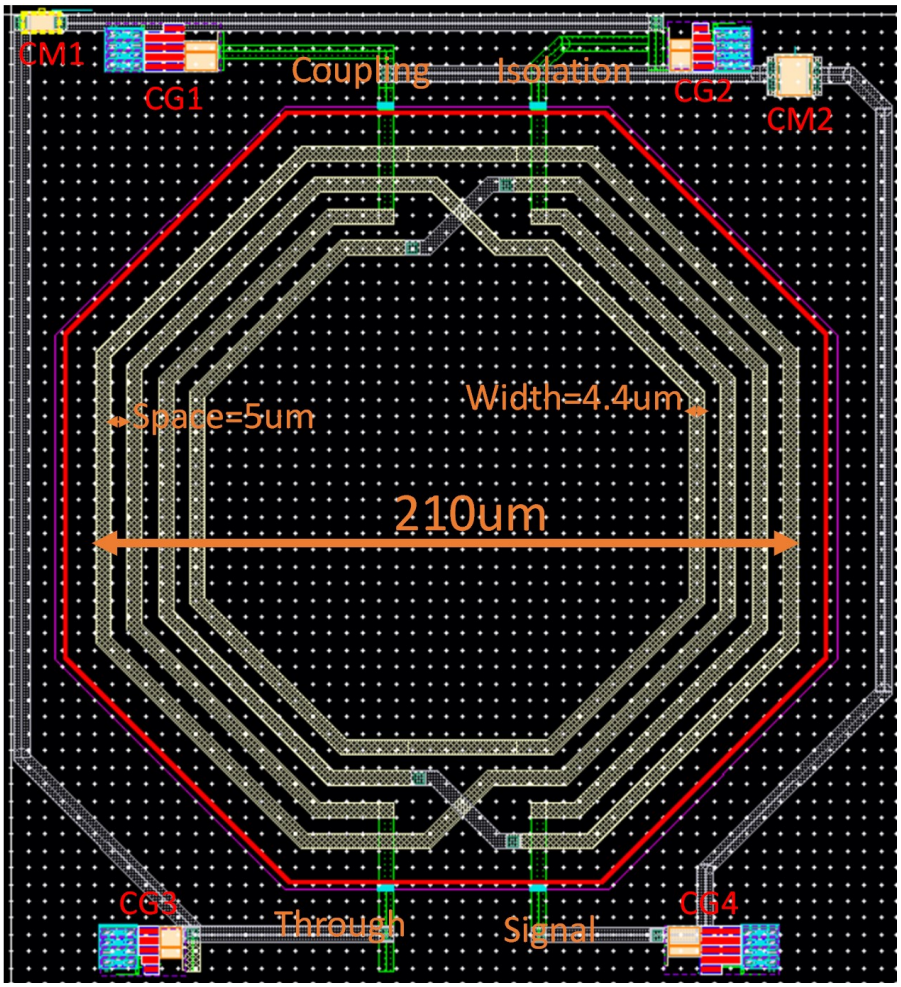

Figure 3.11: The layout of the 90° hybrid coupler.

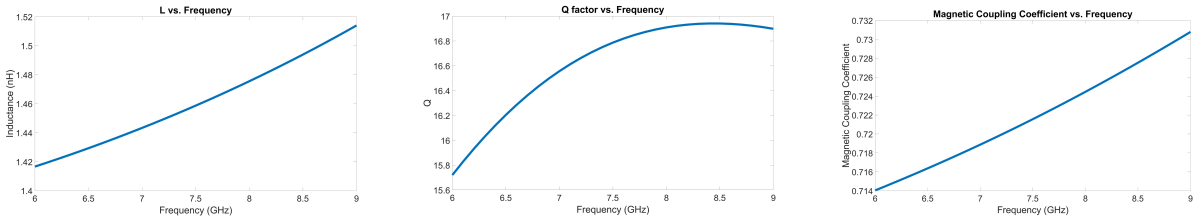

(a) (b) (c)

Figure 3.12: The simulation results of the transformer. (a) Inductance. (b) Q factor. (c) Coupling coefficient.

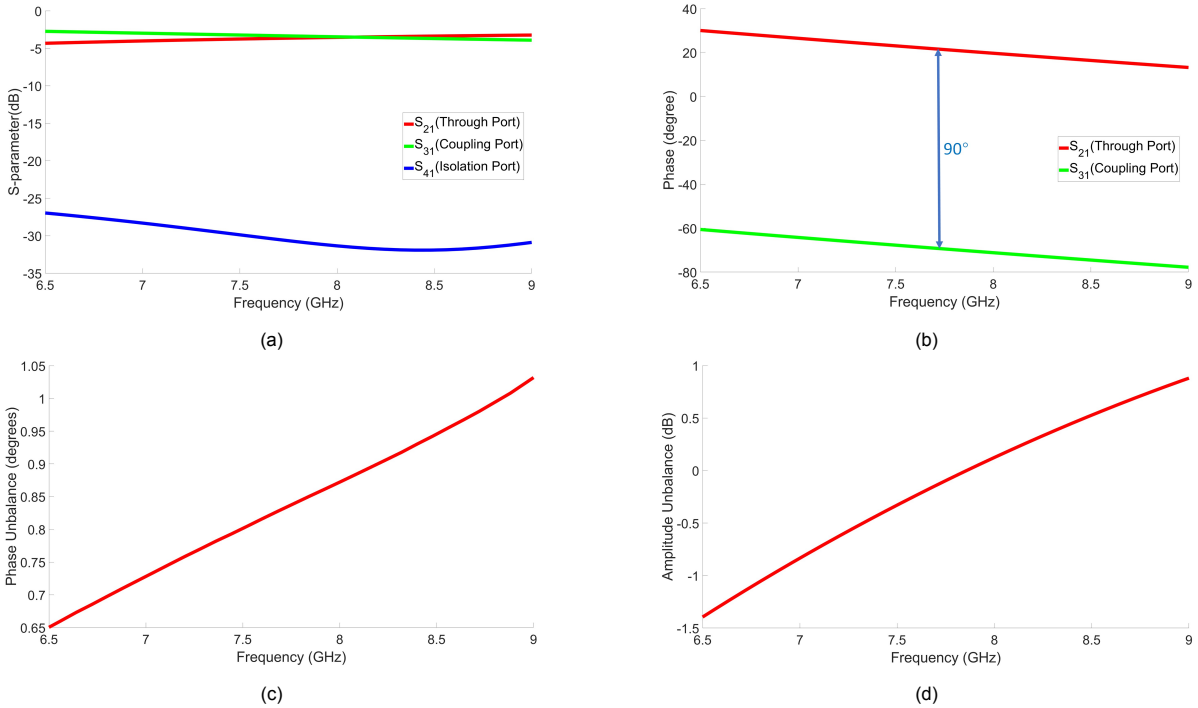

Figure 3.13: Simulated S-parameter characteristics for 90° Hybrid coupler. (a)The amplitude simulation result. (b)The phase simulation result. (c)The phase unbalance simulation result. (d)The amplitude unbalance simulation result.

significantly. The reason has been mentioned before: the RC extraction did not take into account the inductive effects of the transmission lines. The unbalance in phase and amplitude has increased to 15° and 2 dB, respectively, resulting in additional losses of approximately 0.07 dB and 1 dB. However, the layout of the entire duplexer should consider the hybrid coupler and the interconnections between other circuits. Therefore, the performance of the duplexer can be optimized after completing the entire circuit. Moreover, setting multiple tunable capacitors in the duplexer can effectively help improve the unbalance of phase and amplitude.

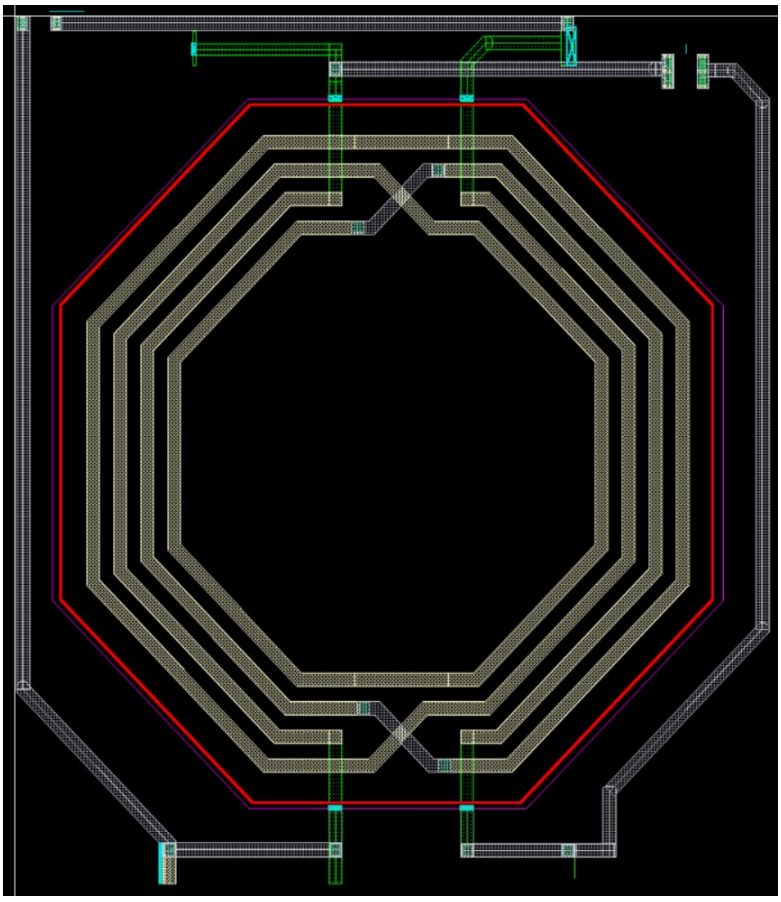

Figure 3.14: The 90° hybrid coupler layout circuit for EM simulation.

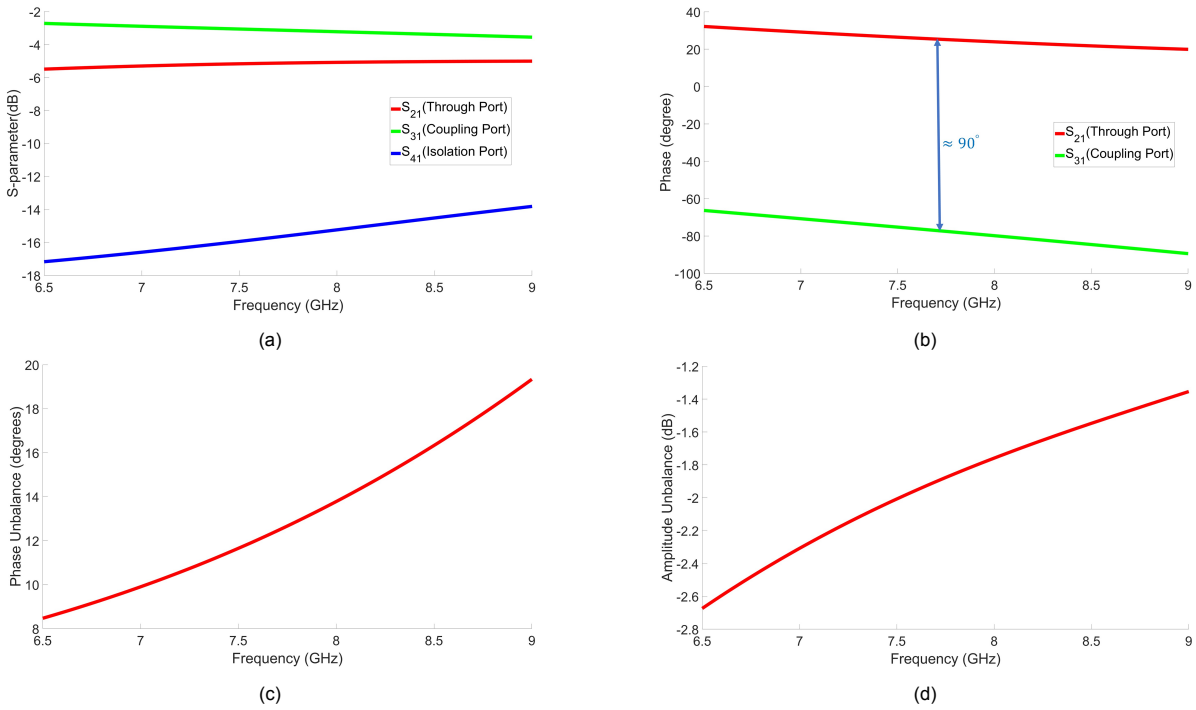

Figure 3.15: Simulated S-parameter characteristics for 90° Hybrid coupler based on the EM simulation in Fig. 3.14. (a)The amplitude simulation result. (b)The phase simulation result. (c)The phase unbalance simulation result. (d)The amplitude unbalance simulation result.

3.4. Gyrator Design

This subsection will introduce how to implement a non-reciprocal phase shifter. As described in Chapter 2, three techniques exist to achieve a non-reciprocal phase shifter. Among them, the N-path filter can implement a non-reciprocal phase shifter of $\pm 90°$, but the power consumption is very high. In this duplexer, a preferred large load capacitance of around 1 pF is needed for broad bandwidth. With a supply voltage of 0.9 V and a frequency of approximately 7.5 GHz, using the equation $Power = CV^2 f$ and an 8-path N-path filter, the estimated power consumption is about 24 mW, without even accounting for the circuit's power consumption generating the eight local oscillation signals. Even with a 4-path filter, the power consumption is at least above 10 mW, which cannot meet the low power consumption requirement of the transceiver. The power consumption can be reduced if a spatiotemporal conductance modulation circuit is used to achieve a $0°/180°$ non-reciprocal phase shifter. In [54], it is noted that at a comparable frequency, power consumption can be as low as 3 mW. However, a fully differential circuit is required to implement this circuit, meaning that two additional baluns must be designed for both the antenna and the RX. This not only increases the chip area but also the insertion loss. Moreover, just implementing a non-reciprocal phase shifter already requires five coils, taking up a large area of the chip. Additionally, generating precise local oscillation signals in this frequency band is a significant challenge and will further increase circuit complexity. To summarize, using a gyrator to implement a non-reciprocal phase shifter is a good choice for this application. It avoids the complexity of clock generation circuits and effectively reduces the chip area. Achieving non-reciprocity can be done by using active devices like transistors. However, this requires the implementation of low-power and low-noise designs.

3.4.1. The Block Diagram of Transformer-based Gyrator

The block diagram of the proposed circuit is shown in Fig. 3.16. The non-reciprocity is achieved by using a combination circuit of Gm cell and two step-up transformers. It should be noted that the tap directions of the output of the two transformers in the figure are inverse, which realizes $0°/180°$ phase shifting in the forward and reverse directions. If a signal with positive voltage is transmitted from port 1 to port 2, it induces a positive voltage at the secondary coil of T1. This voltage then goes through Gm_1, resulting in a negative current. Once the negative current passes through T2, a positive voltage is produced at Port 2 since the primary and secondary stages of T2 are connected in reverse. Therefore, the phase shifting from port 1 to port 2 is $0°$. Likewise, It can also be concluded that there is a phase shift of $180°$ from port 2 to port 1.

3.4.2. Circuit Analysis

This section will analyze the gain, S-parameters, and other important parameters of the circuit using open-loop and closed-loop circuit methods. The impedance at the input and output ports needs to satisfy $50\,\Omega$ impedance matching. First, the proposed gyrator is analyzed by assuming ideal components for easy computation. The g_m cell and transformer are assumed to be ideal components. This means no current enters or exits the g_m cell's input end, and there is no loss when the current traverses the transformer. As a result, the input impedance R_{in}, as shown in Fig. 3.17 (a), can be calculated using the following formula:

$$R_{in} = \frac{N^2}{16 g_m^2 R_L} \tag{3.46}$$

In this context, R_{in} represents the input impedance, and R_L is the load impedance at port 2, which is $50\,\Omega$. By substituting these values into equation (3.46), it can derived the relation between g_m and N:

$$g_m = \frac{N}{200} \tag{3.47}$$

Next, the noise voltage and noise figure are analyzed. In Fig. 3.16, the noise current output from Gm_1 will dominate the noise at port 2, because the equivalent noise current output from Gm_2 will not flow into Gm_1, nor will it affect port 2. Therefore, the equivalent noise voltage at the output is:

$$\overline{V_{n,\,\text{out}}} = 2R_S \frac{\sqrt{4kT\gamma g_m}}{N} \tag{3.48}$$

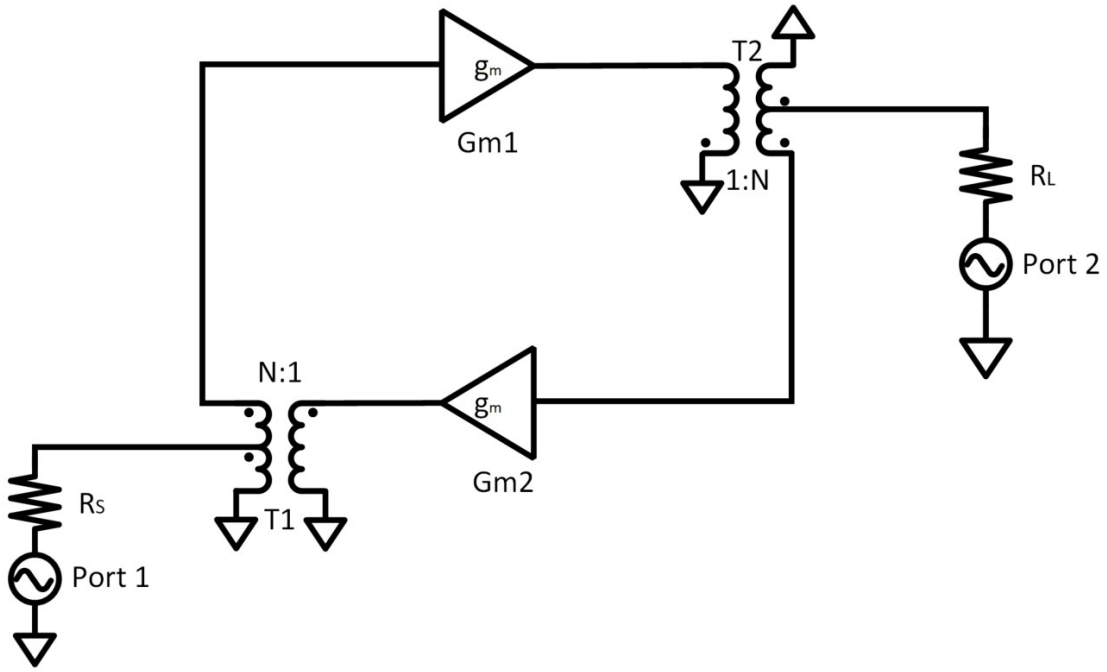

Figure 3.16: The block diagram of the proposed gyrator.

Substituting equation (3.47) into equation (3.48), the equivalent noise at the output $\overline{V_{n,\,\text{out}}}$ can be expressed as equation (3.49). In this equation, k is the Boltzmann constant, T represents temperature, and the coefficient γ is a constant typically assumed as 2/3. It can also be set to one for ease of computation. R_s represents the load impedance of $50\,\Omega$.

$$\overline{V_{n,\,\text{out}}} = 2R_S\sqrt{\frac{kT\gamma}{50 \cdot N}} \tag{3.49}$$

Based on the definition of the noise figure:

$$\text{NF} = \frac{SNR_{\text{in}}}{SNR_{\text{out}}} \tag{3.50}$$

According to the calculation in [58], the calculation of NF in this gyrator can be simplified to:

$$\text{NF} = \frac{1}{4kTR_S} \cdot \frac{\overline{V_{n,\,\text{out,total}}^2}}{A_0^2} \tag{3.51}$$

The total noise $\overline{V_{n,\,\text{out,total}}^2}$ at the output is composed of the noise generated by the gyrator and the source R_S. substituting equation (3.49) into equation (3.51), the NF in this gyrator is:

$$\text{NF} = \left(1 + \frac{1}{A_0^2}\frac{4\gamma g_m}{N^2}R_S\right) \tag{3.52}$$

The voltage gain A_0 from port 1 to port 2 is 1. Substituting into the equation, the noise figure (NF) of the gyrator is:

$$\text{NF} = 1 + \frac{\gamma}{\text{N}} \tag{3.53}$$

The gain calculation is a bit more complex because this circuit has a voltage-to-current feedback loop. To make this issue easier, start by computing the voltage gain from V_{in} to V_2^-. For the input and output to match, their respective impedance should follow the following equations:

$$\begin{aligned} R_S &= R_{in} = 50\,\Omega \\ R_L &= 50\,\Omega \end{aligned} \tag{3.54}$$

The reflected wave of the gyrator is:

$$\begin{aligned} V_1^- &= 0 \\ V_2^+ &= 0 \end{aligned} \tag{3.55}$$

To begin, the open-loop gain must be calculated. In Fig. 3.17(b), the open-loop gain A_{OL} can be easily obtained:

$$A_{OL} = \frac{4g_m R_s}{N} \tag{3.56}$$

To determine the feedback factor β, we need to take the following steps: First, we break the loop. Next, we set a test signal V_t and follow it around the loop. Finally, we measure the value V_F that returns to the breakpoint, as shown in Fig. 3.17 (c). The β can be obtained by using equation (3.57).

$$\frac{V_F}{V_t} = -\beta A_{OL} \tag{3.57}$$

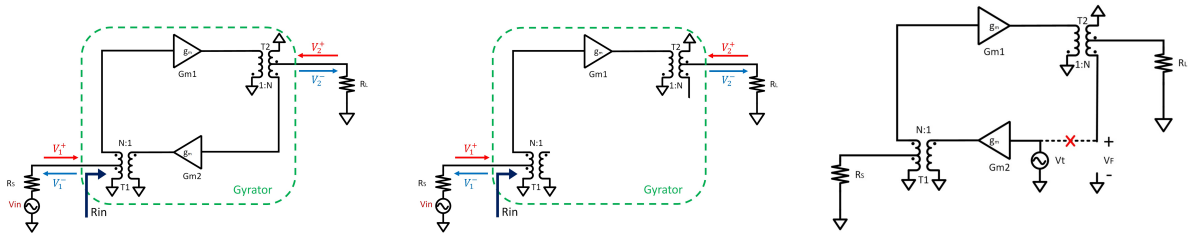

Figure 3.17: The computation of gyrator gain. (a) The S-parameter calculation with incident and reflected waves. (b) The open loop gain computation. (c)The feedback factor β computation.

Next, calculate the feedback factor β. The result of the feedback factor beta is:

$$\beta = \frac{16 g_m^2 R_s^2}{N^2} \tag{3.58}$$

Then, the closed loop gain is:

$$A_{CL} = \frac{A_{OL}}{1 + \beta A_{OL}} \tag{3.59}$$

Substituting equation (3.47),(3.56),(3.58) and $R_s = 50\,\Omega$ into (3.59), the close-loop gain can be obtained:

$$A_{CL} = \frac{V_2^-}{V_{in}} = \frac{1}{2} \tag{3.60}$$

The voltage gain (A_{CL}) is calculated from V_{in} to V_2^-, but we require the gain between V_1^+ and V_2^-:

$$S_{21} = \left.\frac{V_2^-}{V_1^+}\right|_{V_2^+ = 0} \tag{3.61}$$

If the input matching condition is assumed, i.e., $R_S = R_{in} = 50\,\Omega$, then the relation between input voltage V_{in} and the incident wave V_1^+ is as following:

$$V_1^+ = \frac{R_{in}}{R_{in} + R_S} V_{in} = \frac{1}{2} V_{in} \tag{3.62}$$

We can get the S-parameter S_{21} for this circuit with the matching condition by substituting equation (3.60) (3.62) into (3.61). The value of $|S_{21}|$ is 1. Similarly, we can obtain $|S_{12}|$ which is also 1. The forward and backward phase shifting can be obtained by observing the direction of T1 and T2.

$$\begin{aligned} |S_{21}| = |S_{12}| = 1 = 0\,dB \\ \angle S_{21} = 0° \\ \angle S_{12} = 180° \end{aligned} \tag{3.63}$$

This conclusion can be verified with ideal components by using ADS, as shown in Fig. 3.18. The simulation results are shown in Fig. 3.19. Under matched conditions, the reflection loss is infinitesimally small; the gain is 0 dB, and importantly, non-reciprocal phase shifting is achieved, with forward phase shifting being $180°$ and reverse phase shifting being $0°$.

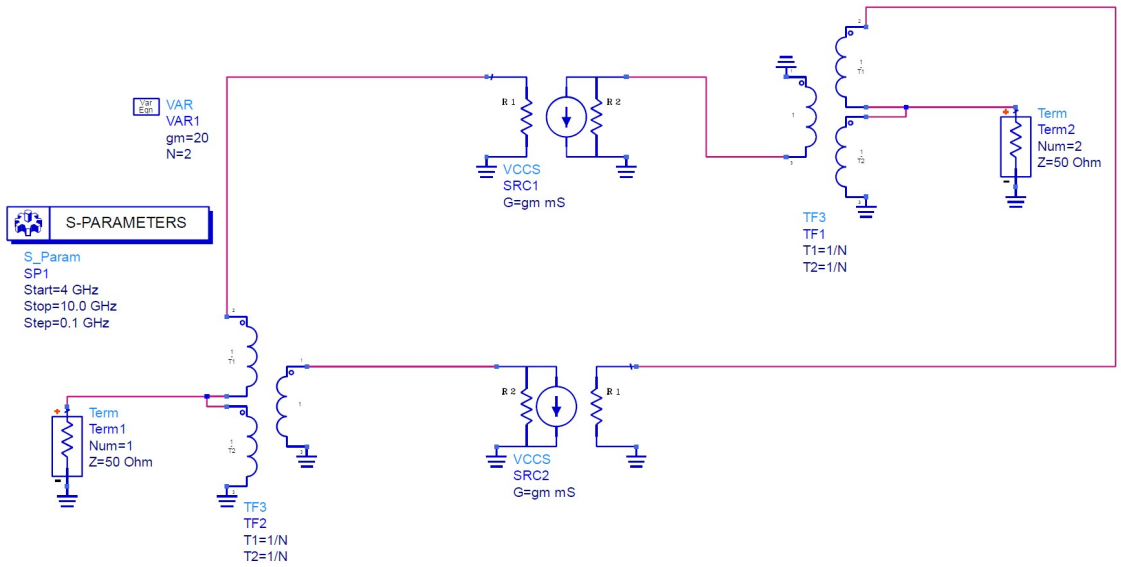

Figure 3.18: The simulation model of the proposed gyrator in ADS.

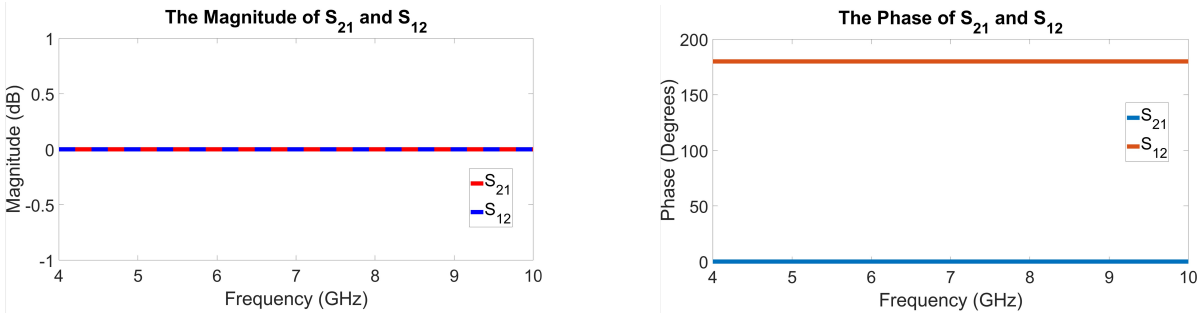

(a) (b)

Figure 3.19: The ADS simulation results of the proposed gyrator. (a) The Magnitude simulation results. (b) The phase simulation results.

[35] has implemented a low-power, broadband gyrator working near 66 GHz by using a co-directional and a reverse 1:1 transformer. By adjusting g_m (transconductance), the input and output impedance can be set to $50\,\Omega$. Moreover, g_m is also related to the ratio of the transformer:

$$g_m = \frac{N}{50} \tag{3.64}$$

After comparing equation (3.47) with equation (3.64), it is clear that the upgraded circuit has significantly reduced the current demand to one-fourth of its initial requirement. This has resulted in a

remarkable decrease in power consumption, which is now only one-sixteenth of its original value. The noise level calculation result at the output end matches the one presented in reference [35]. Interestingly, the NF of the new gyrator has improved as the required g_m has decreased.

3.4.3. Design and Simulation

Fig. 3.20 shows the designed schematic for the gyrator, which requires a 5-bit adjustable current source due to its sensitivity to input and output impedance. The center operating frequency of the gyrator can be adjusted using capacitor CP, which is in parallel with the first stage coil of the step-up transformer. Capacitor CT is used to resonate with the leaked inductance caused by the non-ideal transformer, while capacitor CS is primarily used for AC coupling and matching. The Gm cell uses the simplest common source stage circuit, and the operation points for M1 and M2 are chosen based on a trade-off between noise and large signal performance. The values for capacitors, transistors, and the current source range are listed in Table 3.3.

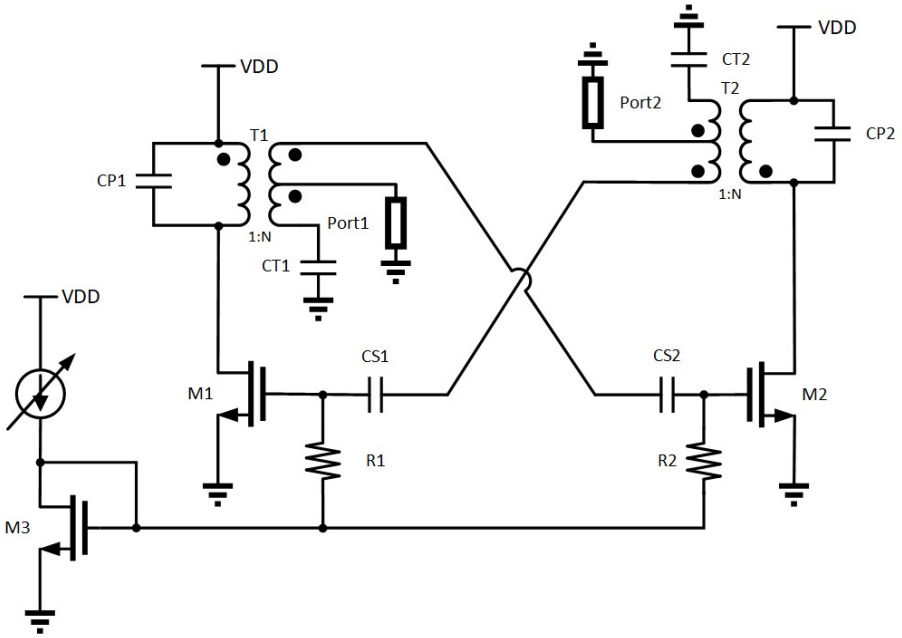

Figure 3.20: The schematic of the proposed gyrator.

Table 3.3: The design values for the proposed gyrator

Parameters	Design value
CP_1	$101\,fF$
CP_2	$101\,fF$
CT_1	$2.63\,pF$
CT_2	$2.63\,pF$
CS_1	$802\,fF$
CS_2	$802\,fF$
R_1	$128\,k\Omega$
R_2	$128\,k\Omega$
M_1	$7.2\,\mu m/30\,nm$
M_2	$28\,\mu m/30\,nm$
M_3	$28\,\mu m/30\,nm$
Current Source (5-bit tunable)	$0 \sim 0.57\,mA$

The step-up transformers T1 and T2 are this circuit's most important passive components. As equation (3.49) shows, the larger the turn ratio N, the less noise the gyrator injects into the circuit. However, according to equation (3.64), the larger the N, the more current is required to maintain impedance matching. Therefore, N must strike a balance between noise and power consumption. In addition, a larger turn ratio N means a smaller coupling factor [59], and an overly large secondary coil also implies a larger area and more parasites, all of which can degrade the performance of this duplexer. Considering

all these factors, the step-up transformer designed in this thesis has a turn ratio of 4. The layout of the step-up transformer and the gyrator is shown in Fig. 3.21, Fig. 3.23, respectively. The space between conductors must be minimized to improve the magnetic coupling coefficient. Therefore, the minimum value allowed by the process for the space between metal wires is set at $2\,\mu m$. When selecting the width of the conductor for a transformer, it's crucial to consider its impact on self-frequency, coupling coefficient, and Q-factor altogether. If the conductor's width is too broad, it will reduce the self-frequency of the transformer. This is due to a broader conductor's increased inductance and larger parasitic capacitance. Furthermore, as the conductor's width grows, the coupling coefficient decreases [59]. Therefore, the choice of conductor width should primarily meet the requirements for self-frequency and coupling coefficient. The width should be moderately increased, ensuring the self-frequency and coupling coefficient requirements are met. This is because too narrow a width will increase the resistance of the transformer, leading to a reduced Q-factor. A $4\,\mu m$ width is typically chosen for optimal performance. A dimension of $200\,\mu m$ has been chosen to achieve a high Q-factor at the desired frequency.

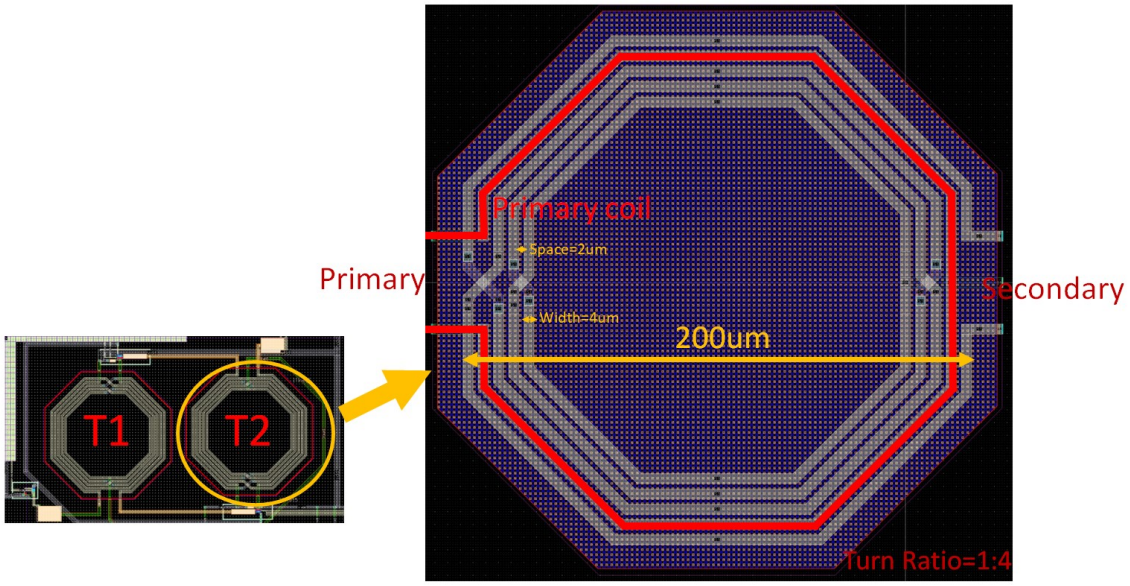

Figure 3.21: The layout of the step-up transformer.

As shown in Fig. 3.22, its simulation results indicate that the primary coil operates in the region with the maximum Q value, the coupling factor is also around 0.8, and the effective turn ratio is close to 4.

The circuit's large area, resulting from using two transformers and operating at a high frequency with the gyrator, undoubtedly makes wiring more challenging. Wire lengths that are too long can cause parasitic effects, losses, and reduced noise performance. Furthermore, the gyrator's layout design also has to consider the overall layout of the transceiver. The completed layout is shown in Fig. 3.23. Its post-simulation is shown in Fig. 3.24. S_{11} and S_{22} are less than -15 dB at the frequencies of interest, which proves that port 1 and port 2 are well matched. The in-band insertion loss is between 1 dB and 2 dB, and the noise figure is approximately 3.2 dB. It is worth noting that the forward phase shift is about $-45°$, while the reverse phase shift is $-225°$, not $0°/180°$. This is because the transformer in the gyrator is not ideal, and the LC circuit composed of the transformer's inductance and the capacitance in the circuit causes a phase deviation. Therefore, a fixed $45°$ phase shifter, as shown in Fig. 3.27, is added to the circuit to compensate for the phase deviation.

At the desired frequency, there is a phase unbalance ranging from $-2°$ to $-3°$, and a magnitude unbalance ranging from 0.7 dB to 1.5 dB, as shown in Fig. 3.24(e) and (f). As analyzed in section 3.2.2, the phase and amplitude unbalance of the gyrator would improve the isolation of TX and RX, but at the cost of increasing the losses of TX and RX. As shown in Fig. 3.6, the loss caused by a phase deviation of less than $3°$ is negligible. Due to the unidirectional pass-through characteristic of the gyrator, the forward loss S_{21} will have a greater impact on RX, and S_{12} will have a greater impact on TX, and the imbalance between them will not bring additional adverse effects. As can be seen from Fig. 3.24(b),

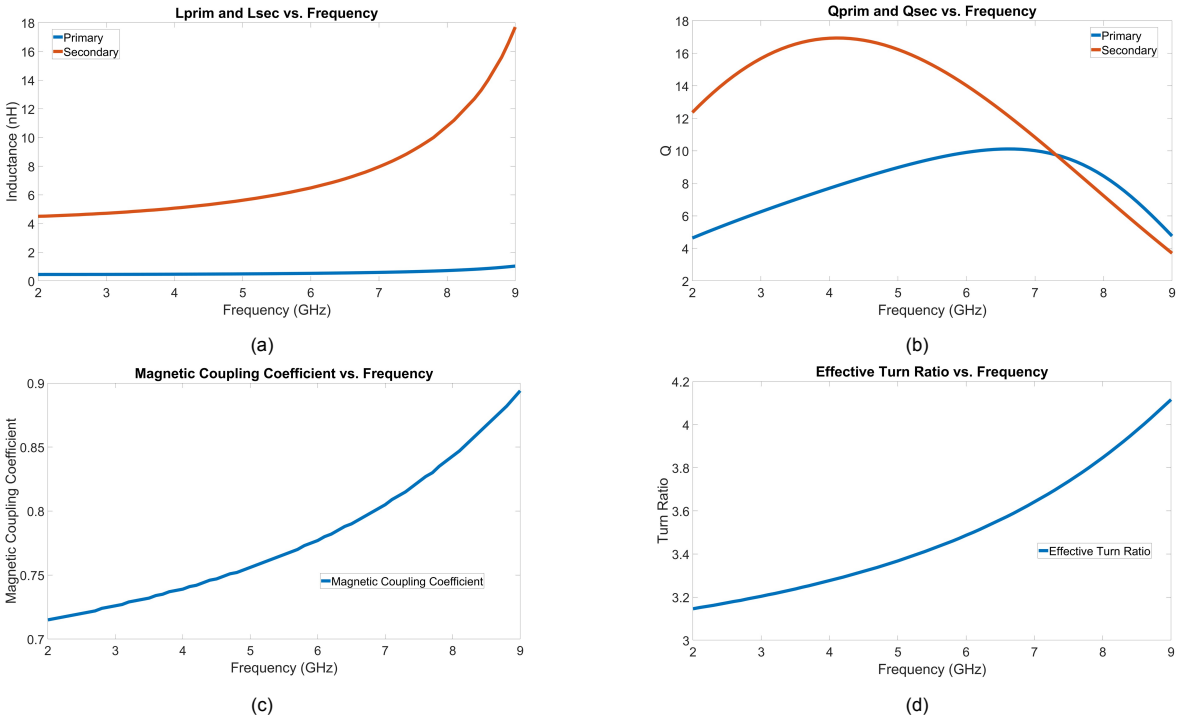

Figure 3.22: The simulation result of the step-up transformer. (a) The inductance of the primary and secondary coil. (b) The Q factor of the primary and secondary coil. (c) The magnetic coupling coefficient. (d) The effective turn ratio.

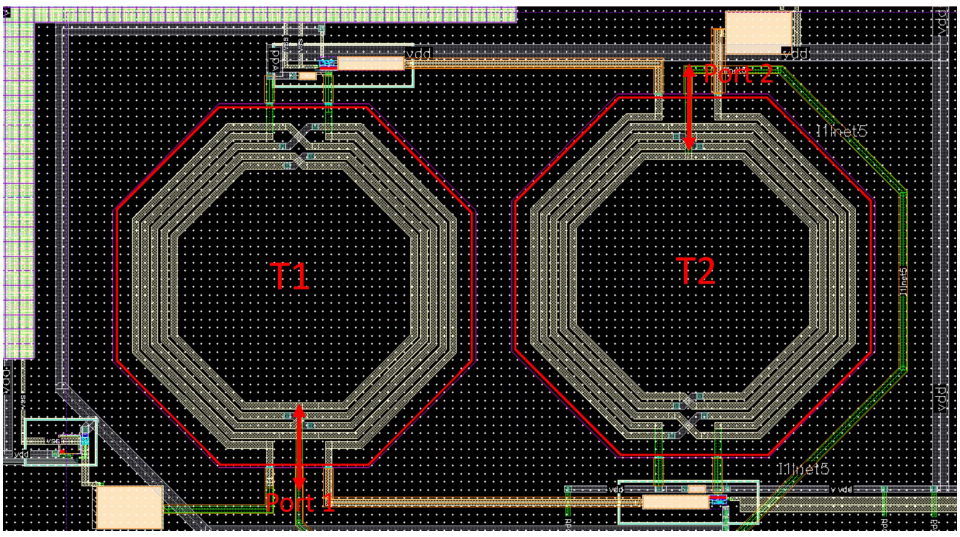

Figure 3.23: The layout of the proposed gyrator.

the loss of S_{21} is better than the loss of S_{12}, so in the duplexer circuit, $RXIL$ will be better than $TXIL$. A 1dB loss in the gyrator will lead to a 0.5 dB loss in the duplexer, while a 3 dB loss will result in a 1.4 dB loss, as shown in Fig. 3.7 (b).

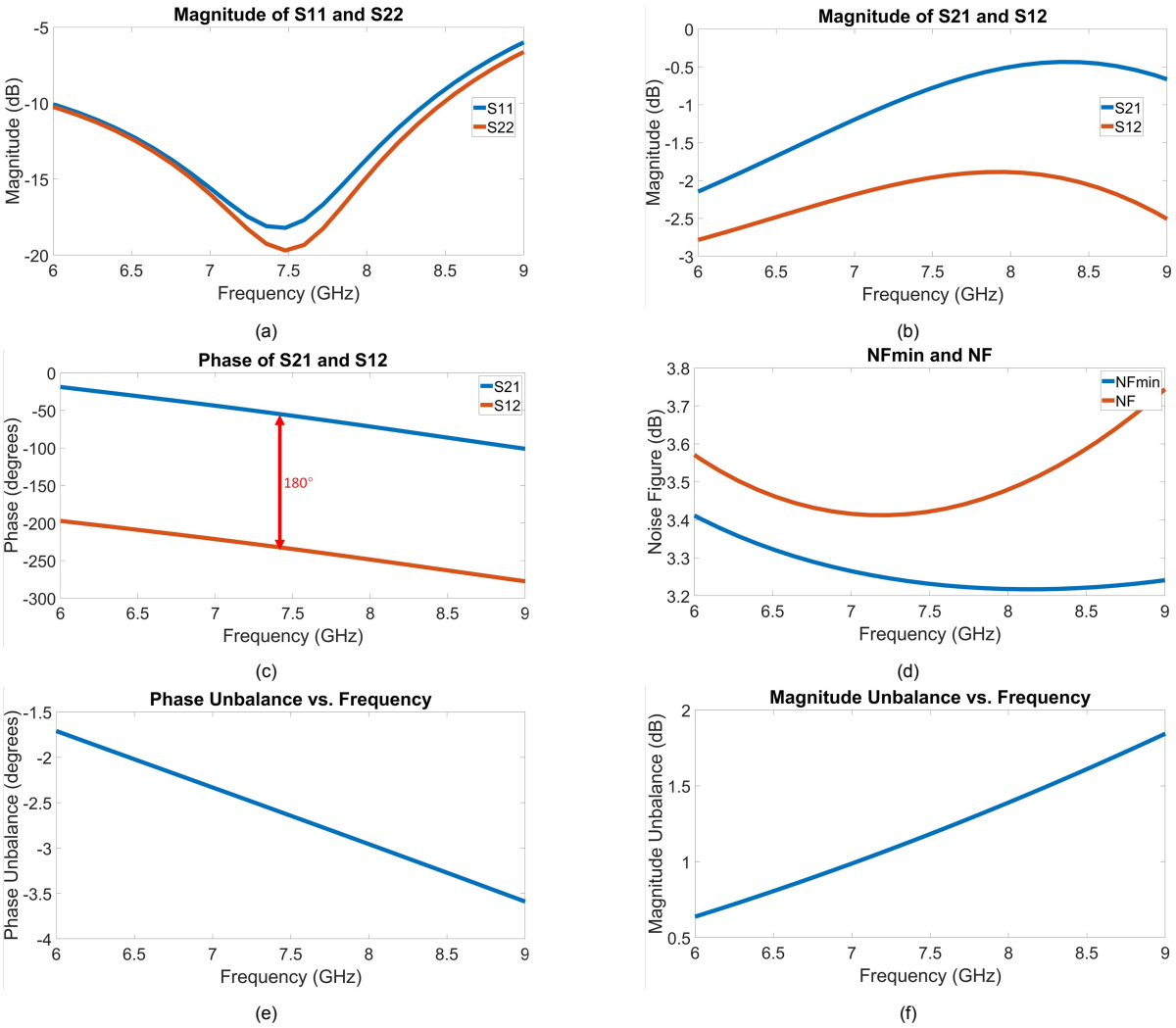

Figure 3.24: The post-simulation result of the proposed gyrator. (a) The magnitude of S_{11} and S_{22}. (b) The magnitude of S_{21} and S_{12}. (c) The phase of S_{21} and S_{12}. (d) The noise figure & The minimal noise figure. (e) The phase unbalance between S_{21} and S_{12}. (f) The magnitude unbalance between S_{21} and S_{12}.

During layout, asymmetrical routing can lead to inconsistencies in the magnitude of the forward and reverse directions. However, this would not lead to such a large magnitude imbalance of 0.5dB to 2dB, as shown in Fig. 3.24(f). The real reason is the difference in magnitude responses due to different connections of the primary and secondary coils of the transformer. For the same planar transformer (or Frlan transformer), a transformer with an inverting connection will have a superior frequency response in the designed working frequency compared to a transformer with a non-inverting connection. This variation is mainly caused by interwinding capacitance, which results in a zero in the response of the non-inverting transformer [59]. As shown in Fig. 3.25, the two transformers in the gyrator are connected differently. For transformer T_1, since a phase shift of $0°$ is needed, the primary and secondary of the transformer are connected in a non-inverting way. As for T_2, a $180°$ phase shift is needed, so it is connected in an inverting way. For these two different connections, a testbench is set up according to Fig. 3.25 to simulate the frequency response of these two connections separately and then calculate their amplitude difference. The obtained amplitude difference curve is compared with the magnitude unbalance in Fig. 3.24(f). First, inverting and non-inverting transformers' magnitude response (or transmission coefficient) are simulated. The results are shown in Fig. 3.26(a). As previously noted, the

inverting-connection transformer exhibits superior performance. As shown in Fig. 3.26(b), the red curve displays the magnitude of unbalance in the gyrator's forward and backward directions, while the blue curve shows the gap between the inverting and non-inverting connections of the step-up transformer. The two curves match perfectly, proving the accuracy of the analysis.

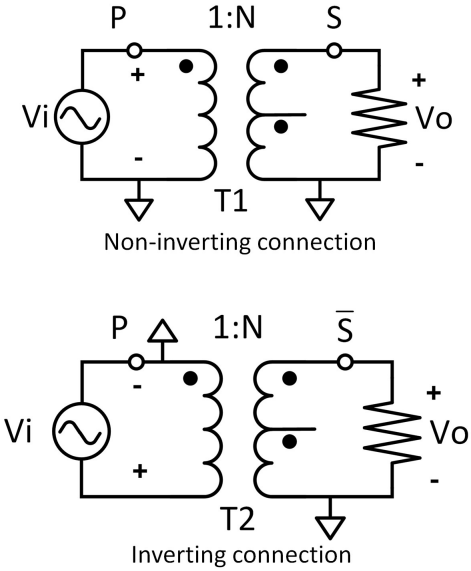

Figure 3.25: Two different connections of the transformer.

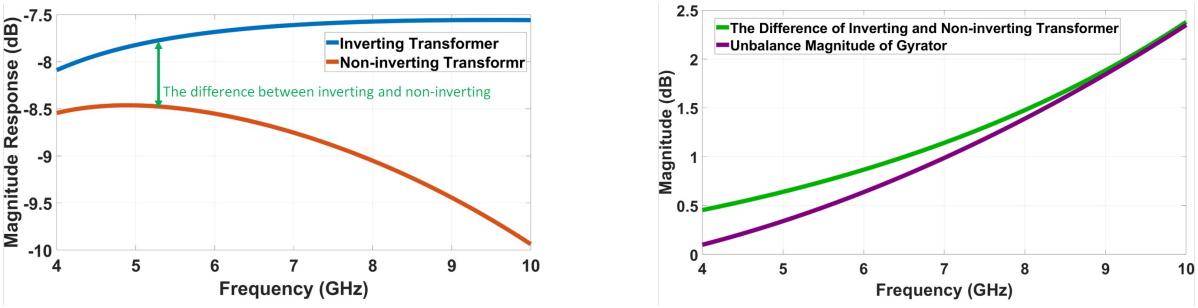

(a) (b)

Figure 3.26: The magnitude response and comparison of unbalance. (a) The magnitude response of inverting and non-inverting transformers. (b) The comparison between the unbalance of the gyrator and the difference of inverting/non-inverting transformers.

3.5. Fixed Phase Shifter Design

An additional adjustment is required to achieve the desired $0°/180°$ phase shift, as the gyrator only provides a $-45°/-225°$ phase shift. The schematic and layout of the fixed phase shifter can be seen in Fig. 3.27, with the capacitor and inductor values provided in Table 3.4. Simulation results are displayed in Figure 3.28. The fixed phase shifting increases the insertion loss of GE-EBD, similar to the impact of the gyrator. In fact, a 1-dB loss will increase by about 0.5 dB loss at RX and TX, respectively. The phase shift is not exactly $45°$ due to the parasitic capacitance changing the phase shift in the duplexer circuit. The intended phase shift is determined through the optimization of GE-EBD's performance.

3.6. Hybrid Transformer Design

[59] provides a detailed explanation of the design principles of transformers based on CMOS technology and outlines a procedure for estimating the size of a monolithic transformer to meet a specific

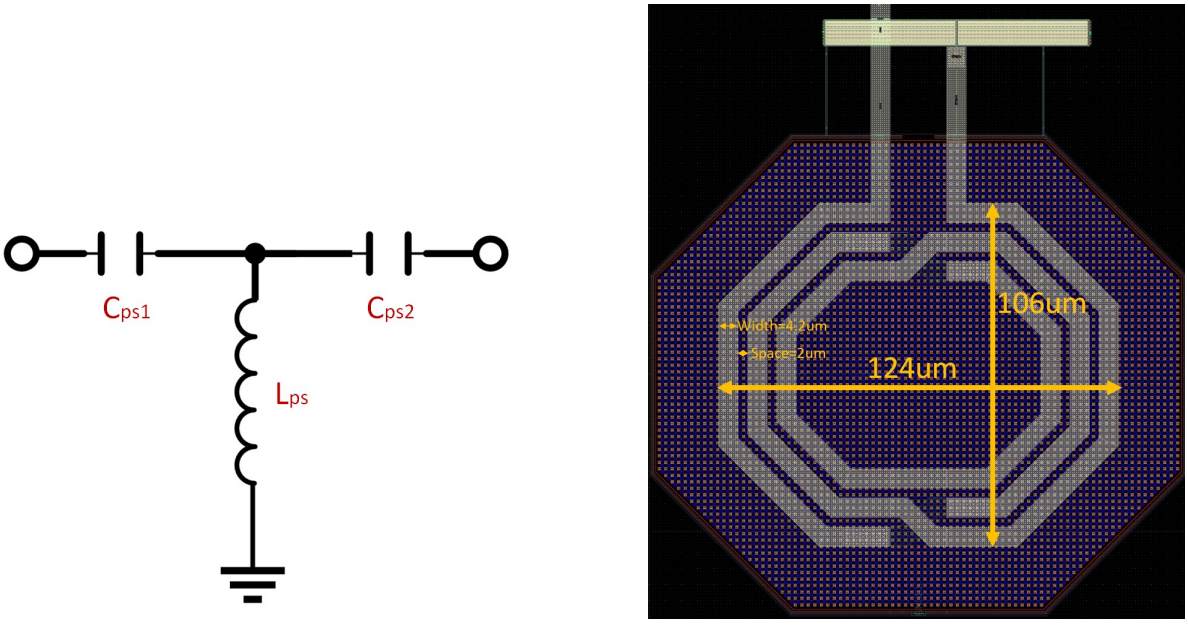

(a) (b)

Figure 3.27: The design of the fixed phase shifter. (a) The schematic design (b) The layout design.

Table 3.4: Design values for the fixed phase shifter

Parameters	Design value
C_{ps1}	$761\,fF$
C_{ps1}	$761\,fF$
L_{ps}	$950\,pH$

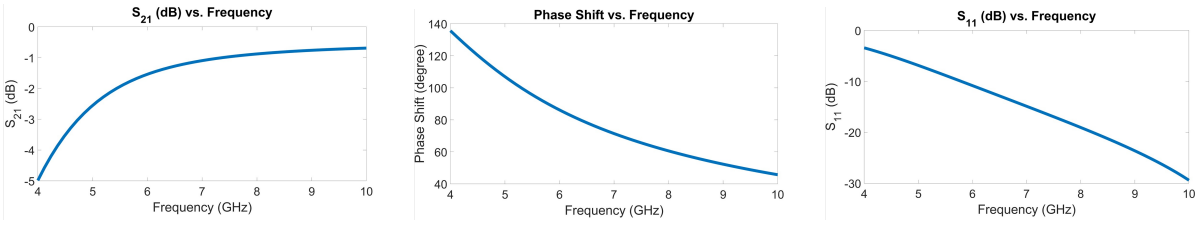

(a) (b) (c)

Figure 3.28: The simulation results of the fixed phase shifting. (a) S_{21} (Insertion Loss). (b) Phase shift. (c) S_{11} (Return Loss).

specification. In [41, 42], the hybrid transformer circuit used in EBD circuits is analyzed in detail. Its simplified model is shown in Fig. 2.4. To achieve circuit matching, bi-conjugacy must be satisfied between TX and RX and between ANT and BAL as expressed in equation (2.1). In this project, $r = 1$, the ratio $\frac{N2}{N1} \approx 1$. Therefore, to ensure matching and bi-conjugacy, the impedance requirements should be as follows:

$$\begin{aligned} R_D &= R_B = 50\Omega \\ R_A &= 25\Omega \\ R_C &= 100\Omega \end{aligned} \tag{3.65}$$

Since the PA and LNA impedances are not always $100\,\Omega$ and $25\,\Omega$, respectively, it is necessary to add a matching network between them and the hybrid transformer. The hybrid transformer can be modeled as a lumped circuit, as shown in Fig. 3.29. Those components' values are shown in Table 3.5. In the analysis in [60], equation (3.66) was obtained. This equation yields the optimum value of $L_{opt,prim}$, resulting in the minimum sum of TXIL and RXIL. The magnetic coupling coefficient, k, is approximately 0.75, while the antenna resistance, R, is approximately 50Ω. Both Q1 and Q2 have a value of around 15. By substituting these values into equation (3.66), the calculated value of $L_{opt,prim}$ is 1.9 nH. Simulating the total parameters in Fig. 3.29 can establish a relationship between L_{prim} and total insertion loss, leading to a similar conclusion as depicted in Fig. 3.30. In this way, the value of L_{prim} is obtained. Based on the empirical formula provided in [61], the planar transformer's outer and inner conductor lengths (OD and ID) can be estimated. Finally, the layout of the hybrid transformer is obtained, as shown in Fig. 3.31. The space between conductors is minimized to obtain the optimal magnetic coupling coefficient. For optimal efficiency, the transformer should be operated in the area with the highest Q value to reduce loss. The simulation results, as shown in Fig. 3.32, indicate that in the operating frequency range, the Q factor is greater than 14, and the coupling coefficient is greater than 0.85. The inductance value is around 2 nH, and the effective turn ratio is close to 1.

$$L_{opt,prim} \approx 2\frac{R}{\omega_0}\sqrt{\frac{Q_1}{2.2k^2Q_2}} \tag{3.66}$$

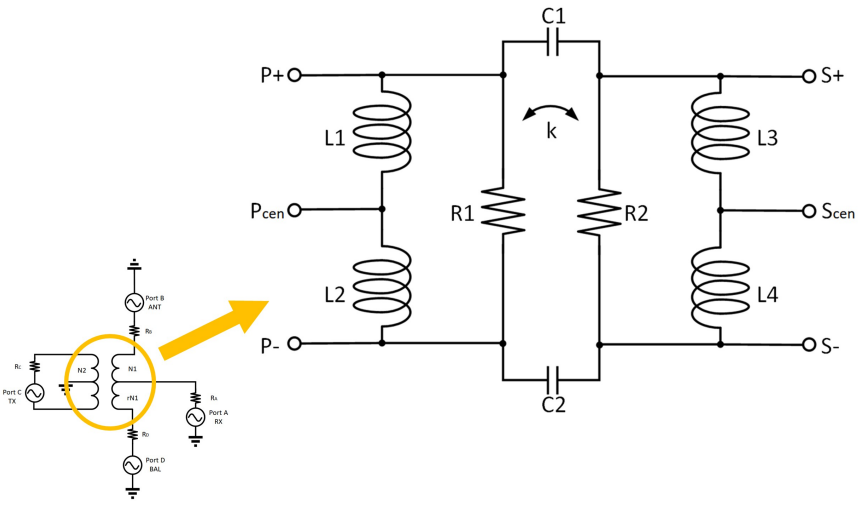

Figure 3.29: The lumped circuit model of the hybrid transformer.

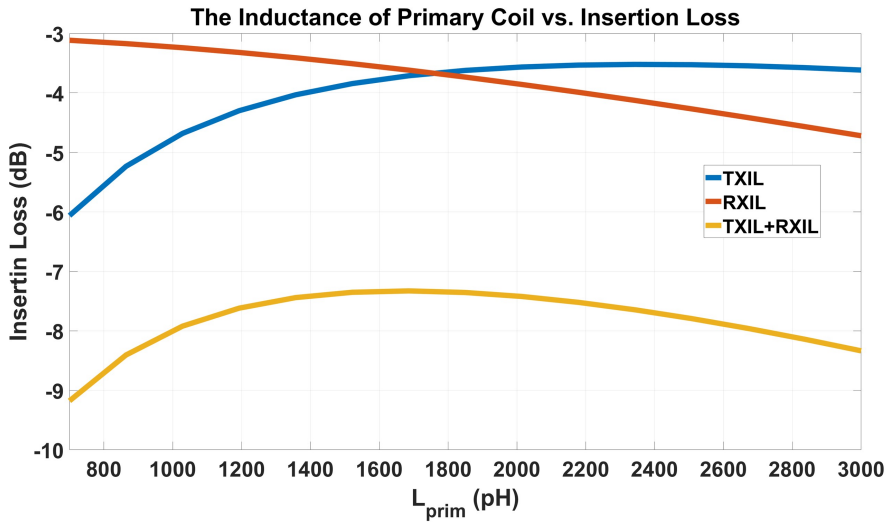

Figure 3.30: The relation between the insertion loss of the lumped model hybrid transformer and the primary inductance.

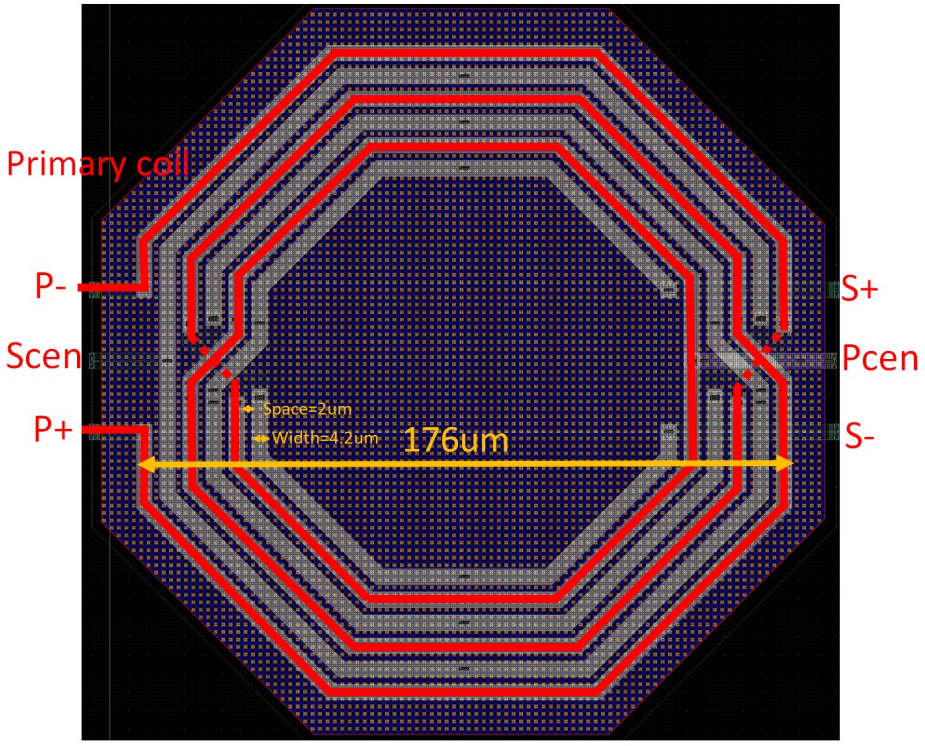

Figure 3.31: The layout of the hybrid transformer.

Table 3.5: The values of the lumped parameters

Parameters	Values	Descriptions
L_1	$L_{prim}/2$	L_{prim}: The inductance of the secondary coil
L_2	$L_{prim}/2$	
L_3	$L_{sec}/2$	L_{sec}: The inductance of the secondary coil
L_4	$L_{sec}/2$	For simplicity, assume that $L_{prim}/2$ is approximately equal to L_{sec}.
C_1	$C_w \cdot k$	C_w: The parasitic capacitance between primary and secondary coils
C_2	$C_w \cdot k$	C_w is around 10 fF
R_1	$Q \cdot 2 \cdot \pi \cdot f_{res} \cdot L_{prim}$	f_{res}: The self-resonant frequency ($> 10\,GHz$)
R_2	$Q \cdot 2 \cdot \pi \cdot f_{res} \cdot L_{sec}$	
k	≈ 0.75	k: Magnetic coupling coefficient

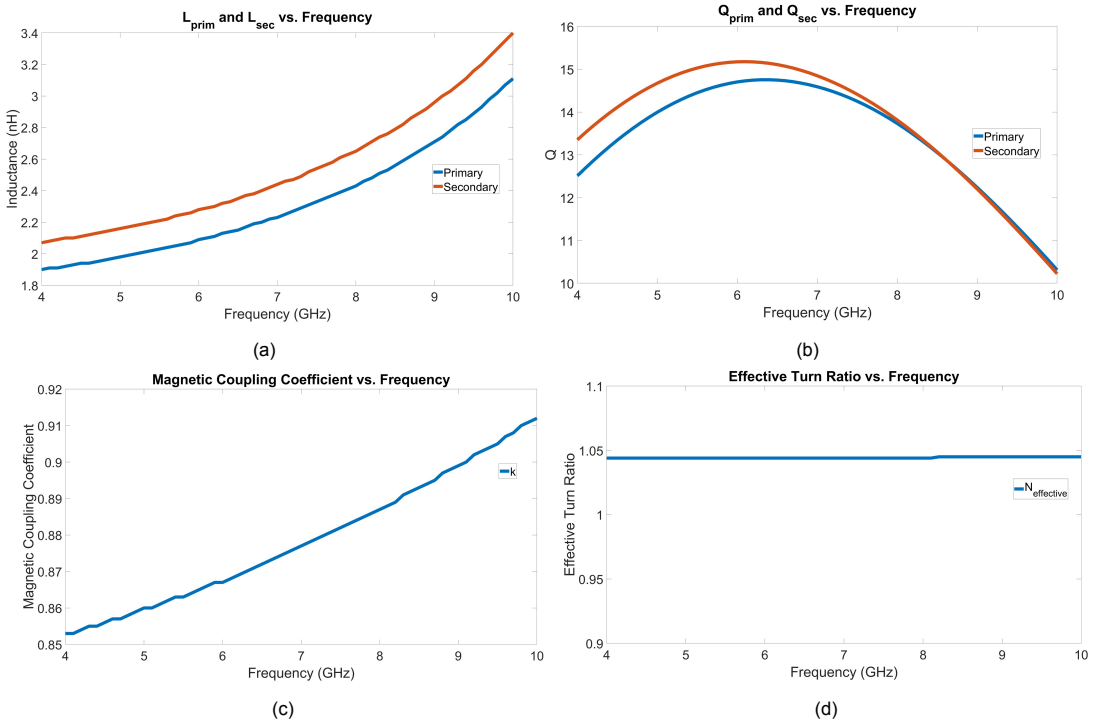

Figure 3.32: The simulation results of the hybrid transformer. (a) Inductance. (b) Q factor. (c) Magnetic coupling coefficient. (d) Effective Turn Ratio.

3.7. GE-EBD Layout and Simulation

Ultimately, the schematic of the GE-EBD is obtained, as shown in Fig. 3.33. GE-EBD includes a hybrid transformer, a hybrid coupler, a fixed phase shifter, a 2-bit balance network, and a gyrator, as shown in Fig. 3.33. The matching network on the figure's left adjusts the antenna's impedance. It can be challenging to achieve a $50\,\Omega$ impedance at the antenna due to the parasitic inductance and capacitance caused by the bond wire and pad. Adding an adjustable matching network between the antenna and the duplexer allows the impedance seen from the duplexer output to be $50\,\Omega$. The balance network can operate in three different states: $50\,\Omega$, $200\,\Omega$, or an open circuit. The gyrator relies on a 5-bit adjustable current source to power the active portion of the circuit. As mentioned earlier, the parasitic capacitance of the transformer in the gyrator will affect the phase of S_{21} and S_{12}. In order to fix any phase deviation, a CLC circuit is placed between the hybrid coupler and hybrid transformer circuit as a fixed phase shifter. The duplexer's capacitors connected in parallel with the ground are equipped with 4-bit adjustable capacitors that can adjust for PVT variations. To achieve optimal performance, this project utilizes a $90°$ hybrid coupler. The purpose of C_{R1} and C_{R2} is to be parallel with the first and second-stage coils of the hybrid transformer. This allows it to resonate at the central working frequency and suppress any out-of-band interference signals. The completed design layout can be seen in Fig.

3.35. The circuit measures approximately $0.32\,mm^2$.

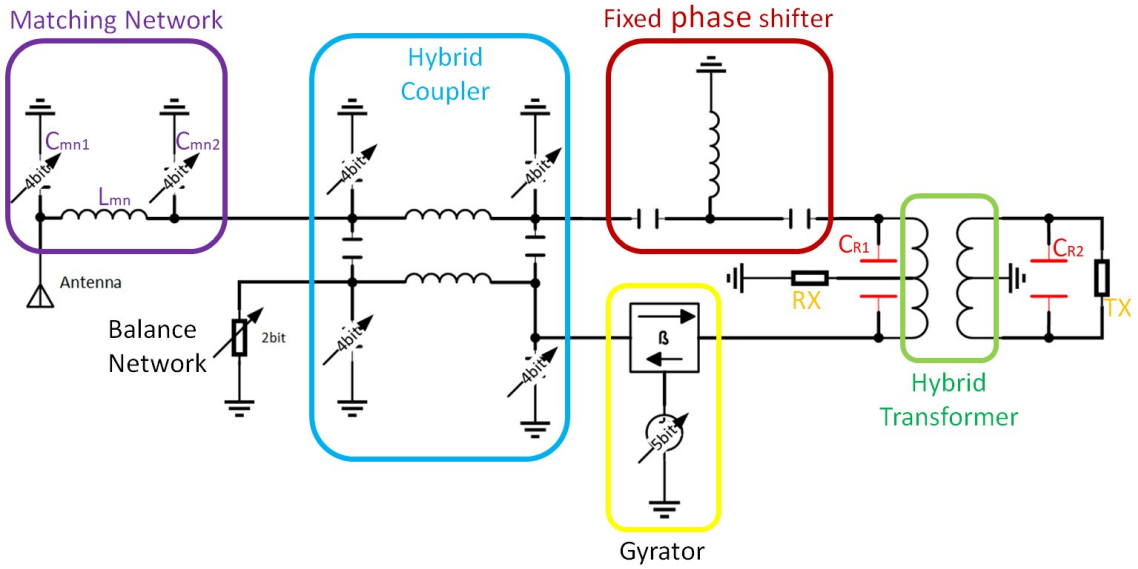

Figure 3.33: The schematic of GE-EBD.

Table 3.6: Values of capacitors and inductors in GE-EBD.

Parameters	Values	
C_{R1}	188 fF	
C_{R2}	188 fF	
C_{MN1}	45 fF ~ 160 fF	Tunable
C_{MN2}	45 fF ~ 160 fF	Tunable
L_{MN}	500 pH	

Additionally, according to Fig. 2.4 and equation (2.1), to achieve electrical balance duplexing, the four ports of the hybrid transformer need to satisfy the bi-conjugacy condition, which means the impedance seen from the RX and TX ports should be $25\,\Omega$ and $100\,\Omega$, respectively. The performance of the GE-EBD will inevitably deteriorate when there is a deviation in impedance. The changes in isolation, insertion loss, and NF are depicted in Fig. 3.34 as the impedance of RX (R_{RX}) increases from $5\,\Omega$ to $85\,\Omega$, while the impedance of TX (R_{TX}) varies from $40\,\Omega$ to $140\,\Omega$. The isolation will not change significantly in this range and can still meet the design requirements. The change in R_{RX} will not affect NF because R_{RX} as a load does not affect the calculation of the noise figure, but the change in R_{TX} will affect NF. As R_{TX} decreases, NF will increase, but the increase is insignificant, less than 0.1dB. The change in R_{RX} will affect RXIL and the optimal RXIL will be achieved around $25\,\Omega$, but it will not significantly impact TXIL. Similarly, the change in R_{TX} will affect TXIL and the optimal TXIL will be achieved between $80\,\Omega$ and $100\,\Omega$, but it will not significantly impact RXIL. The ideal TXIL is not attained with R_{tx} at approximately $100\,\Omega$ since the effective turn ratio is not precisely 1, but rather 1.05, resulting in this deviation. However, the variation is less than 0.1 dB. Overall, it is crucial to maintain the recommended impedance levels to ensure optimal GE-EBD performance.

To perform a more accurate post-simulation on the completed GE-EBD layout design, the GE-EBD layout is divided into two parts, as shown in Fig. 3.36. One part consists of larger and closer coils, for which an electromagnetic simulation is performed using Momentum to obtain S-parameters. The other part includes wiring, capacitors, active devices, and inductors from PDK. RC extraction is performed on this part of the circuit. Finally, the obtained data is loaded into the configuration for post-simulation.

The post-simulation results for the duplexer are shown in Table 3.7. The post-simulation results for the duplexer are presented in Table 3.7. As can be seen from this table, the proposed duplexer meets the performance requirements listed in Table 1.2. Compared to previous literature, the proposed duplexer achieves a wider operational bandwidth, from 6 to 8 GHz. It can attain isolation greater than

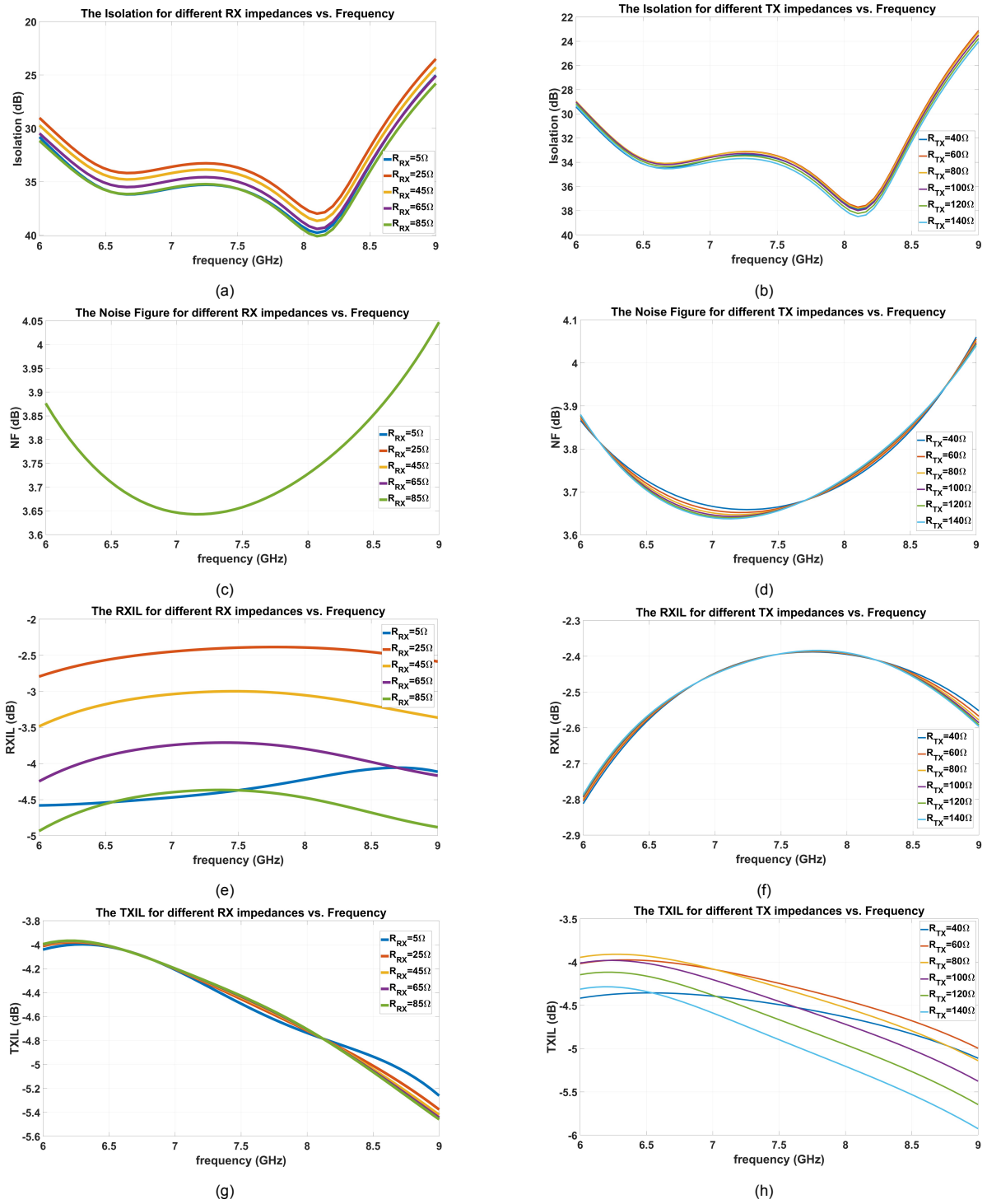

Figure 3.34: The influence of RX and TX impedance variations on the performance of GE-EBD. (a) Isolation for different RX impedances. (b) Isolation for different TX impedances. (c) Noise figure for different RX impedances. (d) Noise figure for different TX impedances. (e) RXIL for different RX impedances. (f) RXIL for different TX impedances. (g) TXIL for different RX impedances. (f) TXIL for different TX impedances.

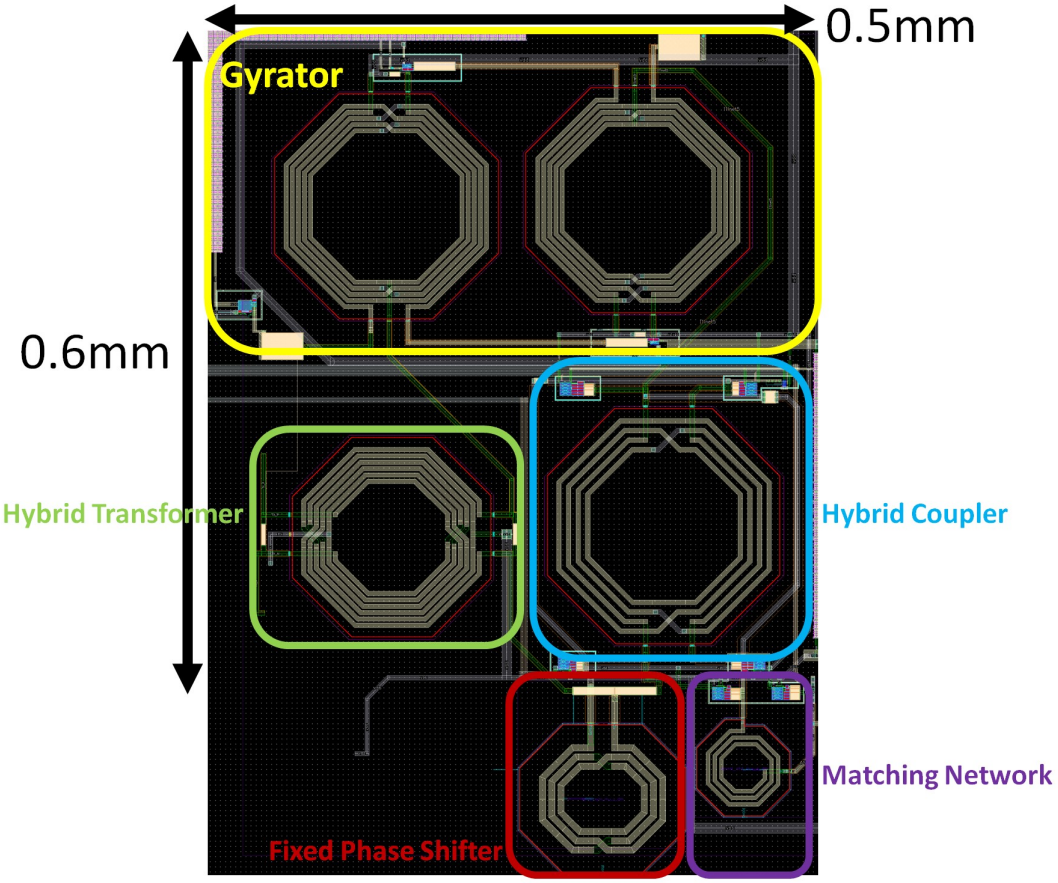

Figure 3.35: The layout of GE-EBD.

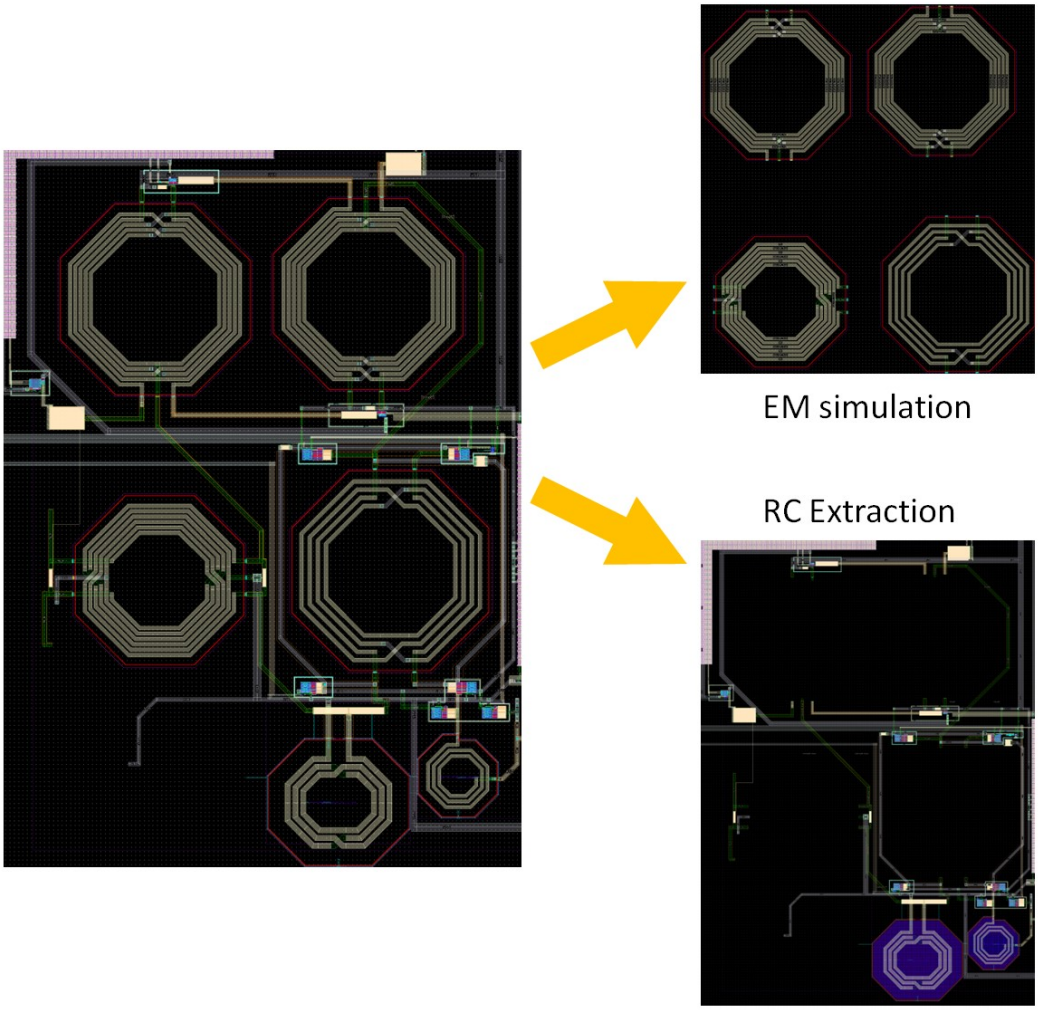

Figure 3.36: The post-simulation method of GE-EBD.

20 dB under conditions of 40% relative bandwidth and achieve more than 30 dB isolation under 30% relative bandwidth conditions. Moreover, the entire duplexer occupies only $0.32\,mm^2$ of chip area, outperforming other publications. Its power consumption, at 4.4 mW, is superior to the non-magnetic circulator using N path filter technology. Simultaneously, the proposed duplexer also achieves decent insertion losses, with an RXIL of 2.2 dB and a TXIL of 3.6 dB.

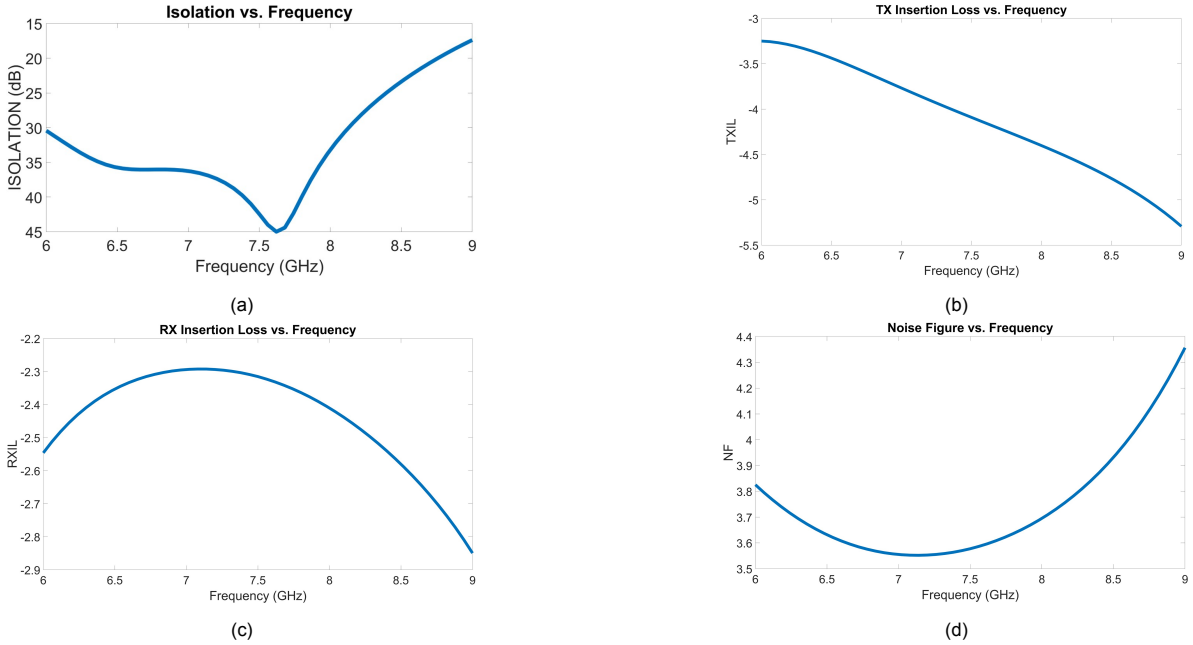

Figure 3.37: Small signal post-simulation results of GE-EBD. (a) The isolation. (b) The TX insertion loss. (c) The RX insertion loss. (d) The noise figure.

In Fig. 3.38, the simulation results for the GE-EBD's large signal are presented. It is observed that the isolation bandwidth reduces from over $2\,GHz(>30\,dB)$ to $1\,GHz(>30\,dB)$ when the input power of TX (P_{in}) is $8\,dBm$, which also happens to be the maximum output power of the UWB transceiver. When transmitting, the PA sends the signal to the antenna. The 1 dB compression point for the input signal ($P_{-1dB,in}$) is 11.8 dBm, the input-referred second-order intercept point ($IP2$) is 18.0 dBm, and the third-order intercept point ($IIP3$) is 9.0dBm. When receiving, the antenna sends the signal to the LNA. The 1dB compression point for the input signal ($P_{-1dB,in}$) is 3.6 dBm, the input-referred $IP2$ is 13.5 dBm, and $IIP3$ is 6.2 dBm.

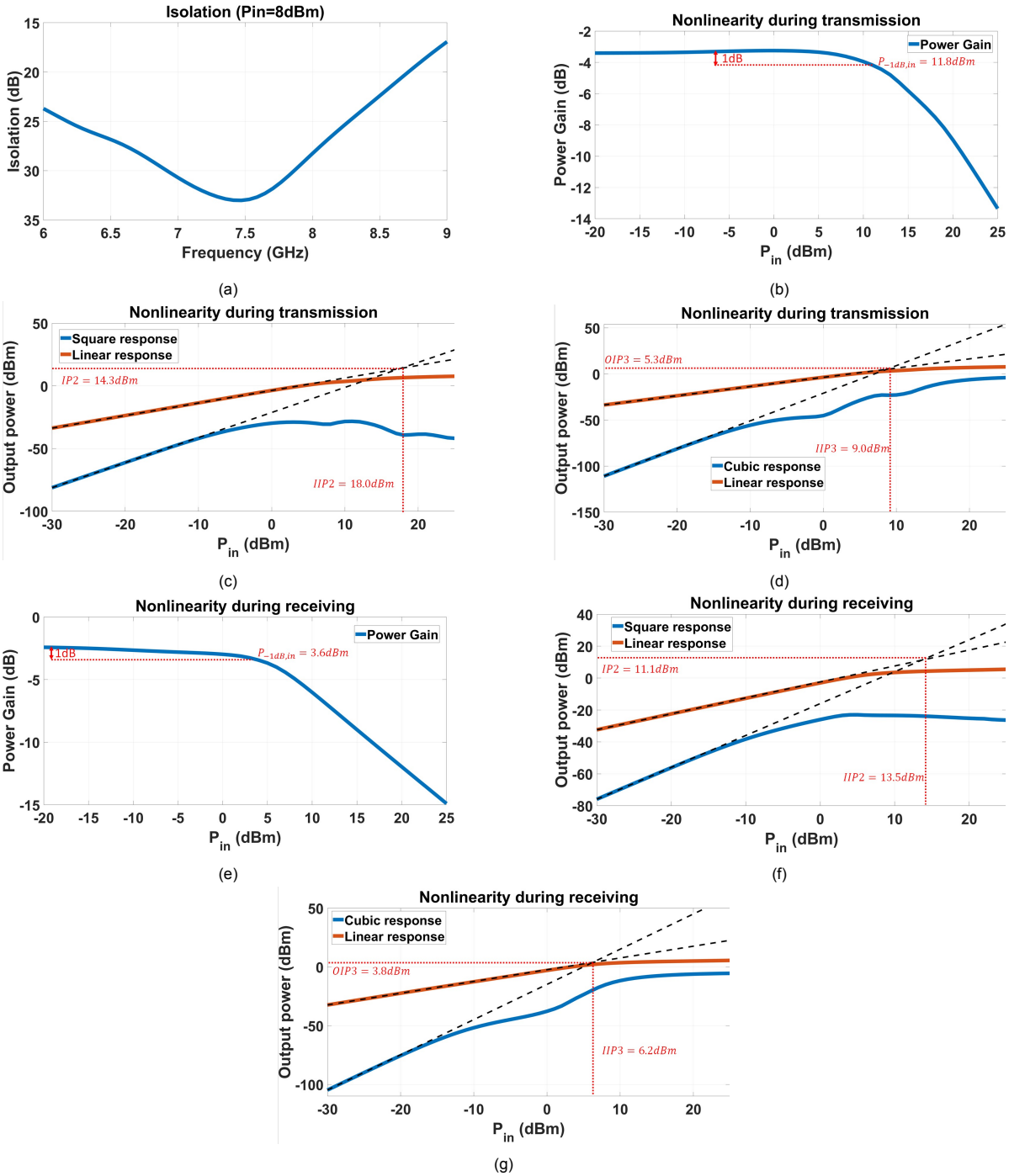

Figure 3.38: The large signal simulation of GE-EBD. (a) Isolation when $P_{in} = 8dBm$ @7.5 GHz. (b) 1 dB power gain compression point from TX to ANT. (c) The second intercept point from TX to ANT. (d) The third intercept point from TX to ANT. (e) 1 dB power gain compression point from ANT to RX. (c) The second intercept point from ANT to RX. (d) The third intercept point from ANT to RX.

Table 3.7: The Performance of the Proposed Duplexer

	ISSCCI5 [62]	ISSCCI6 [28]	ISSCCI7 [51]	ISSCCI8 [50]	RFICI8 [47]	JSSC2020 [54]	This work
Architecture	EBD	N-path filter circulator	Spatio-Temporal Modulation	N-path filter hybrid coupler	Spatio-temporal modulation	Spatio-temporal modulation	Gyrator enhanced duplexer
Technology	180nm SOI CMOS	65nm CMOS	45nm CMOS	65nm CMOS	180nm SOI CMOS	40nm CMOS	28nm CMOS
Frequency(GHz)	1.9-2.2	0.61-0.975	25	0.55-0.9	0.86-1.08	5.6-7.4	6-8
TX loss(dB)	3.7	1.7	3.3	3.1	2.1	2.2	3.6
RX loss(dB)	3.9	1.7	3.2	N/R	2.9	2.2	2.2
BW & Isolation	$15\%(>40dB)$	$1.9\%(>25dB)0.33\%(>40dB)$	$18\%(>18.5dB)$	$26\%(>30dB)4.4\%(>40dB)$	$17\%(>25dB)3.1\%(>40dB)$	$28\%(>18dB)$	$40\%(>20dB)30\%(>30dB)$
ANT-RX NF(dB)	3.9	4.3	3.3-4.4	2.7	3.1	2.4-3.4	3.4
TX-ANT IIP3(dBm)	70	27.5	20.1	25	50.0	18.7	9.0
ANT-RX IIP3(dBm)	72	8.7	19.9	N/R	36.9	N/R	6.2
Power(mW)	0	59	78.4	24	170	2.5	4.4
Chip Area(mm^2)	1.74	25(with off-chip inductors)	2.16	1mm^2 IC + 30.6mm^2 commercial coupler	16.5	0.45	0.32

4

System-level Design

After presenting the design of GE-EBD, this section briefly introduces other parts of the system such as the DSIC, receiver, transmitter, and transceiver, which have already been designed and verified. To make this project more comprehensive and practical, mature circuits from previous projects were adopted and combined with the full-duplex device designed in this thesis. The entire chip accomplishes the functionality of transmitting UWB pulse signals, amplifying received signals, and down-converting them to the baseband. Upon completing the design of the entire GE-EBD, the next task is to integrate the GE-EBD into the UWB transceiver. This requires considering the maturity and verification of the transmitter, receiver, and DSIC circuits, as well as the crucial impact of RX and TX impedance on the performance of GE-EBD. To facilitate the testing of the duplexer, a dedicated antenna switch has been designed and integrated into the transceiver. These issues will be discussed in detail in this chapter.

4.1. Impedance Matching

Based on previous calculations and simulations, the ideal impedance for optimal performance of the GE-EBD is $25\,\Omega$ as seen from RX. The block diagram for the IR-UWB receiver is illustrated in Fig. 4.1 (a). To match the impedance requirements of the GE-EBD, the impedance seen from the LNA needs to be matched. By incorporating the matching network depicted in Fig. 4.1 (b), the input impedance Z_{in} is matched to 25 ohms.

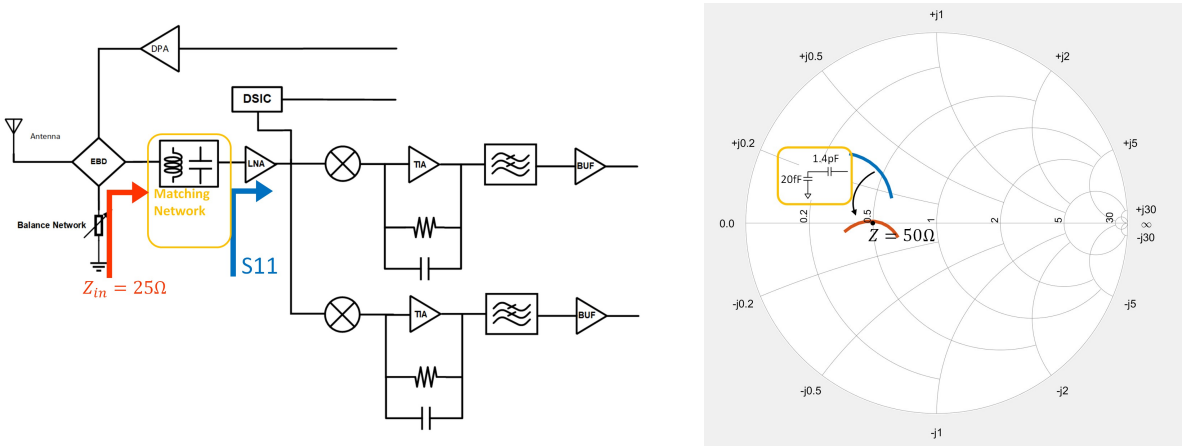

(a) (b)

Figure 4.1: The block diagram of the IR-UWB Receiver and impedance matching. (a) IR-UWB Receiver. (b) Impedance matching can be achieved using the Smith chart.

Due to the impedance at the output of the Power Amplifier (PA) being related to the load connected to the output, it is not advisable to use small-signal methods to simulate and match the impedance at the PA output. In this thesis, after connecting the transmitter (TX) with GE-EBD, as shown in Fig. 4.2.

The large-signal simulation result is shown as Fig. 4.3. The output power of the Power Amplifier (PA) is set to the maximum. In the range of 6 GHz to 9 GHz, the output power of the PA varies between 3.5 dBm and 2 dBm. The PA's output signal is differential, and when calculating power, the resistance is calculated as $100\,\Omega$, so the maximum power value calculated from this figure is only 3.5 dBm. The power at the antenna output end varies between 0.4 dBm and -0.5 dBm. Fig. 4.3 (b) is the spectrum diagram when the input signal is 7.5 GHz. it can be seen that the output signal at the antenna port is -0.1 dBm at 7.5 GHz, the highest harmonic is the second harmonic signal, at 15 GHz, the power is -20.6 dBm. The TX transmission signal is normal, and the fluctuation in the frequency range of interest is less than 1 dB.

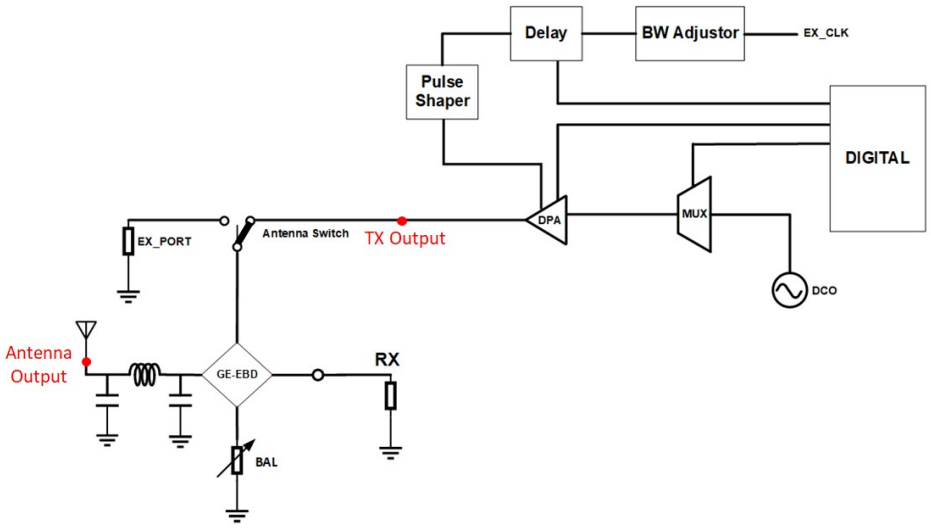

Figure 4.2: The block diagram GE-EBD and transmitter.

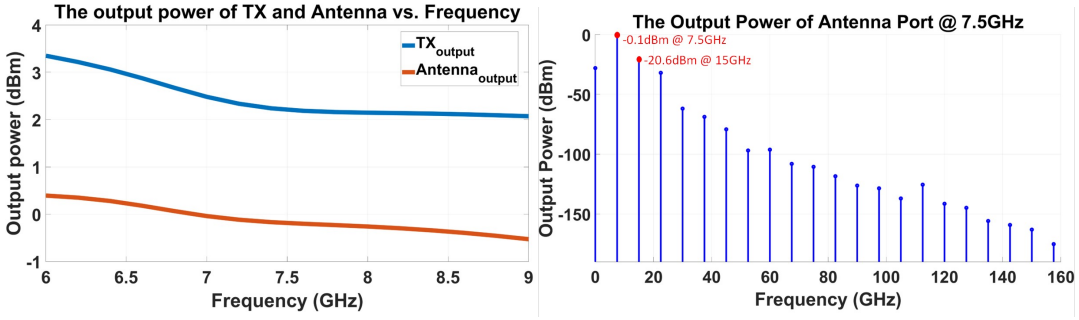

(a) (b)

Figure 4.3: The simulation result of TX part. (a) The output power of TX and Antenna from $6\,GHz$ to $9\,GHz$. (b) The spectrum when the fundamental frequency of the transmitted signal is $7.5\,GHz$.

4.2. Antenna Switch

To independently test the performance of GE-EBD, a pair of antenna switches has been added at the TX port of GE-EBD, allowing for the external input of signals via EX_PORT. When the antenna switch is connected to EX_PORT, there is more than 45 dB of isolation from the PA port of the transceiver. By adjusting the signal source connected to EX_PORT, the performance of GE-EBD under different conditions can be tested.

In [63], a detailed analysis is provided on the design of a CMOS T/R switch, specifically for applications in ultra-wideband (UWB) and over 10-GHz operations. The switch functionality for the TX and RX paths is performed by the series transistors M1 and M2. In addition, shunt transistors M3 and M4 ground out undesired signals during their respective modes.

Gate bias resistors are implemented to decrease the coupling between gate-drain and gate-source and enhance the DC-bias isolation. With the use of deep N-well technology, the device body is connected to the ground through a $5\,k\Omega$ resistor. The role of bulk resistors is somewhat complicated. [64] utilizes body-floating technology to enhance the power handling capacity of antenna switches and elaborates on its specifics.

When considering conditions of a large signal, the series transistor is in the 'on' state while the shunt transistor is 'off.' The schematic of the series resistor along with its equivalent-circuit model, can be seen in Fig. 4.4. Given the high resistance connected to the ground (R_1) relative to R_{on}, the input impedance of the transistor essentially stays equal to R_{on}. This attribute aids in enhancing performance under large signal conditions.

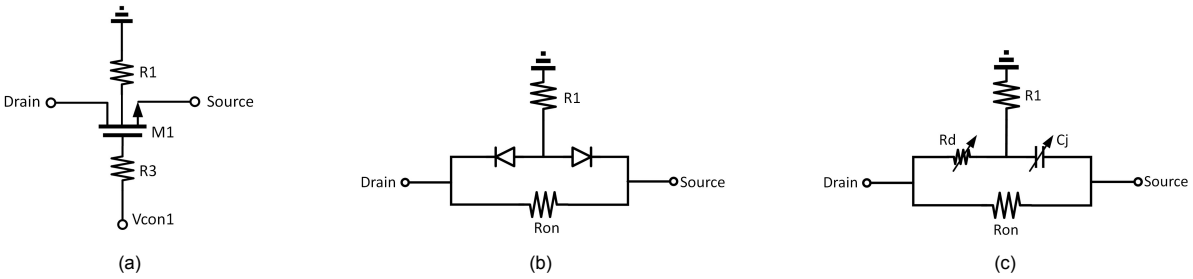

Figure 4.4: The schematic and model of the series transistor. (a) Schematic with the body-floating resistor. (b) The equivalent model. (c) The equivalent model in the "on" state.

For shunt transistors, if the body-floating technique is not employed, the high input power can activate the diode connecting the body and drain, leading to a rapid surge in current from the ground to the drain. This increased current can modify the transistor's input impedance so that the input impedance varies with the input signal, which can cause the harmonic components to rise. This will eventually reduce the power performance. Fig. 4.5 illustrates the equivalent-circuit model for an off-state transistor implementing the body-floating technique. When the input power is elevated, the diode between the drain and the body can still be activated. However, due to the considerable resistance between the body and the ground, the current increase from ground to drain is more gradual.

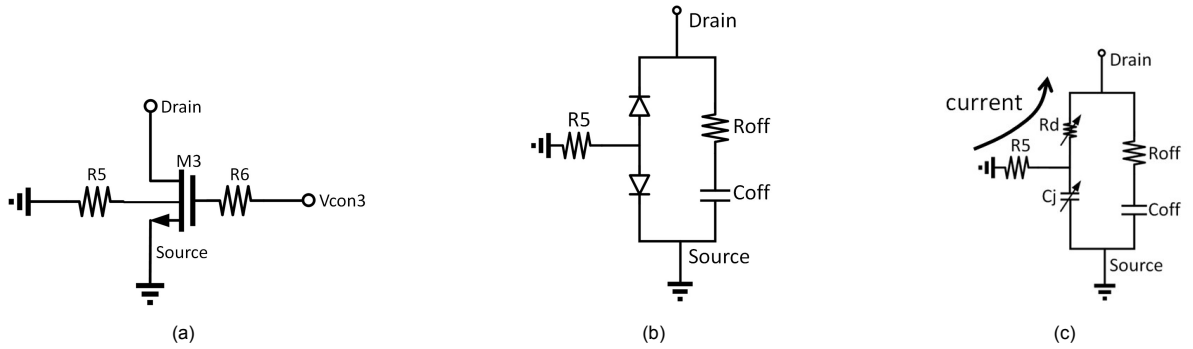

Figure 4.5: The schematic and model of the shunt transistor. (a) Schematic with the body-floating resistor. (b) The equivalent model. (c) The equivalent model in the "off" state.

The antenna switch's components are listed in Table 4.1, and the simulation results are displayed in Fig. 4.7. Within the operating frequency band, when the switch is turned on, the insertion loss from the "on" port to the common port (COM) is between 0.6 and 0.85 dB, while the isolation from the "on" port to the "off" port is greater than 40 dB. The antenna switch has a 1 dB compression point of 9.3 dBm ($P_{-1dB,in}$=9.3 dBm) and an $IIP3$ of 22 dBm, meeting system requirements.

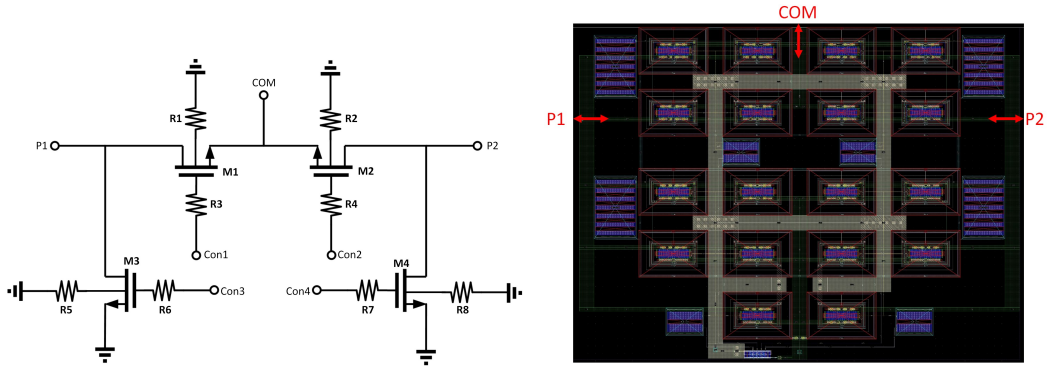

(a) (b)

Figure 4.6: The design of the antenna switch. (a) Schematic. (b) Layout.

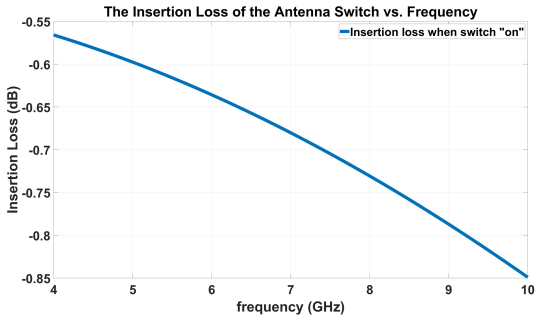

(a)

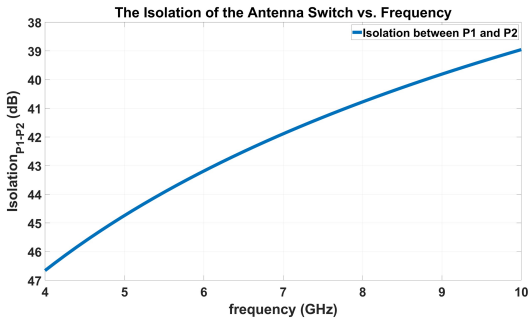

(b)

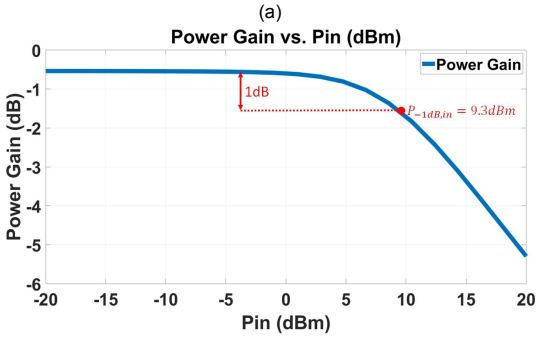

(c)

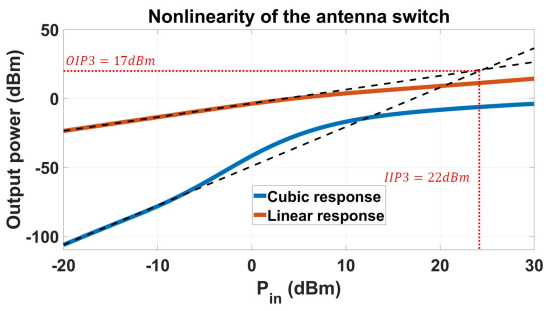

(d)

Figure 4.7: The simulation results of the antenna switch. (a) Insertion loss under small-signal conditions. (b) Isolation from ”on” port to ”off” port (c) The 1 dB power gain compression. (d) The third-order intercept point

Table 4.1: Values of components in the antenna switch.

Parameters	Values
R_1	$40\,k\Omega$
R_2	$40\,k\Omega$
R_3	$5\,k\Omega$
R_4	$5\,k\Omega$
R_5	$40\,k\Omega$
R_6	$5\,k\Omega$
R_7	$40\,k\Omega$
R_8	$5\,k\Omega$
M_1	$72\mu m/30nm$
M_2	$72\mu m/30nm$
M_3	$90\mu m/30nm$
M_4	$90\mu m/30nm$

4.3. Transceiver Design

The thesis incorporates a transmitter architecture that uses hybrid modulation from [8]. Furthermore, it also includes the implementation of the UWB receiver design from [65]. The achievement of Full-Duplex (FD) and RadCom requires the implementation of robust and efficient self-interference cancellation. This is accomplished through the use of GE-EBD at the antenna interface and the Digital Self-Interference Cancellation (DSIC) module at the analog domain. This DSIC is an improvement on the all-digital spillover cancellation method initially introduced in Sander Heijmans' master's thesis project [66], and further refined in Jiang Liu's master's thesis project [65]. In addition to this, an antenna switch has been added to the TX port of GE-EBD for standalone measurement. When the antenna switch is connected to the EX_PORT, it can directly connect to the external testing instruments. Moreover, a matching circuit has been added between GE-EBD and the LNA, which has improved the match between the duplexer and the RX and reduced the loss caused by reflection. The block diagram is shown in the following Fig. 4.8.

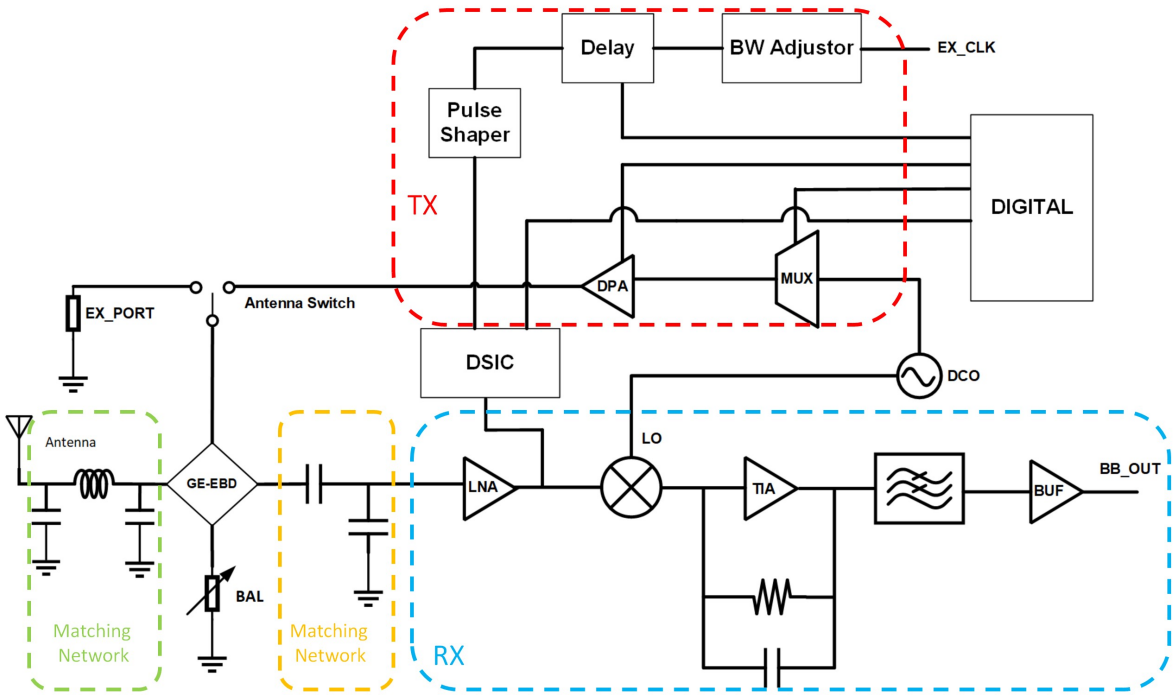

Figure 4.8: The proposed IR-UWB transceiver block diagram.

The layout of the comprehensive IR-UWB transceiver is executed and depicted in Fig. 4.9. GE-

EBD, situated adjacent to the RX and TX sections, is predominantly occupying a substantial part of the chip's right side. The DSIC circuit is located between the RX and TX sections. The digital circuit section, responsible for controlling other circuits, is positioned on the left side of the chip. The entire chip measures a compact $1.44mm \times 1.44mm$. Further steps toward system-level implementation encompass the design of the pad ring, floor planning, and dummy filling. A succinct introduction to these processes can be found in the appendix of this thesis.

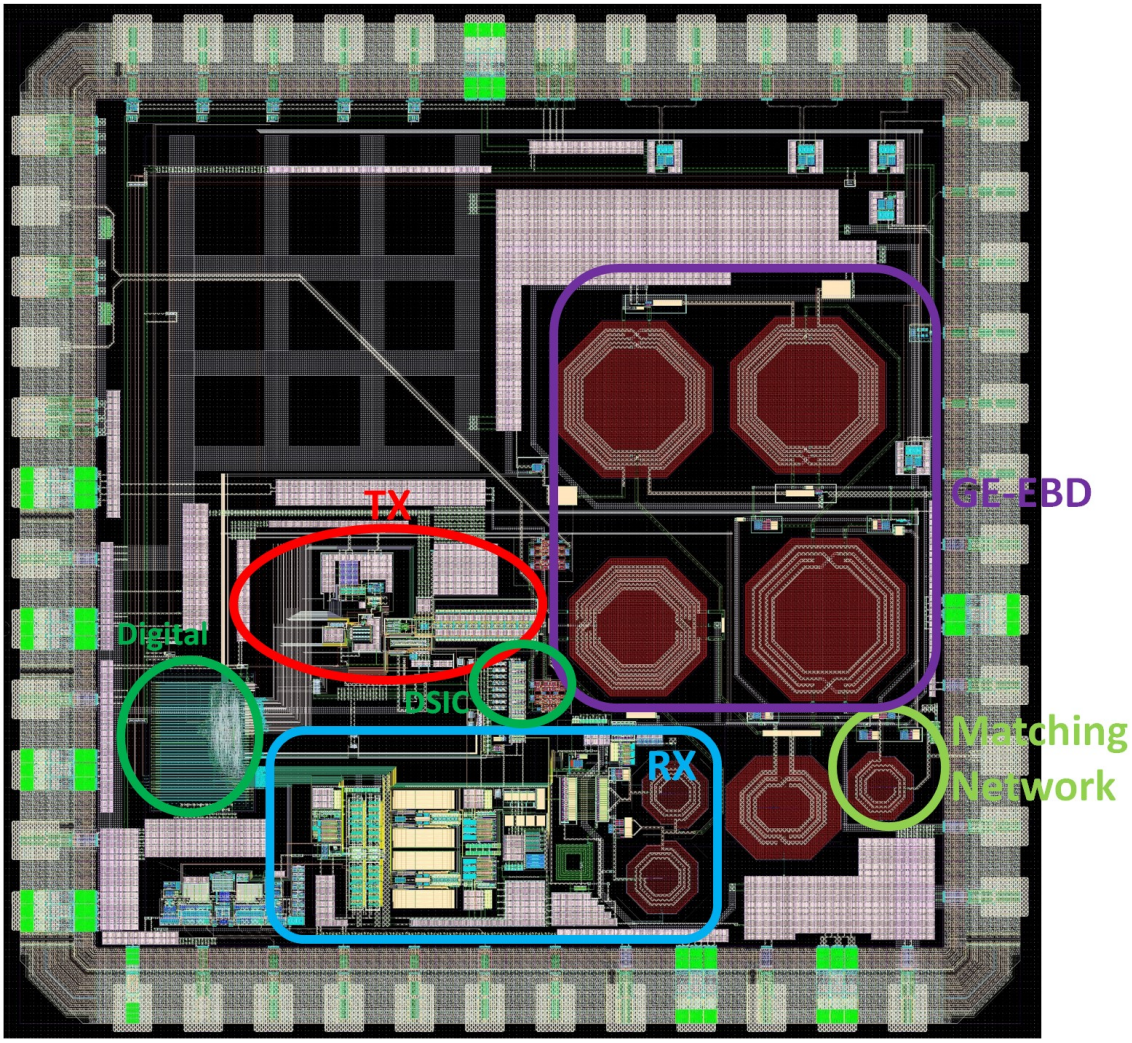

Figure 4.9: Layout implementation of the proposed IR-UWB transceiver.

5

Conclusion

5.1. Master Thesis Conclusion

This thesis presents a comprehensive exploration of the design, simulation, and potential implementation of a full duplexer and an IR-UWB transceiver, contributing to the ongoing advancements in the field of IR-UWB, particularly in RF and analog circuit design.

The proposed full duplexer, gyrator-enhanced electrical balanced duplexer (GE-EBD), as detailed in Chapter 3, is a significant focus of this thesis. The layout of the proposed duplexer, as well as the simulation model of the proposed gyrator with ideal components, are meticulously outlined. The ADS simulation results of the proposed gyrator further substantiate the theoretical feasibility of the design.

The small signal and large signal post-simulation results of GE-EBD, including the isolation, the TX insertion loss, the RX insertion loss, and the noise figure, P_{-1dB}, $IIP3$, provide valuable insights into the performance of the proposed full duplexer. These results indicate the promising potential for the real-world application of the full duplexer.

Furthermore, the post-simulation results demonstrate that this circuit design, which uses a smaller chip area of $0.32\,mm^2$ compared to other non-magnetic circulator circuit structures, achieves an RXIL of 2.2 dB, a TXIL of 3.6 dB, and over 30 dB of isolation within a frequency range of 6 to 8 GHz. This circuit has lower insertion loss than traditional EBD and, like EBD, can match antenna-end impedance mismatches.

In Chapter 4, The thesis explores the design of the system at a high level, with a focus on how the GE-EBD matches with the RX/TX, and the proposed IR-UWB transceiver. The layout implementation of the proposed IR-UWB transceiver is presented, providing a clear visual representation of the design. This chapter underscores the importance of system-level design in the successful implementation of IR-UWB systems.

In light of the detailed simulations and designs presented in this thesis, both the proposed full duplexer and the IR-UWB transceiver represent significant advancements in the field of RadCom. However, it is important to note that the transition from simulation to real-world application is a complex process that may present unforeseen challenges. Future work should therefore focus on testing these proposed designs under real-world conditions to assess their performance and identify potential areas for improvement.

5.2. Future Work

Testing of the GE-EBD and the entire IR-UWB transceiver needs to be conducted to verify the simulation results of the circuit. Due to the use of many coils in the circuit, the wiring of the circuit is long and difficult to optimize for the parasitics brought about by the length of the lines. There is still room for further optimization in this area to achieve better performance.

Additionally, in this thesis, a 90° hybrid coupler is used. As mentioned in the paper, if a $45^\circ-$ or $60^\circ-$ hybrid coupler is used, it can compensate for antenna impedance mismatch under larger antenna-end mismatch conditions. The next step would be to design and verify these two schemes.

Furthermore, this thesis uses a transformer-based gyrator rather than the popular approach of using LPTV circuits to achieve nonreciprocal phase shifting. Although the circuit used in this thesis is simpler and has certain advantages in terms of area and power consumption compared to LPTV circuits, its performance under large signal conditions is not as good as that of LPTV circuits. Future work could involve designing a gyrator circuit with superior performance and metrics to enhance the overall performance of the duplexer.

Bibliography

[1] Siwiak Kazimierz and McKeown Debra. *Ultra-wideband Radio Technology, 2nd Edition*. John Wiley Sons, 2004.

[2] Bernd Schleicher and Hermann Schumacher. “Impulse generator targeting the European UWB mask”. In: *2010 Topical Meeting on Silicon Monolithic Integrated Circuits in RF Systems (SiRF)*. 2010, pp. 21–24. DOI: 10.1109/SMIC.2010.5422846.

[3] Rakhesh Singh Kshetrimayum. “An introduction to UWB communication systems”. In: *IEEE Potentials* 28.2 (2009), pp. 9–13. DOI: 10.1109/MPOT.2009.931847.

[4] Dieter Coppens et al. “An Overview of UWB Standards and Organizations (IEEE 802.15.4, FiRa, Apple): Interoperability Aspects and Future Research Directions”. In: *IEEE Access* 10 (2022), pp. 70219–70241. DOI: 10.1109/ACCESS.2022.3187410.

[5] Faranak Nekoogar. *Ultra-Wideband Communications: Fundamentals and Applications Fundamentals and Applications*. Prentice Hall Press, 2011.

[6] Jet’aime Lowe, Hong Nie, and Zhizhang Chen. “A Code-Shifted Reference impulse radio ultra-wideband (IR-UWB) transmitter”. In: *2010 IEEE Radio and Wireless Symposium (RWS)*. 2010, pp. 535–538. DOI: 10.1109/RWS.2010.5434126.

[7] I. Oppermann et al. “UWB wireless sensor networks: UWEN - a practical example”. In: *IEEE Communications Magazine* 42.12 (2004), S27–S32. DOI: 10.1109/MCOM.2004.1367555.

[8] Minyoung Song et al. “A 1.66Gb/s and 5.8pJ/b Transcutaneous IR-UWB Telemetry System with Hybrid Impulse Modulation for Intracortical Brain-Computer Interfaces”. In: *2022 IEEE International Solid- State Circuits Conference (ISSCC)*. Vol. 65. 2022, pp. 394–396. DOI: 10.1109/ISSCC42614.2022.9731608.

[9] Wan Kim et al. “31.2 A Fully Integrated IEEE 802.15.4/4z-Compliant 6.5-to-8GHz UWB System-on-Chip RF Transceiver Supporting Precision Positioning in a CMOS 28nm Process”. In: *2023 IEEE International Solid- State Circuits Conference (ISSCC)*. 2023, pp. 462–464. DOI: 10.1109/ISSCC42615.2023.10067364.

[10] Jorge R. Fernandes and David Wentzloff. “Recent advances in IR-UWB transceivers: An overview”. In: *Proceedings of 2010 IEEE International Symposium on Circuits and Systems*. 2010, pp. 3284–3287. DOI: 10.1109/ISCAS.2010.5537916.

[11] Abdellah Chehri and Hussein T. Mouftah. “Internet of Things - integrated IR-UWB technology for healthcare applications”. In: *Concurrency and Computation: Practice and Experience* 32.2 (2020). e5454 CPE-19-0083.R2, e5454. DOI: https://doi.org/10.1002/cpe.5454. eprint: https://onlinelibrary.wiley.com/doi/pdf/10.1002/cpe.5454. URL: https://onlinelibrary.wiley.com/doi/abs/10.1002/cpe.5454.

[12] Geunhaeng Lee et al. “An IR-UWB CMOS Transceiver for High-Data-Rate, Low-Power, and Short-Range Communication”. In: *IEEE Journal of Solid-State Circuits* 54.8 (2019), pp. 2163–2174. DOI: 10.1109/JSSC.2019.2914584.

[13] Run Chen et al. “A 6.5-to-10GHz IEEE 802.15.4/4z-Compliant 1T3R UWB Transceiver”. In: *2022 IEEE International Solid- State Circuits Conference (ISSCC)*. Vol. 65. 2022, pp. 396–398. DOI: 10.1109/ISSCC42614.2022.9731638.

[14] Bowen Wang, Woogeun Rhee, and Zhihua Wang. “A Quadrature Uncertain-IF IR-UWB Transceiver with Twin-OOK Modulation”. In: *2023 IEEE International Solid- State Circuits Conference (ISSCC)*. 2023, pp. 1–3. DOI: 10.1109/ISSCC42615.2023.10067737.

[15] Elbert Bechthum et al. “A 3-10GHz 21.5mW/Channel RX and 8.9mW TX IR-UWB 802.15.4a/z 1T3R Transceiver”. In: *ESSCIRC 2022- IEEE 48th European Solid State Circuits Conference (ESSCIRC)*. 2022, pp. 421–424. DOI: 10.1109/ESSCIRC55480.2022.9911356.

[16] Kenneth E Kolodziej. *In-Band Full-Duplex Wireless Systems Handbook*. Artech House, 2021.

[17] Ashutosh Sabharwal et al. “In-band full-duplex wireless: Challenges and opportunities”. In: *IEEE Journal on selected areas in communications* 32.9 (2014), pp. 1637–1652.

[18] Steven Hong et al. “Applications of self-interference cancellation in 5G and beyond”. In: *IEEE Communications Magazine* 52.2 (2014), pp. 114–121. DOI: 10.1109/MCOM.2014.6736751.

[19] Negar Reiskarimian et al. “One-way ramp to a two-way highway: Integrated magnetic-free nonreciprocal antenna interfaces for full-duplex wireless”. In: *IEEE Microwave Magazine* 20.2 (2019), pp. 56–75.

[20] Jin Zhou et al. “Integrated full duplex radios”. In: *IEEE Communications Magazine* 55.4 (2017), pp. 142–151.

[21] Kaihui Lin et al. “A Ka-band FMCW radar front-end with adaptive leakage cancellation”. In: *IEEE Transactions on Microwave Theory and Techniques* 54.12 (2006), pp. 4041–4048.

[22] Zhongshan Zhang et al. “Full-duplex wireless communications: Challenges, solutions, and future research directions”. In: *Proceedings of the IEEE* 104.7 (2016), pp. 1369–1409.

[23] Kenneth E. Kolodziej, Bradley T. Perry, and Jeffrey S. Herd. “In-Band Full-Duplex Technology: Techniques and Systems Survey”. In: *IEEE Transactions on Microwave Theory and Techniques* 67.7 (2019), pp. 3025–3041. DOI: 10.1109/TMTT.2019.2896561.

[24] C.E. Fay and R.L. Comstock. “Operation of the Ferrite Junction Circulator”. In: *IEEE Transactions on Microwave Theory and Techniques* 13.1 (1965), pp. 15–27. DOI: 10.1109/TMTT.1965.1125923.

[25] Kamran Entesari and Mohamed Elkholy. “RF CMOS Duplexers for Frequency-Division Duplex Radios: The Most Recent Developments”. In: *IEEE Microwave Magazine* 23.7 (2022), pp. 30–46.

[26] Jin Zhou et al. “Integrated wideband self-interference cancellation in the RF domain for FDD and full-duplex wireless”. In: *IEEE Journal of solid-state circuits* 50.12 (2015), pp. 3015–3031.

[27] Tolga Dinc, Anandaroop Chakrabarti, and Harish Krishnaswamy. “A 60 GHz CMOS full-duplex transceiver and link with polarization-based antenna and RF cancellation”. In: *IEEE journal of solid-state circuits* 51.5 (2016), pp. 1125–1140.

[28] Jin Zhou, Negar Reiskarimian, and Harish Krishnaswamy. “9.8 Receiver with integrated magnetic-free N-path-filter-based non-reciprocal circulator and baseband self-interference cancellation for full-duplex wireless”. In: *2016 IEEE International Solid-State Circuits Conference (ISSCC)*. IEEE. 2016, pp. 178–180.

[29] Mohyee Mikhemar, Hooman Darabi, and Asad A Abidi. “A multiband RF antenna duplexer on CMOS: Design and performance”. In: *IEEE Journal of Solid-State Circuits* 48.9 (2013), pp. 2067–2077.

[30] Sherif H Abdelhalem, Prasad S Gudem, and Lawrence E Larson. “Hybrid transformer-based tunable differential duplexer in a 90-nm CMOS process”. In: *IEEE Transactions on Microwave Theory and Techniques* 61.3 (2013), pp. 1316–1326.

[31] S. Tanaka, N. Shimomura, and K. Ohtake. “Active circulators—The realization of circulators using transistors”. In: *Proceedings of the IEEE* 53.3 (1965), pp. 260–267. DOI: 10.1109/PROC.1965.3683.

[32] Tissana Kijsanayotin and James F. Buckwalter. “Millimeter-Wave Dual-Band, Bidirectional Amplifier and Active Circulator in a CMOS SOI Process”. In: *IEEE Transactions on Microwave Theory and Techniques* 62.12 (2014), pp. 3028–3040. DOI: 10.1109/TMTT.2014.2364827.

[33] Shihan Qin, Qiang Xu, and Yuanxun Ethan Wang. “Nonreciprocal Components With Distributedly Modulated Capacitors”. In: *IEEE Transactions on Microwave Theory and Techniques* 62.10 (2014), pp. 2260–2272. DOI: 10.1109/TMTT.2014.2347935.

[34] Jen-Feng Chang et al. “Design and Analysis of 24-GHz Active Isolator and Quasi-Circulator”. In: *IEEE Transactions on Microwave Theory and Techniques* 63.8 (2015), pp. 2638–2649. DOI: 10.1109/TMTT.2015.2442976.

[35] Chendi Yu and Howard C Luong. “An 8-mW 66-GHz Active Circulator with 40dB TX-RX Isolation in 65nm CMOS for Full-Duplex Radios”. In: *2020 IEEE Asian Solid-State Circuits Conference (A-SSCC)*. IEEE. 2020, pp. 1–4.

[36] Seyyed Amir Ayati et al. “Integrated Quasi-Circulator With RF Leakage Cancellation for Full-Duplex Wireless Transceivers”. In: *IEEE Transactions on Microwave Theory and Techniques* 66.3 (2018), pp. 1421–1430. DOI: 10.1109/TMTT.2017.2773485.

[37] Hsin-Chih Kuo et al. “A Fully Integrated 60-GHz CMOS Direct-Conversion Doppler Radar RF Sensor With Clutter Canceller for Single-Antenna Noncontact Human Vital-Signs Detection”. In: *IEEE Transactions on Microwave Theory and Techniques* 64.4 (2016), pp. 1018–1028. DOI: 10.1109/TMTT.2016.2536600.

[38] Gengzhen Qi et al. “A SAW-less tunable RF front end for FDD and IBFD combining an electrical-balance duplexer and a switched-LC N-path LNA”. In: *IEEE Journal of Solid-State Circuits* 53.5 (2018), pp. 1431–1442.

[39] Leo Laughlin et al. “Tunable frequency-division duplex RF front end using electrical balance and active cancellation”. In: *IEEE Transactions on Microwave Theory and Techniques* 66.12 (2018), pp. 5812–5824.

[40] ES Malotaux. “Full-Duplex CMOS Duplexer: Passive self-interference cancellation”. In: (2013).

[41] E. Sartori. “Hybrid Transformers”. In: *IEEE Transactions on Parts, Materials and Packaging* 4.3 (1968), pp. 59–66. DOI: 10.1109/TPMP.1968.1135893.

[42] Sherif H. Abdelhalem, Prasad S. Gudem, and Lawrence E. Larson. “Hybrid Transformer-Based Tunable Differential Duplexer in a 90-nm CMOS Process”. In: *IEEE Transactions on Microwave Theory and Techniques* 61.3 (2013), pp. 1316–1326. DOI: 10.1109/TMTT.2013.2243748.

[43] Benjamin Hershberg et al. “20.8 A dual-frequency 0.7-to-1GHz balance network for electrical balance duplexers”. In: *2016 IEEE International Solid-State Circuits Conference (ISSCC)*. IEEE. 2016, pp. 356–357.

[44] Oliver Georg Dorn. “An Electrical Balance Duplexer Architecture Without Inherent Insertion Loss Limitation”. PhD thesis. Friedrich-Alexander-Universitaet Erlangen-Nuernberg (Germany), 2022.

[45] Chang Yang and Ping Gui. “85–110-GHz CMOS magnetic-free nonreciprocal components for full-duplex transceivers”. In: *IEEE Journal of Solid-State Circuits* 54.2 (2018), pp. 368–379.

[46] Negar Reiskarimian and Harish Krishnaswamy. “Magnetic-free non-reciprocity based on staggered commutation”. In: *Nature communications* 7.1 (2016), p. 11217.

[47] Aravind Nagulu, Andrea Alù, and Harish Krishnaswamy. “Fully-Integrated Non-Magnetic 180nm SOI Circulator with > 1W P1dB, >+50dBm IIP3 and High Isolation Across 1.85 VSWR”. In: *2018 IEEE Radio Frequency Integrated Circuits Symposium (RFIC)*. 2018, pp. 104–107. DOI: 10.1109/RFIC.2018.8428969.

[48] Negar Reiskarimian et al. “18.2 highly-linear integrated magnetic-free circulator-receiver for full-duplex wireless”. In: *2017 IEEE International Solid-State Circuits Conference (ISSCC)*. IEEE. 2017, pp. 316–317.

[49] Negar Reiskarimian et al. “Analysis and Design of Commutation-Based Circulator-Receivers for Integrated Full-Duplex Wireless”. In: *IEEE Journal of Solid-State Circuits* 53.8 (2018), pp. 2190–2201. DOI: 10.1109/JSSC.2018.2828827.

[50] Sanket Jain et al. “A 0.55-to-0.9GHz 2.7dB NF full-duplex hybrid-coupler circulator with 56MHz 40dB TX SI suppression”. In: *2018 IEEE International Solid - State Circuits Conference - (ISSCC)*. 2018, pp. 400–402. DOI: 10.1109/ISSCC.2018.8310353.

[51] Tolga Dinc and Harish Krishnaswamy. “17.2 A 28GHz magnetic-free non-reciprocal passive CMOS circulator based on spatio-temporal conductance modulation”. In: *2017 IEEE International Solid-State Circuits Conference (ISSCC)*. 2017, pp. 294–295. DOI: 10.1109/ISSCC.2017.7870377.

[52] Tolga Dinc et al. “Synchronized conductivity modulation to realize broadband lossless magnetic-free non-reciprocity”. In: *Nature communications* 8.1 (2017), p. 795.

[53] Aravind Nagulu and Harish Krishnaswamy. “28.5 Non-Magnetic 60GHz SOI CMOS Circulator Based on Loss/Dispersion-Engineered Switched Bandpass Filters”. In: *2019 IEEE International Solid- State Circuits Conference - (ISSCC)*. 2019, pp. 446–448. DOI: 10.1109/ISSCC.2019.8662467.

[54] Andrea Ruffino et al. “A Wideband Low-Power Cryogenic CMOS Circulator for Quantum Applications”. In: *IEEE Journal of Solid-State Circuits* 55.5 (2020), pp. 1224–1238. DOI: 10.1109/JSSC.2020.2978020.

[55] Aravind Nagulu et al. “Nonreciprocal Components Based on Switched Transmission Lines”. In: *IEEE Transactions on Microwave Theory and Techniques* 66.11 (2018), pp. 4706–4725. DOI: 10.1109/TMTT.2018.2859244.

[56] R.C. Frye, S. Kapur, and R.C. Melville. “A 2-GHz quadrature hybrid implemented in CMOS technology”. In: *IEEE Journal of Solid-State Circuits* 38.3 (2003), pp. 550–555. DOI: 10.1109/JSSC.2002.808287.

[57] Milad Kalantari et al. “A Tunable Reflection/Transmission Coefficient Circuit Using a 45° Hybrid Coupler With Two Orthogonal Variables”. In: *IEEE Transactions on Microwave Theory and Techniques* 67.4 (2019), pp. 1402–1411. DOI: 10.1109/TMTT.2019.2895578.

[58] Behzad Razavi and Razavi Behzad. *RF microelectronics*. Vol. 2. Prentice hall New York, 2012.

[59] J.R. Long. “Monolithic transformers for silicon RF IC design”. In: *IEEE Journal of Solid-State Circuits* 35.9 (2000), pp. 1368–1382. DOI: 10.1109/4.868049.

[60] Mohamed Elkholy et al. “Low-Loss Integrated Passive CMOS Electrical Balance Duplexers With Single-Ended LNA”. In: *IEEE Transactions on Microwave Theory and Techniques* 64.5 (2016), pp. 1544–1559. DOI: 10.1109/TMTT.2016.2541118.

[61] H. Greenhouse. “Design of Planar Rectangular Microelectronic Inductors”. In: *IEEE Transactions on Parts, Hybrids, and Packaging* 10.2 (1974), pp. 101–109. DOI: 10.1109/TPHP.1974.1134841.

[62] Barend van Liempd et al. “2.2 A +70dBm IIP3 single-ended electrical-balance duplexer in 0.18um SOI CMOS”. In: *2015 IEEE International Solid-State Circuits Conference - (ISSCC) Digest of Technical Papers*. 2015, pp. 1–3. DOI: 10.1109/ISSCC.2015.7062851.

[63] Qiang Li and Y. P. Zhang. “CMOS T/R Switch Design: Towards Ultra-Wideband and Higher Frequency”. In: *IEEE Journal of Solid-State Circuits* 42.3 (2007), pp. 563–570. DOI: 10.1109/JSSC.2006.891442.

[64] Mei-Chao Yeh et al. “Design and analysis for a miniature CMOS SPDT switch using body-floating technique to improve power performance”. In: *IEEE Transactions on Microwave Theory and Techniques* 54.1 (2006), pp. 31–39. DOI: 10.1109/TMTT.2005.860894.

[65] Jiang Liu. “An Energy-Efficient High-Speed Full-Duplex IR-UWB Transceiver For Joint Radar and Communication (RadCom)”. MA thesis. Technische Universiteit Delft, 2022.

[66] Sander Heijmans. “An All-Digital Spillover Cancellation Method for IR-UWB Communication Radar”. MA thesis. Technische Universiteit Eindhoven, 2022.

Appendices

A. Floor Plan

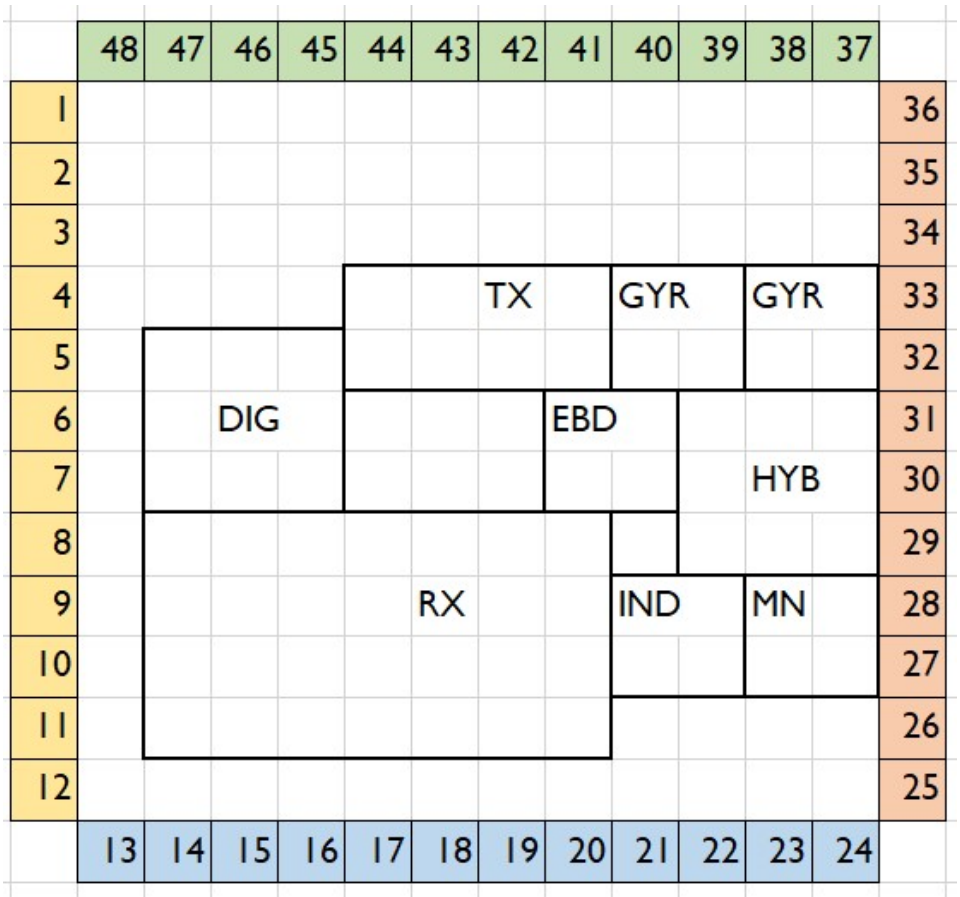

Figure 1: Floor plan.

	Number	Pin Name	Type	Direction	Description
	1	VSS_PA	VDC	Input	VSS for antenna switch
	2	EXT_TX_P	VAC	Input	external RF signal
	3	VSS_PA	VDC	Input	VSS for antenna switch
	4	EXT_TX_N	VAC	Input	external RF signal
PRCUT	5	VSS_PA	VDC	Input	VSS for PA
	6	VDD_PA	VDC	Input	VDD for PA
PRCUT	7	VSS	VDC	Input	Common VSS
	8	VDD_HS	VDC	Input	VDD for High-Speed Baseband
PRCUT	9	VSS	VDC	Input	Common VSS
	10	VDD_DCO	VDC	Input	VDD for DCO
PRCUT	11	VSS	VDC	Input	Common VSS
	12	VDD_DIG	VDC	Input	VDD for digital
PRCUT	13	VDD1P8	VDC	Input	1.8V VDD for output buffer
	14	VSS1P8	VDC	Input	VSS for output buffer
	15	RX_OUT_QP	VAC	Output	RX baseband output
	16	RX_OUT_QN	VAC	Output	RX baseband output
	17	RX_OUT_IN	VAC	Output	RX baseband output
	18	RX_OUT_IP	VAC	Output	RX baseband output
	19	I_VCMOUT	VDC	Input	VCMOUT
PRCUT	20	VSS	VDC	Input	Common VSS
	21	VDD_BB	VDC	Input	VDD for analog baseband
PRCUT	22	VSS	VDC	Input	Common VSS
	23	VDD_RX_RF	VDC	Input	VDD for RX_RF
	24	VSS	VDC	Input	Common VSS
	25	VSS	VDC	Input	Common VSS
PRCUT	26	VSS	VDC	Input	Common VSS
	27	RF_IN_OUT	VAC	Output	RF output
	28	VSS	VDC	Input	Common VSS
	29	VDD_DUP	VDC	Input	VDD for duplexer
	30	VSS	VDC	Input	Common VSS
PRCUT	31	LVDS_CK_P	VAC	Input	LVDS clock (500 MHz)
	32	LVDS_CK_N	VAC	Input	LVDS clock (500 MHz)
	33	EXT_CK	VAC	Input	External clock (500 MHz)
	34	LVDS_IN_P<3>	VAC	Input	LVDS data input (250 Mbps)
	35	LVDS_IN_N<3>	VAC	Input	LVDS data input (250 Mbps)
	36	LVDS_IN_P<2>	VAC	Input	LVDS data input (250 Mbps)
	37	LVDS_IN_N<2>	VAC	Input	LVDS data input (250 Mbps)
	38	LVDS_IN_P<1>	VAC	Input	LVDS data input (250 Mbps)
	39	LVDS_IN_N<1>	VAC	Input	LVDS data input (250 Mbps)
	40	LVDS_IN_P<0>	VAC	Input	LVDS data input (250 Mbps)
	41	LVDS_IN_N<0>	VAC	Input	LVDS data input (250 Mbps)
	42	VSS_IO	VDC	Input	VSS for IO
	43	VDD_IO	VDC	Input	VDD for IO
	44	RSTN	VDC	Input	SPI
	45	CSN	VAC	Input	SPI
	46	MOSI	VAC	Input	SPI
	47	MISO	VAC	Input	SPI
	48	SCK	VDC	Input	SPI

Figure 2: Pin List.

B. Layout and Dummy Filling

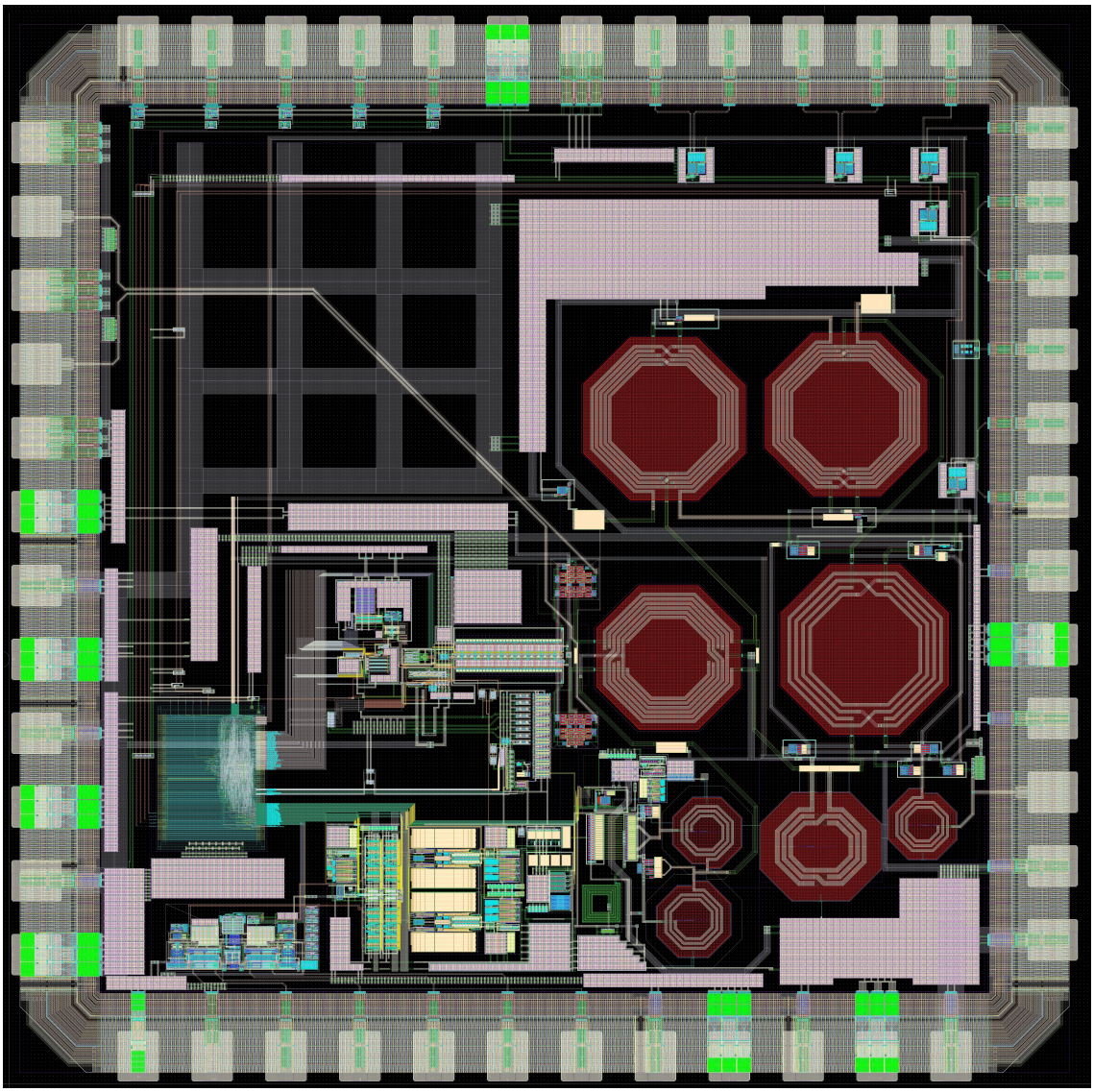

Figure 3: Chip Layout without dummy filling.

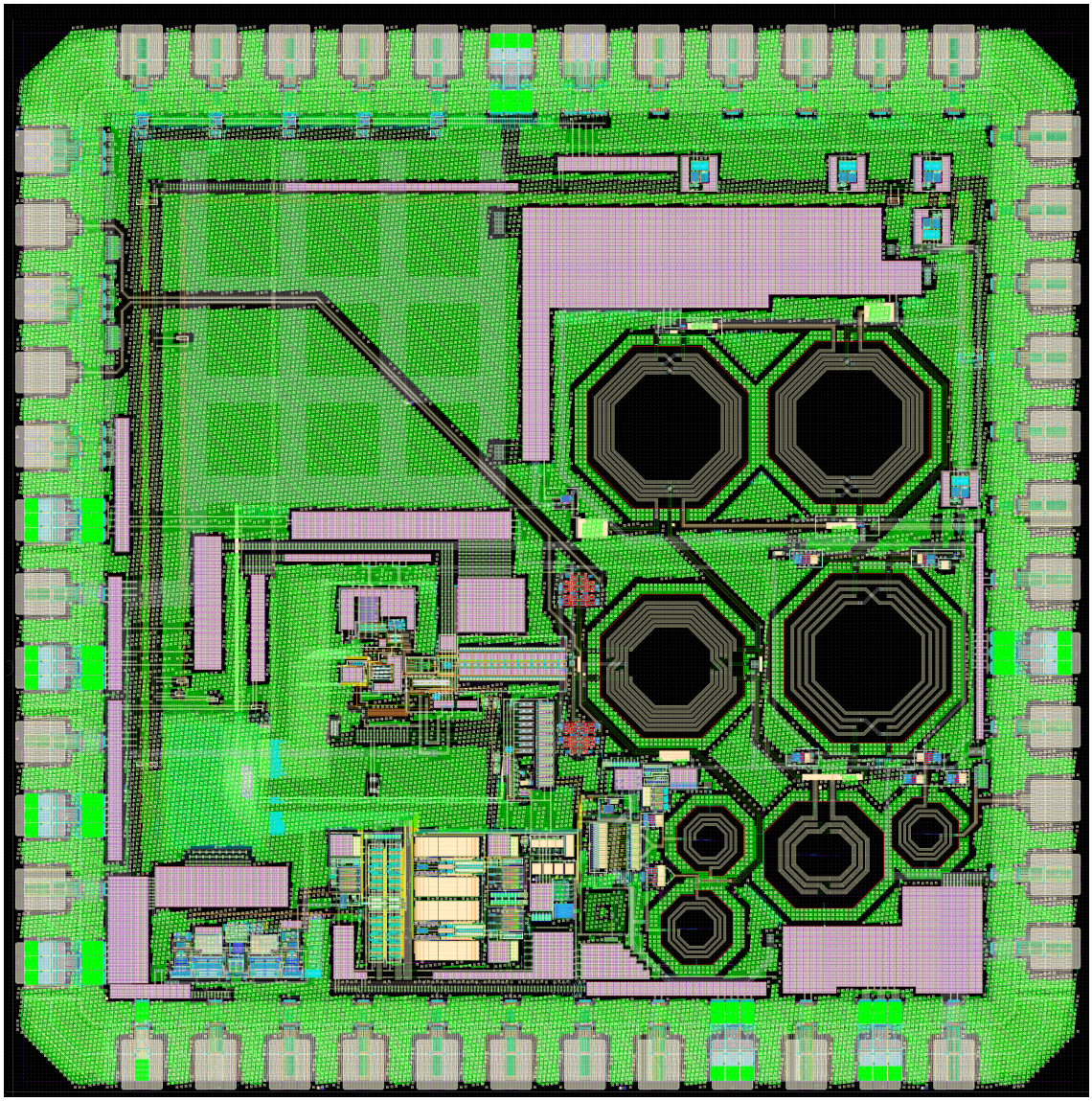

Figure 4: Chip Layout with dummy filling.